THE UNIVERSITY of ADELAIDE

QED+QCD Corrections to the Anomalous Magnetic Moment of the Muon

Alex Westin

Supervisors:
Waseem Kamleh
James Zanotti

A thesis submitted towards the degree of Doctor of Philosophy

The Faculty of Sciences
The University of Adelaide

June 30, 2021

Abstract

The current 3.7σ discrepancy between experimental and Standard Model determinations of the anomalous magnetic moment has long stood without resolution. This serves as an important test for the Standard Model of particle physics, which is the best theory we have to describe the universe at a subatomic scale. If this discrepancy can be removed though an increase of the precision of the experimental results and Standard Model calculations, we will have another important constraint on the Standard Model. On the other hand, if this discrepancy is increased we will have important evidence of new physics effects, beyond our current understanding. Either resolution will be of great impact for the physics community.

The large majority of the Standard Model uncertainty comes from hadronic contributions. In this thesis we investigate improvements to the leading order hadronic contribution using a technique called lattice gauge theory. In particular, we will look at the inclusion of QED corrections to the leading order hadronic contribution using fully dynamical QCD+QED gauge field ensembles generated by the QCDSF collaboration. This investigation is undertaken using two lattice volumes, with three sets of sub-ensembles on each volume. In order to extrapolate the results to the physical quark mass we also use a range of partially quenched quark masses, corresponding to pion masses ranging from 230 MeV to 790 MeV. From this study we find the QED corrections to be $0.2\% \pm 0.1\%$. While small, this is in no way insignificant. Current lattice studies aim for a precision greater than 0.5%, making the QED corrections of great importance in meeting that goal.

We also present an exploratory investigation into the QED corrections to the leading order disconnected contribution. This is done at the SU(3) symmetric point using a single lattice volume. We find a QED correction of $\mathcal{O}\left(0.5\%\right)$.

Declaration

I certify that this work contains no material which has been accepted for the award of any other degree or diploma in my name, in any university or other tertiary institution and, to the best of my knowledge and belief, contains no material previously published or written by another person, except where due reference has been made in the text. In addition, I certify that no part of this work will, in the future, be used in a submission in my name, for any other degree or diploma in any university or other tertiary institution without the prior approval of the University of Adelaide and where applicable, any partner institution responsible for the joint-award of this degree.

I give permission for the digital version of my thesis to be made available on the web, via the University's digital research repository, the Library Search and also through web search engines, unless permission has been granted by the University to restrict access for a period of time.

I acknowledge the support I have received for my research through the provision of an Australian Government Research Training Program Scholarship.

Alex Westin

Acknowledgements

Firstly, I must thank my supervisors, Waseem and James. Without your help over these past 4 years (plus honours!) I would have no thesis. For the drafting, coding, analysis and explaining you have done for me, I thank you.

Next to my fellow students, old and new. Thank you to the lattice group for helping me to get started, and taking the time to explain my project to me. To Alex Chambers, Finn Stokes, Jacob Bickerton, Josh Charvetto, Kim Somfleth and especially Ryan Bignell, thank you for welcoming me to the group and to the office. Your experience has been appreciated. Also a thank you to the whole physics department. It has been a wonderful atmosphere to spend the last 4 years in, I couldn't have asked for a better environment.

I must also thank my close circle of friends outside of uni, you guys have been wonderful to unwind with. Special mention to 2019 Australian Survivor runner up, Baden Gilbert.

Thank you to my family for providing me with an environment where I was able to pursue my ambitions, and put off the responsibility of 'getting a hair cut and a real job'.

Finally, I must give a massive thank you to my amazing partner, Anastasia. Thank you for your patience and support over these last few years, and thank you for making my life so amazing.

Contents

Chapter 1.

Introduction

In the pursuit of a deep understanding of the underlying laws which govern our universe, no theory has had such impact or success as the Standard Model (SM) of particle physics. This theory describes the universe at the subatomic scale, and unifies the electromagnetic, weak and strong interactions between the the fundamental particles. The SM represents our most complete understanding of the universe at this scale.

With the success of the SM, comes countless tests and verification's. Much of modern particle physics involves verifying predictions made by the SM, improving the precision of SM quantities, and searching for new physics which is not described by the SM, known as beyond Standard Model (BSM) physics.

One such test of the SM comes from the anomalous magnetic moment of the muon. First presented in 1948, the anomalous magnetic moment of the electron was predicted by Schwinger [1], and measured by Kush and Foley in [2], and served as one of the major pieces of supporting evidence for Quantum Electrodynamics (QED), which is one of the major pieces of the SM. Fast forward to today, and the anomalous magnetic moment of the electron has now been experimentally measured, and calculated using the SM to a precision greater than 1 part per billion [3, 4]. These two determinations agree to more than 10 significant figures.

The anomalous magnetic moment of the muon, however, has much less agreement between experimental measurements, and the SM calculation, making this an area of great interest in testing the SM and searching for BSM physics. Currently there exists a 3.7σ discrepancy between the SM prediction and experimental measurement [5]. This is below the standard 5σ threshold required to verify the presence of new physics, but it is a large enough discrepancy to garner great interest.

In order to resolve this discrepancy, either into a 5σ signal or by removing the discrepancy, there is desire to increase the precision of the experimental and SM values for the anomalous magnetic moment of the muon. From the experimental side, Fermilab is well underway with their E989 experiment, with first results expected very soon [6, 7]. This experiment aims to increase the precision of the experimental value by a factor of four. J-PARC also has a new experiment in development, E34, also aims to increase the experimental precision [8].

In order to fully take advantage of these new experimental results, we hope to also have an increase in the precision of the SM calculation. In this work we look at one possible source of improving the precision of the SM calculation by including full QED corrections to the leading order hadronic contribution using a technique called lattice gauge theory. To date, only Ref. [9] provides a full estimate of all QED corrections, including those beyond the electro-quenched approximation. As we are pushing for such high presision, an independent calculation using different methods can help provide confidence in these results, and help to reduce the overall uncertainty.

Outline

In Chapter 2, we will discuss the SM in some more detail, focusing on QED and particularly Quantum Chromodynamics (QCD). Here we discuss how the subatomic particles interact under these theories, and look at the QED and QCD Lagrangians, as well as some of the key features of QCD.

In Chapter 3 we go into the background of the anomalous magnetic moment of the muon, and discuss the experimental methods used, as well as how the SM is used to calculate it. This serves to motivate the lattice method used in our analysis, as well as justifying the focus on the hadronic vacuum polarisation term.

Chapters 4 and 5 look at the lattice methods used in this work. This explains how we can discretise space-time and our action in order to compute them non-perturbatively on a computer.

In Chapter 6 we discuss the vector current renormalisation, which is required as we simplify the computational cost by using the local current at the source.

Chapter 7 looks at calculating the hadronic vacuum polarisation term on the lattice, using two different techniques. First we look at the vacuum polarisation tensor

method, and then the time-momentum representation. Here we also investigate any finite-volume effects which are present in our results and attempt to correct for them.

Chapter 8 presents the size of the QED corrections which we find in the hadronic contribution.

The final chapter, Chapter 9, presents our first look at the disconnected contributions including QED corrections. The results presented here serve as a potential pathway towards future work which should be pursued in future studies.

We finish with a summary of the work, and concluding remarks in Chapter 10.

Chapter 2.

Quantum Electrodynamics and Chromodynamics

The Standard Model (SM) of particle physics is the best theory we have to describe the universe at a subatomic scale. The theory provides a description for three of the four fundamental forces of nature; electromagnetism, and the strong and weak nuclear forces. The theory correctly predicted the existence of the $W^{\pm}$ and Z^0 gauge bosons long before experimental evidence, and with the discovery of the Higgs boson [10, 11], all elementary particles predicted by the SM have been observed.

The SM provides 12 elementary spin-half particles called fermions, which consist of 6 flavours of quark, and 6 flavours of lepton split into 3 generations of charged-lepton and neutrino pairs. Force is then mediated by the exchange of 1 of 4 spin-one gauge bosons. These bosons are the photon, which is the mediator of the electromagnetic force, the charged and neutral weak bosons, $W^{\pm}$ and Z^0, which mediate the weak nuclear force, and the gluon which mediates the strong nuclear force. The SM particles and interactions are summarised in Figure 2.1.

In this thesis we will focus on the quark interactions. As quarks have both colour charge and electric charge, they interact with both gluons and photons, described by Quantum Chromodynamics (QCD) and Quantum Electrodynamics (QED) respectively[1]. QCD describes how particles with colour charge interact though the exchange of gluons. In the SM, the colour charge carrying particles are the quarks, and the gluons themselves. QED describes how particles with electric charge interact though the ex-

[1] Quarks also interact with the $W^{\pm}$ and Z^0 bosons via the weak interaction, but this interaction will be neglected as its contributions to observables of interest here is much smaller than the uncertainty on any of our calculations

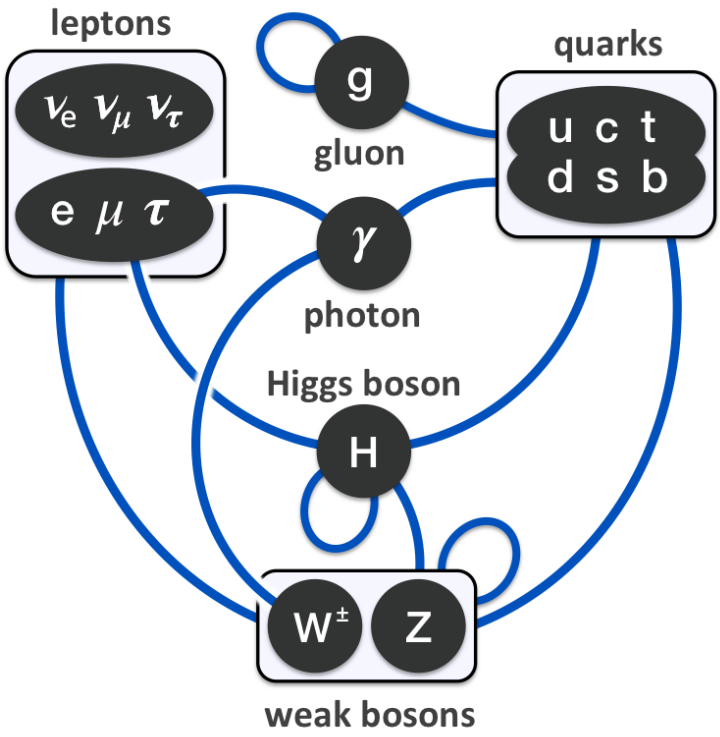

Figure 2.1. Elementary particles of the SM, and their interactions. Image obtained from [12].

change of photons. In the SM, the electric charge carrying particles are the quarks, the charged leptons, and the $W^{\pm}$ boson. As we are focusing on the quark interactions, we will ignore the charged leptons.

2.1. Quantum Electrodynamics

Quantum Electrodynamics (QED) is a Yang-Mills type gauge theory, with U(1) gauge symmetry. It describes how electrically charged particles, such as quarks and the charged-fermions, interact via the exchange of photons. This leads to a single interaction vertex, shown in Figure 2.2.

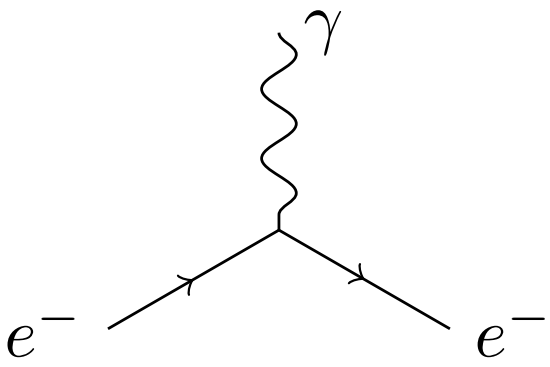

Figure 2.2. The QED interaction vertex, with a photon and fermion. Wavy line represents a photon and solid lines represent fermions. If we consider time flowing from left to right this diagram represents an electron scattering off a photon.

2.1.1. Mathematical formulation

Starting with Maxwell's equations for electromagnetism, we can write them in a Lorentz covariant form as form as

$$\partial_\mu F^{\mu\nu} = J^\nu_{em} \tag{2.1}$$

for the field strength tensor

$$F^{\mu\nu} = \partial^\mu A^\nu - \partial^\nu A^\mu, \tag{2.2}$$

with the electromagnetic potential $A^\mu = \left(V, \vec{A}\right)$, and current vector $J^\nu_{em} = \left(\rho_{em}, \vec{j}_{em}\right)$. Gauss' law and the modified Ampere law come directly from expanding Eq. 2.1. The last two Maxwell equations (which can be written as $\frac{1}{2}\partial^\alpha \epsilon_{\alpha\beta\mu\nu} F^{\mu\nu} = 0$) are automatically satisfied by writing $F^{\mu\nu}$ in a Lorentz covariant and gauge invariant form in terms of A^μ. This also implies that $\partial_\mu \partial_\nu F^{\mu\nu} = 0$ as $F^{\mu\nu}$ is anti-symmetric, which leads to charge conservation $\partial \cdot J = 0$. This can be satisfied by the Lagrangian for a free complex scalar field

$$\mathcal{L}_{photon} = -\frac{1}{4} F_{\mu\nu} F^{\mu\nu}, \tag{2.3}$$

which describes the dynamics of the photon field.

Index	Description	Representation
Dirac	Dirac index	α, β
Lorentz	Lorentz index	μ, ν
Spatial	Spatial index	i, j, k
Colour	Colour index	a, b, c
Colour (adjoint)	Colour index (adjoint)	u, v, w
Quark Flavour	Quark flavour	f, g

Table 2.1. Summary of indexing conventions used in this thesis

We can construct the fermion interacting term by starting with the free fermion Lagrangian

$$\mathcal{L}_{fermion} = \bar{\phi}_f^\alpha(x) \left(i\not{\partial}_{\alpha\beta} - m_f\delta_{\alpha\beta}\right) \phi_f^\beta(x) \tag{2.4}$$

where $\not{\partial}_{\alpha\beta} = \gamma^\mu_{\alpha\beta}\partial_\mu$ using the Feynman slash notation. The fermion field transforms under a local U(1) gauge transformation $\Omega = e^{iq\alpha}$ as

$$\phi_f^\alpha(x) \xrightarrow{\Omega} \phi_f'^\alpha(x) = \Omega\phi_f^\alpha(x), \tag{2.5}$$

$$\bar{\phi}_f^\alpha(x) \xrightarrow{\Omega} \bar{\phi}_f'^\alpha(x) = \bar{\phi}_f^\alpha(x)\Omega^\dagger. \tag{2.6}$$

We also require that our Lagrangian is invariant under local gauge transformations. If we use the form presented in Eq. 2.4 we find that

$$\mathcal{L}_{fermion} \xrightarrow{\Omega} \mathcal{L}' = \bar{\phi}_f^\alpha(x)\Omega^\dagger \left(i\not{\partial}_{\alpha\beta} - m_f\delta_{\alpha\beta}\right) \Omega\phi_f^\beta(x) \tag{2.7}$$

$$= \bar{\phi}_f^\alpha(x)\Omega^\dagger\not{\partial}_{\alpha\beta}\Omega\phi_f^\beta(x) - \bar{\phi}_f^\alpha(x)(m_f\delta_{\alpha\beta})\phi_f^\beta(x) \tag{2.8}$$

$$\neq \mathcal{L}_{fermion}, \tag{2.9}$$

such that this Lagrangian is not invariant under local gauge transformations. This is due to the derivative, $\not{\partial}_{\alpha\beta}$. We can resolve this by defining a replacement derivative, $\not{D}(x)_{\alpha\beta} = \not{\partial}_{\alpha\beta} - ig\not{A}(x)_{\alpha\beta}$, which we call the gauge covariant derivative, such that

$$\not{D}(x)_{\alpha\beta}\phi_f^\beta(x) \xrightarrow{\Omega} \left(\not{D}(x)_{\alpha\beta}\phi_f^\beta(x)\right)' = \Omega\left(\not{D}^{\alpha\beta}(x)\phi_f^\beta(x)\right). \tag{2.10}$$

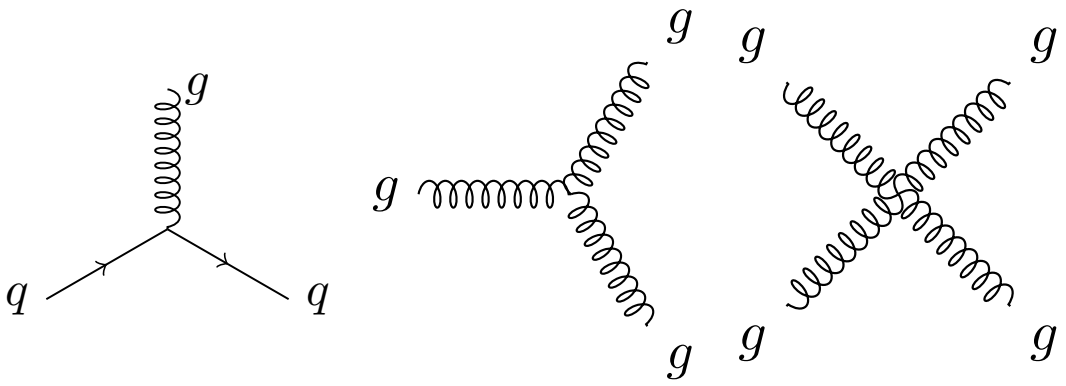

Figure 2.3. The 3 QCD interaction vertices, showing (left to right) the quark-gluon vertex, the three gluon vertex, and the four gluon vertex.

Using the covariant derivative, the Lagrangian for the fermion interaction term is now gauge invariant, and our full QED Lagrangian can be written as

$$\mathcal{L}_{QED} = \mathcal{L}_{fermion} + \mathcal{L}_{photon} \tag{2.11}$$

$$= \bar{\phi}_f^{\alpha}(x)\left(i\not{D}_{\alpha\beta} - m_f\delta_{\alpha\beta}\right)\phi_f^{\beta}(x) - \frac{1}{4}F_{\mu\nu}F^{\mu\nu}. \tag{2.12}$$

2.2. Quantum Chromodynamics

Quantum Chromodynamics (QCD) is the theory of the strong nuclear force, and describes how colour-charge carrying particles interact via the exchange of gluons. The only SM elementary particles with colour charge are the six quark flavours, and gluons themselves. Unlike QED, where the photons do not carry electric charge, in QCD the gluons can undergo self-interactions as they do carry colour charge. This leads to more complex dynamics, which we will see throughout this section. Firstly, this means that QCD has three interaction vertices, compared to the one of QED, shown in Figure 2.3. This also means there will be some additional terms in the field strength tensor and QCD Lagrangian, as shown in the next section.

2.2.1. Mathematical formulation

The Lagrangian for QCD is obtained by following a similar method, redefining the field strength tensor $F_{\mu\nu} \rightarrow G^u_{\mu\nu}$ and potential $A_\mu \rightarrow A^u_\mu$ to represent the gluon field, and

the fermion field $\phi_f(x)_\alpha$ to the quark field $\psi_f(x)^a_\alpha$, where the index f is now restricted to quark flavour. Here we have introduced colour indices in both the fundamental and adjoint representations of SU(3), where the index a has dimension 3 in the fundamental representation, and index u has dimension $3^2-1=8$ in the adjoint representation. The field strength tensor is redefined as

$$\begin{aligned}[G_{\mu\nu}(x)]^u =& [\partial_\mu A_\nu(x)]^u - [\partial_\nu A_\mu(x)]^u + g f^{uvw} A^v_\mu(x) A^w_\nu(x) \\ =& [G^0_{\mu\nu}(x)]^u + g f^{uvw} A^v_\mu(x) A^w_\nu(x),\end{aligned} \tag{2.13}$$

where f^{uvw} are the structure constants of SU(3). Note that this looks like the QED field strength tensor in Eq. 2.2, except with an additional term which contains the gluon self-interactions. To ensure our Lagrangian is invariant under local SU(3) gauge transformations, Ω, we ensure that $[\psi_f]^a_\alpha(x)$ and $A^u_\mu(x)$ transform as

$$[\psi_f]^a_\alpha(x) \xrightarrow{\Omega} \Omega^{ab}(x)[\psi_f]^b_\alpha(x), \tag{2.14}$$

$$[t^u]^{ab} A^u_\mu(x) \xrightarrow{\Omega} \Omega(x)^{ac}[t^u]^{cd} A^u_\mu(x) \left[\Omega^{-1}(x)\right]^{db} + \frac{i}{g}\left(\partial_\mu \Omega(x)^{ac}\right)\left[\Omega^{-1}(x)\right]^{cb}, \tag{2.15}$$

where $\Omega(x)$ defines an independent SU(3) transformation at each point in spacetime, g is the QCD coupling constant and t^u are the eight 3×3 Gell-Mann matrices, the generators of SU(3), as described in Appendix A.3. Finally, we can redefine the covariant derivative in terms of the gluon field $A_\mu(x)^u$ as

$$\not{D}^{ab}_{\alpha\beta}(x) = \delta^{ab}\not{\partial}_{\alpha\beta} - ig[t^u]^{ab}\not{A}^u_{\alpha\beta}(x). \tag{2.16}$$

Putting this all together we can write our QCD Lagrangian as

$$\mathcal{L}_{QCD} = [\bar{\psi}_f]^a_\alpha(x)\left(i\not{D}^{ab}_{\alpha\beta} - m_f\delta_{\alpha\beta}\delta^{ab}\right)[\psi_f]^b_\beta(x) - \frac{1}{4}[G_{\mu\nu}]^u[G^{\mu\nu}]^u. \tag{2.17}$$

By expanding the covariant derivative and field strength tensor we can rewrite the Lagrangian in terms of the free quark field, the gluon field, and the interaction terms, as

$$\mathcal{L}_{QCD} = \mathcal{L}_Q + \mathcal{L}_G + \mathcal{L}_I, \tag{2.18}$$

where

$$\mathcal{L}_Q = [\bar{\psi}_f(x)]^a_\alpha \left(i\delta^{ab}\partial\!\!\!/_{\alpha\beta} - m_f\delta_{\alpha\beta}\delta^{ab}\right)[\psi_f(x)]^b_\beta, \tag{2.19}$$

$$\mathcal{L}_G = -\frac{1}{4}[G^{(0)}_{\mu\nu}(x)]^u[G^{(0),\mu\nu}(x)]^u. \tag{2.20}$$

The last term, $\mathcal{L}_I$, encoding the quark and gluon interactions, can be written as

$$\mathcal{L}_I = g[t^u]^{ab}\bar{\psi}^a_\alpha(x)\not{A}^u_{\alpha\beta}(x)\psi^a_\beta(x) - gf^{uvt}\partial_\mu A^u_\nu A^v_\mu A^t_\nu - \frac{g^2}{4}f^{uvw}f^{ust}A^v_\mu A^w_\nu A^{\mu,s}A^{\nu,t}. \tag{2.21}$$

The separate terms in the interaction term encode, from left to right, the quark-gluon vertex, the three gluon vertex, and the four gluon vertex, shown in Figure 2.3.

2.2.2. QCD Features

There are two important features exhibited by QCD which are not present in QED. The first is colour confinement. In nature, we can only observe colour neutral states, such as colour singlet mesons (quark-antiquark pairs) and baryons (three quark or three antiquark states). While this property is well observed, and holds true in all tests, the mechanism behind confinement is not well understood. Indeed, a proof of confinement is part of the 'Yang-Mills and Mass Gap' Millennium Problem [13]. We can think of this property being the result of it becoming energetically favourable to form quark-antiquark pairs in the vacuum when quarks are separated, forming two colour singlet states instead of the original quarks being isolated.

The second important feature possessed by QCD is asymptotic freedom [14, 15]. This is a feature unique to non-Abelian GFTs. In a theory such as QED, as isolated electric charge will polarise the surrounding vacuum, creating a shell of virtual electron-positron pairs around itself. This shell 'screens' the charge, and in effect reduces the effective electromagnetic coupling at long distances. A similar effect takes places in QCD, where a quark will polarise the vacuum around it, this time in colour, which forms a shell of screening quarks. Unlike photons in QED, however, the gluons also carry colour charge. This means that a quark will surround it self with a cloud of virtual gluons, which act to 'anti-screen' the colour charge, opposite to the screening quarks. These anti-screening gluons will dominate the screening quarks, as long as the QCD β

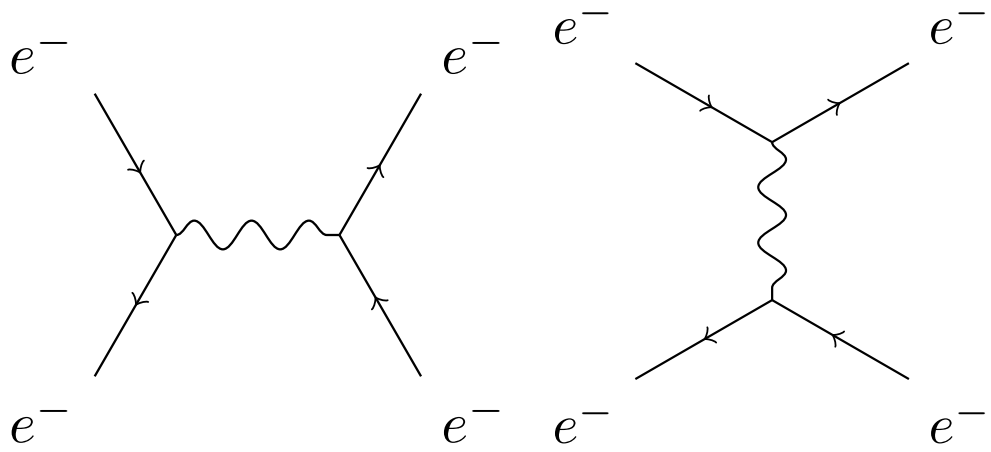

Figure 2.4. Lowest-order Feynman diagrams for electron-positron scattering in QED. Again considering time to flow from left to right, the left diagram shows electron-positron annihilation and creation, while the right diagram shows one-photon exchange.

function is negative (shown to leading order):

$$\beta(g) = -\beta_0 \frac{g^3}{16\pi^2}, \tag{2.22}$$

where

$$\beta_0 = 11 - \frac{2}{3} N_f, \tag{2.23}$$

where N_f is the number of quark flavours. We find that Eq. 2.22 is negative for $N_f < 17$, which is the case in the SM, so the anti-screening effect dominates, and we find that the QCD strong coupling α_s is suppressed at high energy, or short distances. These features can lead to difficulties when using conventional methods to calculate QCD interactions, particularly at low energy.

In Quantum Field Theories (QFTs) we can write scattering amplitudes, which relate to experimental cross-sections and decay rates, in terms of a series of Feynman diagrams. Feynman diagrams are a diagrammatic way of expressing particle interactions in terms of propagating particles and interaction vertices, which map directly to the mathematical expression of the interaction. Figure 2.4 shows the leading order electron-positron scattering diagrams in QED. Each vertex in the diagram contributes a factor of the effective coupling, and so long as the QFTs effective couplings are sufficiently small, higher order terms contribute a smaller amount to the total scattering

amplitude, such that we can systematically truncate the sum at our desired precision. When performing this truncation, we call the calculation perturbative, and can use this method to calculate the scattering amplitude as a finite series of sums.

QED is one such theory. We can see in Figure 2.4 that the leader order electron-positron diagrams only contain 2 vertices, so contribute proportionally to the QED coupling squared, $e^2/(4\pi) = \alpha_{EM} \approx \frac{1}{137}$. The next-order scattering diagrams have 4 vertices, and so contribute at $\alpha_{EM}^2 \approx 5 \times 10^{-5}$, and so on for subsequent order terms. Because of the suppression of higher order contributions, very few terms need to be calculated to get a very precise result.

In QCD, the strong coupling, written to leading order, is

$$\alpha_S\left(Q^2\right) = \frac{4\pi}{\beta_0 \ln \frac{Q^2}{\Lambda_{\text{QCD}}^2}}, \tag{2.24}$$

where β_0 is described in Eq. 2.23, and Λ_{QCD} is the QCD scale, ≈ 0.2 GeV. Figure 2.5 shows the running of the effective QCD coupling determined experimentally. At high energies, the strong coupling is small, and the perturbative methods used in QED can also be used in QCD. As we move to the lower energy scales used in hadronic studies, the strong coupling $\alpha_S \approx 1$. At this energy scale perturbative methods are no longer appropriate as the higher order diagrams contribute at a similar scale to, or even larger than, the lower order diagrams to the total scattering amplitude. Due to this effect, understanding low energy QCD interactions requires a non-perturbative method. Lattice Gauge Theory provides one such ab-initio method of investigating QCD at low energy. This will be discussed in Chapter 4.

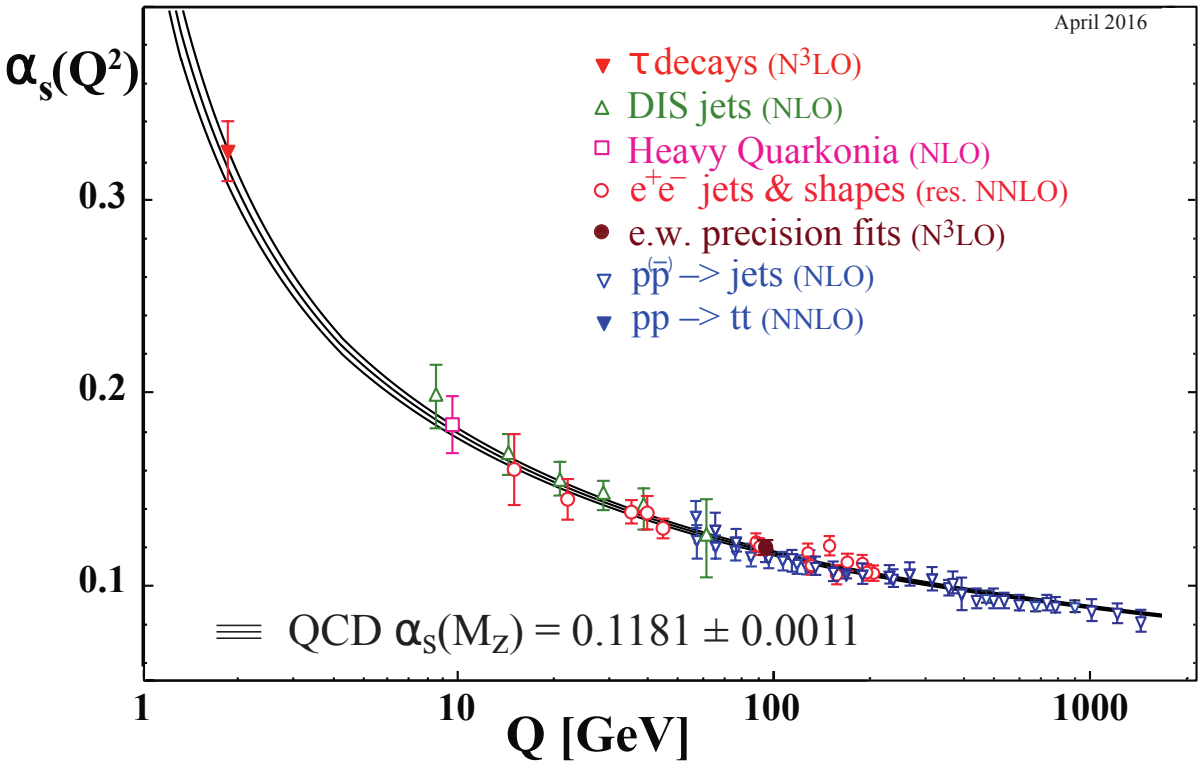

Figure 2.5. Running of the QCD coupling α_s obtained from experimental measurements, as a function of the energy scale Q. Reprinted from Tanabashi *et al* [16]

Chapter 3.

Anomalous Magnetic Moment of the Muon

The magnetic moment of a charged particle, $\vec{\mu}$, can be found from the Dirac equation of relativistic quantum mechanics,

$$\vec{\mu} = g\frac{e}{2m}\vec{S}, \tag{3.1}$$

where e is the charge of the particle, m is the mass of the particle, $\vec{S}$ is the spin, and g is a unitless quantity known as the g-factor [17]. For leptons, the g-factor was thought to be 2.

However, in 1948 Julian Schwinger published the first calculation of a radiative correction in QED; the $\alpha/2\pi$ mass-independent correction to the electron magnetic moment [1],

$$g_e = 2\left(1 + \frac{\alpha}{2\pi}\right). \tag{3.2}$$

This calculation agreed within errors with experimental results by Kush and Foley in [2]. This deviation from $g = 2$ is referred to as the anomalous magnetic moment, or simply "$g - 2$" coming from the equation

$$a = \frac{g-2}{2}, \tag{3.3}$$

where a is the value of the anomalous magnetic moment.

The anomalous magnetic moment of the electron has since been measured experimentally to a precision of better than than 1 part per billion [4], and calculated using the SM to a similar precision [3]. These values agree to more than 10 significant figures, which makes the anomalous magnetic moment of the electron one of the most accurately verified predictions in physics.

For the muon, on the other hand, the anomalous magnetic moment is less well known. The current experimental value is known to a precision of 0.54 ppm [18, 19]:

$$a_\mu^{\text{exp}} = 11\,659\,209.1(54)(33) \times 10^{-10}, \tag{3.4}$$

with current experiments underway which hope to improve on the precision by a factor of 4. The SM calculation for the muon anomalous magnetic moment is more complicated than that of the electron, since electroweak (EW) and, in particular, QCD contributions play a much more significant role for the muon, due to the muon's much larger mass,

$$\frac{m_\mu}{m_e} \approx 200. \tag{3.5}$$

The SM value of the anomalous magnetic moment of the muon can be expressed in terms of the separate SM contributions: QED, EW and QCD terms, which will be discussed in more detail later in this chapter. Based on the results from [20–39], and combined into a single value for a_μ^{SM} in [5], the SM value is found to be

$$a_\mu^{\text{SM}} = 11\,659\,181.0(43) \times 10^{-10}. \tag{3.6}$$

We find that unlike the case of the electron, the SM value in Eq. 3.6 does not agree with the experimentally measured result in Eq. 3.4. In fact, the difference is

$$\Delta a_\mu = a_\mu^{\text{exp}} - a_\mu^{\text{SM}} = 28.1(76) \times 10^{-10}, \tag{3.7}$$

corresponding to a 3.7σ discrepancy.

This discrepancy is of great interest in the search for new physics. We expect the sensitivity to new physics to grow quadratically with the mass of the lepton, so with respect to the electron, the sensitivity of a_μ should increase by a factor of $(m_\mu/m_e)^2 \sim 4 \times 10^4$ compared to a_e. If the discrepancy remains as we increase the precision of our

calculations and measurements, it will be a sure sign of the presence of new physics beyond the standard model. If, on the other hand, the difference fades away as the theory and experimental values converge, it will provide some severe constraints to any new physics.

3.1. Experiment

Currently, the best experimental results for a_μ are from the Brookhaven Experiment E821 [18], which finished in 2006, although new results from Fermilab's E989 experiment are expected very soon. Here we will provide only a brief overview of the experiment, with more details being available in [18].

Muons are injected into a storage ring with constant magnetic field $\vec{B}$, and precess along a circle with the Larmor frequency

$$\omega_p = -\frac{q\vec{B}}{m_\mu \gamma}, \tag{3.8}$$

where γ is the Lorentz factor. Due to the anomalous magnetic moment, there is a small change in the precession of the spin with respect to the momentum,

$$\omega_s = -\frac{ge\vec{B}}{2m_\mu} - (1-\gamma)\frac{q\vec{B}}{m_\mu \gamma}. \tag{3.9}$$

This precession of the spin is shown in Figure 3.1.

By measuring the difference between the Larmor frequency of the spin and momentum,

$$\begin{aligned} \omega_a &= \omega_s - \omega_p \\ &= -\left(\frac{g-2}{2}\right)\frac{q\vec{B}}{m_\mu} \\ &= -a_\mu \frac{q\vec{B}}{m_\mu}, \end{aligned} \tag{3.10}$$

we have a direct way to measure a_μ, provided $\vec{B}$ is well known.

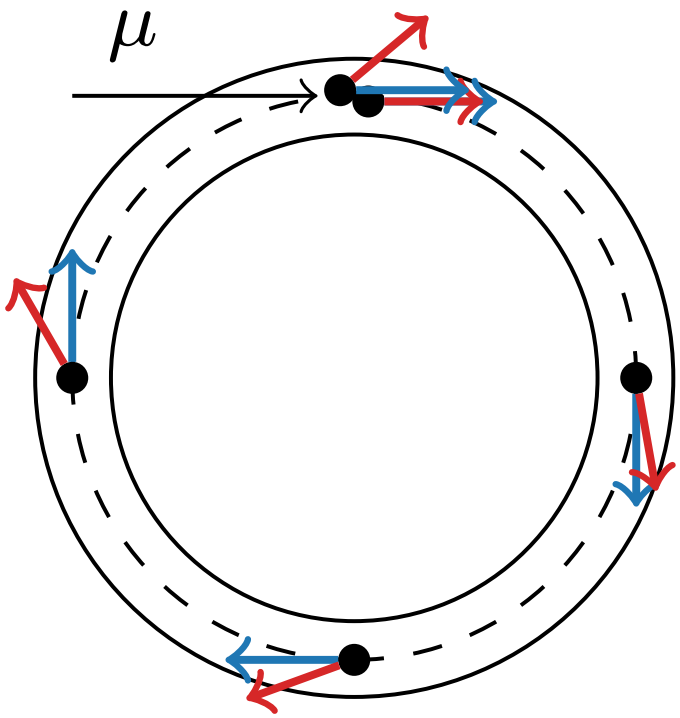

Figure 3.1. Simplified diagram of the experimental setup used in Brookhaven E821. The muon beam is injected at the top, when they circle around the storage ring. The spin (shown in red) is seen to precess with respect to the momentum (blue) as the beam moves though the magnetic field. Diagram adapted from [40]

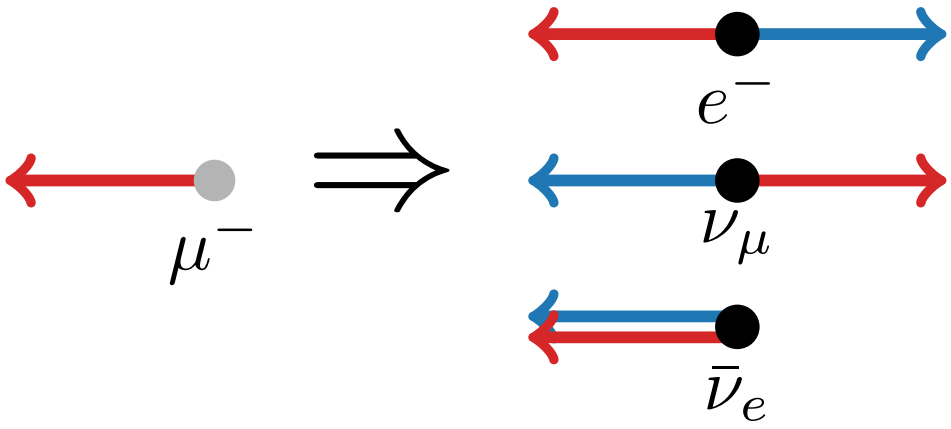

Figure 3.2. Dominant decay pattern of the muon to electron and neutrinos. Momentum is shown in blue, spin in red. Note that the electron momentum is anti-parallel to the muon spin.

The Larmor frequency of the spin can be measured by observing the decay of the muon to an electron and neutrinos. Due to the chiral nature of the weak interaction, the emerging electron has momentum preferentially anti-parallel to the muon spin, shown in Figure 3.2.

Currently Fermilab is running a similar experiment, reusing some of the equipment from E821. This experiment, labelled E989, aims to improve on the current experimental uncertainty by a factor of 4 [7]. This experiment is well underway, and is in the process of analysing data from the first run. J-PARC also has an muon $g-2$ experiment (E34) in development [8].

3.2. Standard Model

As mentioned at the start of this chapter, the SM prediction for the anomalous magnetic moment of the muon can be broken up into three separate contributions: QED, EW and QCD contributions. The QCD contribution is also referred to as the hadronic contribution, and both terms are used interchangeably. We can write this as

$$a_\mu = a_\mu^{\text{QED}} + a_\mu^{\text{EW}} + a_\mu^{\text{QCD}}. \tag{3.11}$$

The QED contribution is by far the largest contribution to the anomalous magnetic moment, contributing at [36]

$$a_\mu^{\text{QED}} = 116\,584\,71.8931(104) \times 10^{-10}, \tag{3.12}$$

accounting for over 99% of the total contribution to a_μ. Despite this term being so dominant in the final SM prediction for a_μ, the QED term is incredibly precisely known, so contributes the least uncertainty to the total value.

The EW contribution is the smallest term, coming in at [38, 39]

$$a_\mu^{\text{EW}} = 15.36(10) \times 10^{-10}. \tag{3.13}$$

The QCD, or hadronic, contribution accounts for the majority of the SM uncertainty, contributing at [20–35, 41–46]

$$a_\mu^{\text{QCD}} = 693.7(43) \times 10^{-10}. \tag{3.14}$$

In the following sections we will give a brief break down how each of these contributions are currently calculated. Much of these sections are based on the 2020 review of the field, *The anomalous magnetic moment of the muon in the Standard Model* [5].

3.2.1. Pure QED

The QED contribution can be expressed as the sum of successive powers of the fine structure constant, α, and orders of Feynman loop diagrams,

$$a_\mu^{\text{QED}} = \left(\frac{\alpha}{\pi}\right) A^{(2)} + \left(\frac{\alpha}{\pi}\right)^2 A^{(4)} + \left(\frac{\alpha}{\pi}\right)^3 A^{(6)} + ..., \tag{3.15}$$

where $A^{(n)}$ is the contribution of order e^n.

The leading order QED contribution is shown in Figure 3.3, and is mass independent, so is the same as the leading order contribution to the electron anomalous magnetic moment, determined by Schwinger, contributing $A^{(2)} = \frac{1}{2}$.

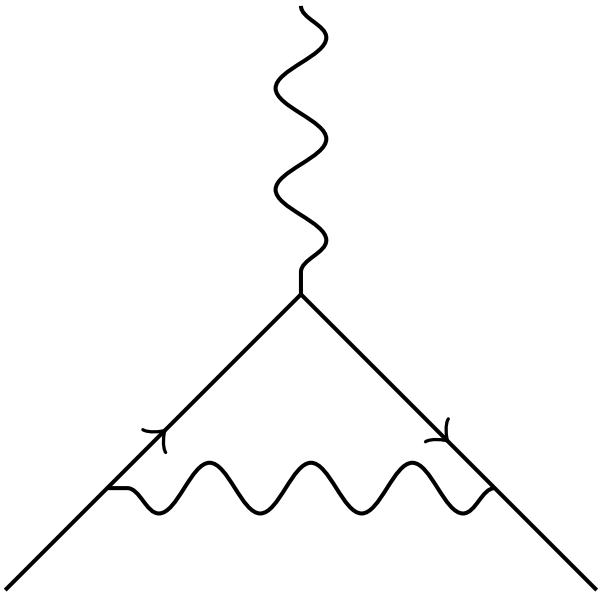

Figure 3.3. Second-order contributions, responsible for the leading order QED contribution to the anomalous magnetic moment.

The next leading order comes from fourth-order contributions in e, of which there are seven diagrams, shown in Figure 3.4. From fourth-order and higher, we start to get a mix of mass-independent and mass-dependent terms, and the lepton anomalous magnetic moments start to differ. At sixth-order, there are 72 diagrams, eighth-order has 891, and tenth order has 12 672 diagrams.

The fourth and sixth order contributions have been fully calculated analytically. For the mass-independent terms, the eighth order contributions have also been calculated analytically, but the mass-dependent terms rely on numerical evaluation. Tenth-order contributions have been numerically calculated [3, 5]. These tenth-order QED contributions are estimated to contribute at roughly 5×10^{-11}, comparable to the target precision of the new E989 at Fermilab, $\sim 1.5 \times 10^{-11}$. Higher order terms have only been estimated, but are expected to contribute at less than the E989 precision.

3.2.2. Electro-weak

The EW contributions to a_μ consist of any contribution containing the EW bosons W, Z, or the Higgs. The EW terms have been numerically calculated for one and two-loop terms, of which a selection are shown in Figure 3.5, as well as the leading order three-

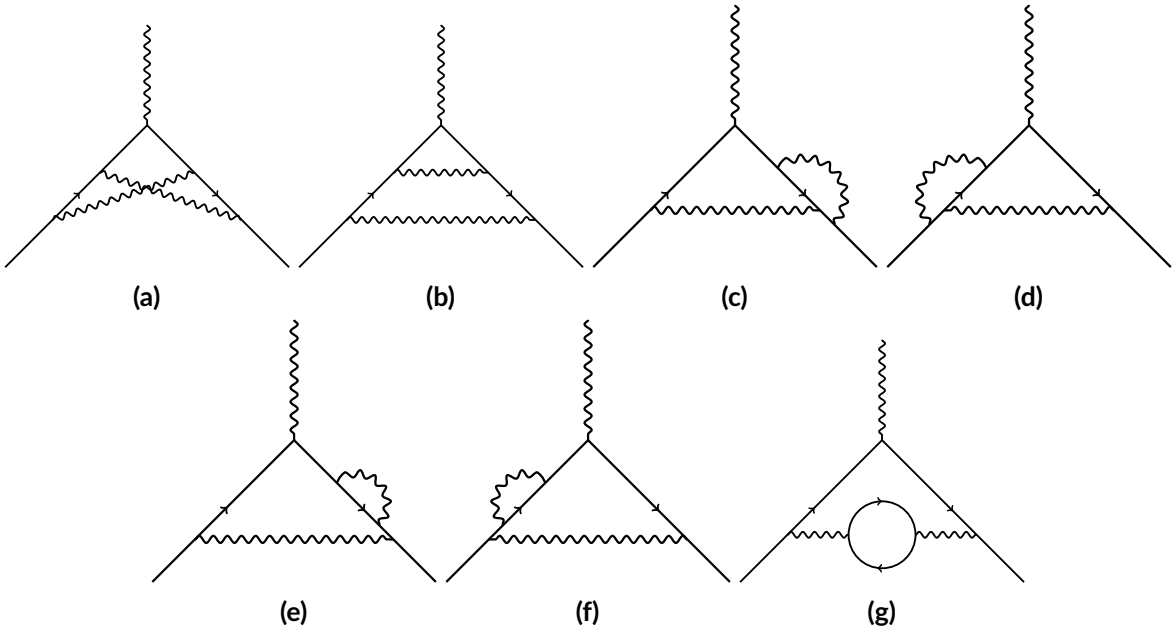

Figure 3.4. Feynman diagrams of Fourth-order contributions. Note that (c) and (d), and (e) and (f), are mirrored in time.

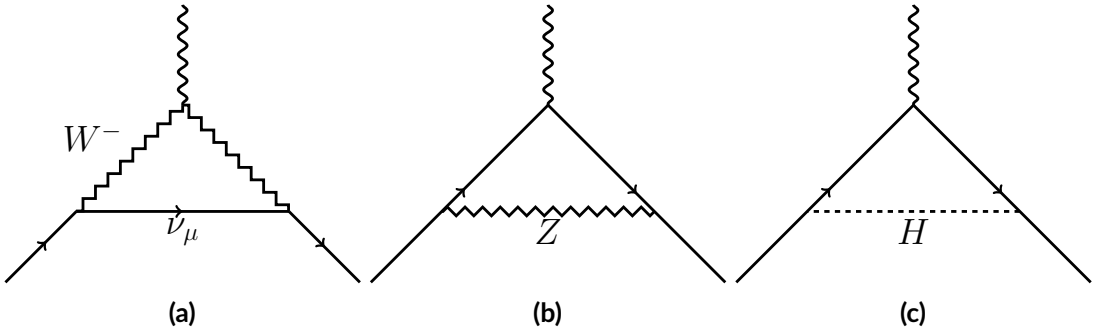

Figure 3.5. The lowest order EW contribution Feynman diagrams.

loop terms. The remaining three-loop contributions have been estimated to be below a percent of the two-loop contributions, and have been neglected for now [38].

As the EW contributions are so small, only the two-loop and leading three-loop terms contributions need to be considered. This smallness is in part due to a suppression from the ratio $m_\mu^2/m_W^2 \approx 10^{-6}$. However, this is still $\sim 40\,000$ times more significant than in the case of the anomalous magnetic moment of the electron. This enhancement makes a_μ much more sensitive to EW contributions, and hence any new physics models which may contribute in this sector.

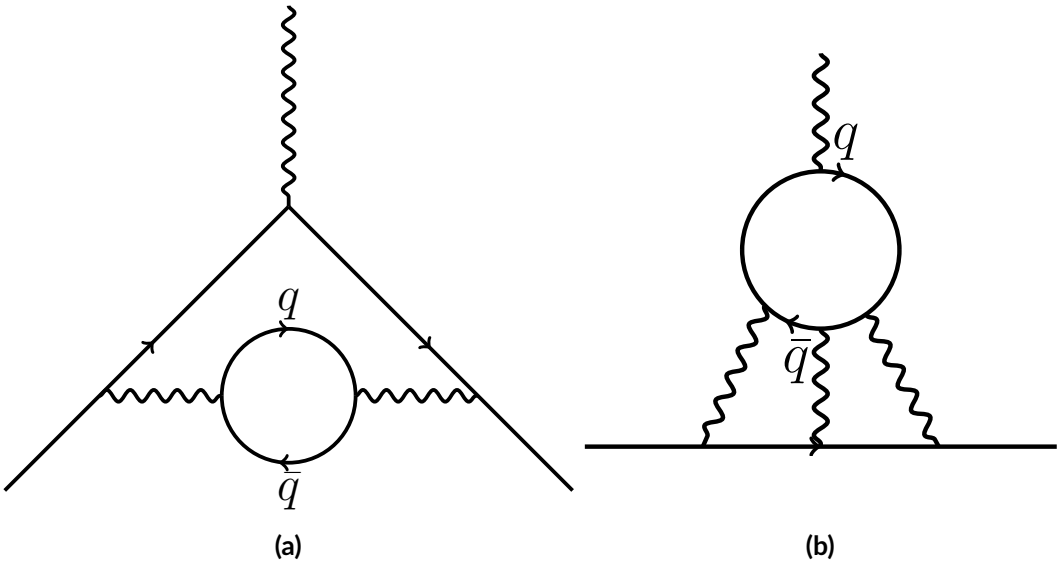

Figure 3.6. Leading order diagrams for HVP and HLbL

3.2.3. Hadronic

As mentioned at the start of this section, the uncertainty of the SM calculation is dominated by the hadronic sector, and as such has been the focus of a lot of attention over the past few years. In order to fully take advantage of any significant improvement in the experimental result from up-coming experiments, the hadronic uncertainty must be improved.

The hadronic contribution is further split into two contributions: the hadronic vacuum polarisation (HVP) and hadronic light by light (HLbL). The HVP term enters at $\left(\frac{\alpha}{\pi}\right)^2$, while HLbL enters at $\left(\frac{\alpha}{\pi}\right)^3$. Both these contributions are shown (to leading order) in Figure 3.6.

As QCD is non-perturbative, we are unable to calculate some finite number of Feynman diagrams up to a given contribution where the value becomes smaller than the experimental uncertainty, as done in the QED and EW case. Instead a non-perturbative calculation is required.

Hadronic Light by Light

HLbL scattering is complicated to calculate, due to the many contributions which go into it, which until recently have relied on multiple models and sets of experimental

input. The $g-2$ white paper [5] explains all these contributions in some detail, which will not be repeated here. In this context of this thesis, it is enough to know that the HLbL represents the second largest contribution to the uncertainty of a_μ, and current best estimates are

$$9.2(18) \times 10^{-10}, \tag{3.16}$$

combining results from phenomenology and lattice, presented in [27–35, 41–46].

Hadronic Vacuum Polarisation

The HVP term is responsible for most of the hadronic uncertainty. Currently, the best estimate for a_μ^{HVP} is obtained using the dispersion relation to calculate the cross section of a virtual photon decaying into hadrons. This cross section is determined using experimental data for $e^+e^- \to$ hadrons. At leading order, the dispersion integral is [47, 48]

$$a_\mu^{\text{HVP,LO}} = \frac{\alpha^2}{3\pi^2} \int_{M_\pi^2}^{\infty} \frac{K(s)}{s} R(s) ds, \tag{3.17}$$

where $K(s)$ is a known kernel function, and $R(s)$ is the hadronic R-ratio

$$R(s) = \frac{\sigma^0(e^+e^- \to \text{hadrons}(+\gamma))}{\sigma_{pt}}, \quad \sigma_{pt} = \frac{4\pi\alpha^2}{3s}. \tag{3.18}$$

The kernel term $K(s)/s$ in Eq. 3.17 leads to contributions from the lowest energies being weighted most strongly. This results in the two-pion channel being the dominant contribution at more than 70% of $a_\mu^{\text{HVP,LO}}$ [5].

As the $\pi^+\pi^-$ channel is the dominant contribution to $a_\mu^{\text{HVP,LO}}$, these results need to be known to the highest precision, and have have been the focus of many experimental measurements.

While there has been success in producing results with high precision, the two most precise measurements, by KLOE [49] and BABAR [50], do not agree within their quoted uncertainties. Figure 3.7 (reprinted from [49]) shows the ratio of measurements by BABAR with the KLOE cross section, which show the discrepancy between KLOE and BABAR.

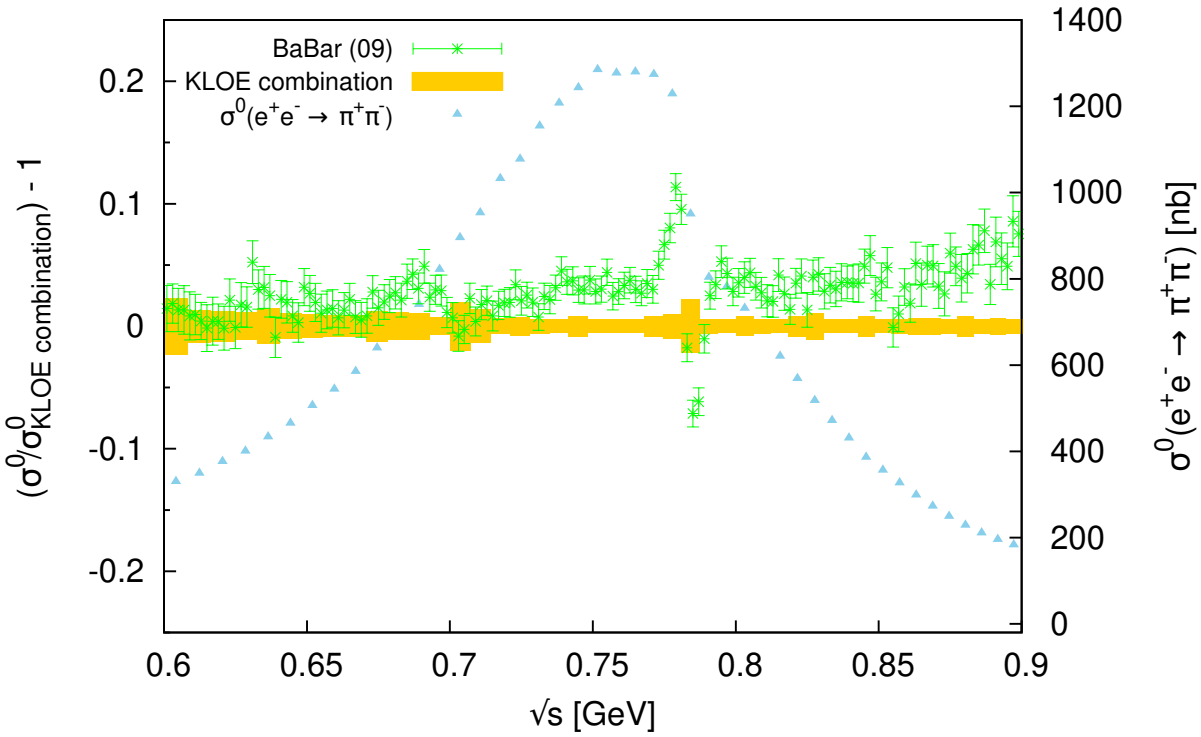

Figure 3.7. $\pi^+\pi^-$ cross section from the KLOE combination compared to the BaBar cross section. KLOE results are represented by the yellow band, and BaBar results with the green points. Reprinted from Anastasi *et al* [49].

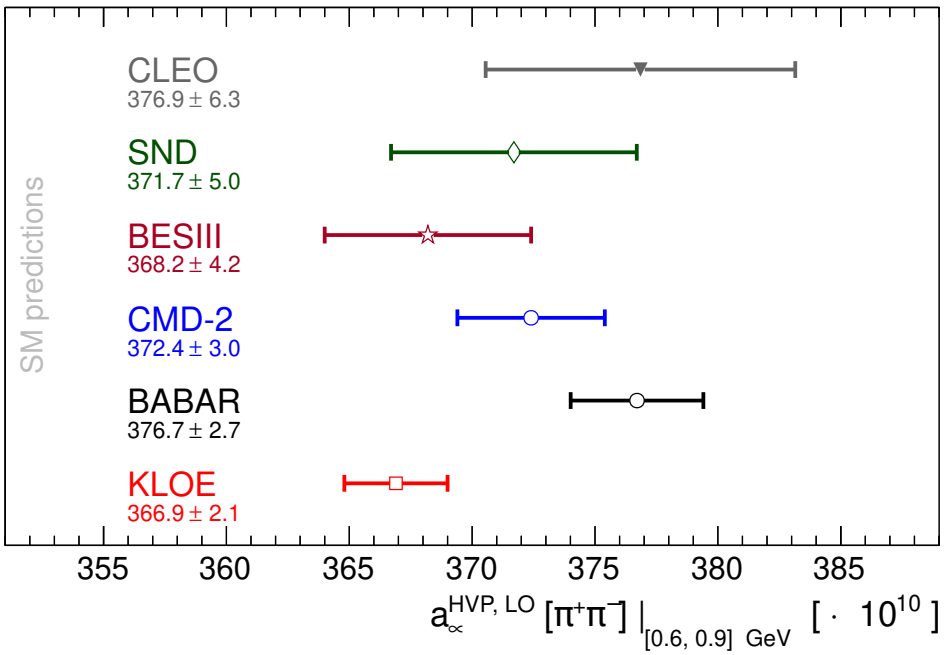

Figure 3.8. Comparison of results for the $\pi^+\pi^-$ channel contribution to $a_\mu^{\text{HVP,LO}}$ from 0.6 to 0.9 GeV, as found from various experiments [49–55]. The disagreement between KLOE and BaBar is clearly shown, and other experimental results are unable to distinguish between these two results. Reprinted from Aoyama *et al.* [5]

Results from other experiments are currently insufficiently precise at the moment to resolve this discrepancy. If we look at the contribution to $a_\mu^{\text{HVP,LO}}$ from the $\pi^+\pi^-$ cross section results from individual experiments, as shown in Figure 3.8, we find that the results from other experiments [49–55] generally lie between KLOE and BABAR, agreeing with both.

The cause of this disagreement is not currently understood, but while this tension exists the desired precision for the overall SM calculation of a_μ cannot be reached, at least not without an alternative method to calculate the HVP term.

The current world average for the HVP term using the scattering cross-sections compiled by [5] is

$$a_\mu^{\text{HVP}} = 684.5(40) \times 10^{-10}, \tag{3.19}$$

$$a_\mu^{\text{HVP,LO}} = 693.1(40) \times 10^{-10}. \tag{3.20}$$

The leading order term has been quoted separately here as it will be useful to compare with later.

One such alternative method is Lattice, which we will discuss in the next chapter, Chapter 4, and will be used to look at the anomalous magnetic moment throughout the rest of this thesis. Current calculations for the HVP term using lattice results have a higher uncertainty than those using the data driven methods discussed above, but these lattice results are also quite young, and there is a lot of work going into improving the precision of these results.

Details on the methods used to calculate the HVP term will be explored in Chapter 7. Here we will have a look at the current state of lattice results, and motivate how we might seek to improve them.

Hadronic Vacuum Polarisation - Lattice

Currently the world average lattice result for the leading order HVP term is [56–64]

$$a_\mu^{\text{HVP,LO}} = 711.6(184) \times 10^{-10}, \tag{3.21}$$

however, as this is a very active area of research many results are being published so this should not be considered a constant value, but does serve to give context for the state of research. Currently lattice is only able to give results for the leading order contribution, but as this is where almost all the uncertainty comes from, this is not an issue. When referring to lattice results, we are always referring to the leading order contribution, unless otherwise noted.

One thing to note is that many of the lattice results are based on pure QCD, or include some form of *quenched*-QED. Currently there only exists one result for a fully dynamical QCD +QED lattice calculation [9]. One can think of the pure-QCD HVP term as being when the hadronic loop in Figure 3.6 containing only gluon interactions, and neglecting any photon interactions between the quarks in the loop. The most common form of quenched-QED is to include QED interactions between the valance quarks which form the loop, but only include QCD interactions between those valance quarks and the background *sea* quarks.

As there exists tensions between the results of different lattice groups for the light-quark connected contributions, it makes computing a second fully dynamical QCD+QED calculation imperative if we want to fully understand the QED corrections and push towards more precise calculations.

Chapter 4.

Lattice

Lattice Field Theory is an ab-initio method first proposed in 1973 [65], by which we are able to study QCD non-perturbatively.

Lattice QCD is based on the path integral formalisation of QCD [66], in which the expectation values of operators are expressed as weighted integrals over fermion and gauge field configurations. By introducing a grid of discretised space-time coordinates, these integrals can be evaluated using high-performance computing resources. This necessitates the introduction of a finite lattice volume, and non-zero spacing between the lattice sites, which introduce infrared and ultraviolet cutoffs, which must be accounted for.

In this chapter we will describe the theoretical formulation of lattice QCD, and look at how this can be extended to include QED interactions.

4.1. Lattice QCD

4.1.1. Path Integral

In a QFT such as QCD, we can calculate observables from vacuum expectation values using the Feynman path integral formalisation. The expectation value for some operator $\mathcal{O}[\psi, \bar{\psi}, A^\mu]$ is given by

$$\langle \Omega | \mathcal{O}[\psi, \bar{\psi}, A^\mu] | \Omega \rangle = \frac{1}{\mathcal{Z}} \int \mathcal{D}\psi \mathcal{D}\bar{\psi} \mathcal{D}A^\mu \mathcal{O}[\psi, \bar{\psi}, A^\mu] \exp\left(i\mathcal{S}_{\text{QCD}}[\psi, \bar{\psi}, A^\mu]\right), \tag{4.1}$$

for all possible quark/anti-quark fields $\psi/\bar{\psi}$, and gluon field A^μ, at all possible points in space-time, where $|\Omega\rangle$ denotes the vacuum state. The QCD action, $\mathcal{S}_{\text{QCD}}$, is given by the integral of the Lagrangian over space-time

$$\mathcal{S}_{\text{QCD}}[\psi, \bar{\psi}, A^\mu] \equiv \int d^4x \mathcal{L}_{\text{QCD}}(x), \tag{4.2}$$

and the partition function $\mathcal{Z}$ is

$$\mathcal{Z} = \int \mathcal{D}\psi \mathcal{D}\bar{\psi} \mathcal{D}A^\mu \exp\left(i\mathcal{S}_{\text{QCD}}[\psi, \bar{\psi}, A^\mu]\right). \tag{4.3}$$

This partition function is reminiscent of the partition function from statistical mechanics [67]. The major difference between the two is that the exponent appearing in the lattice partition function is complex instead of real and negative. If we can rewrite the exponent in a real, negative form, then we can use the methods of statistical mechanics. We do this by formulating the theory in Euclidean space-time by performing a Wick rotation

$$t \to -it, \tag{4.4}$$
$$\vec{x} \to \vec{x}, \tag{4.5}$$
$$A^0 \to iA_4, \tag{4.6}$$
$$\mathcal{S}_{\text{QCD}} \to i\mathcal{S}^{\text{Eucl.}}_{\text{QCD}}, \tag{4.7}$$

and the gamma matrices are expressed in a Euclidean representation (see Appendix A.2). In the Euclidean formulation the metric $\delta_{\mu\nu} = \text{diag}(+1, +1, +1, +1)$, so we no longer need to distinguish between covariant and contravarient indices [68].

The partition function can now be expressed in a form compatible with statistical mechanics

$$\mathcal{Z} = \int \mathcal{D}\psi \mathcal{D}\bar{\psi} \mathcal{D}A^\mu \exp\left(-\mathcal{S}^{\text{Eucl.}}_{\text{QCD}}[\psi, \bar{\psi}, A^\mu]\right). \tag{4.8}$$

Using this representation, we are able to interpret the vacuum expectation value from Eq. 4.1 as the weighted average of the operator over all possible field configurations. This set of field configurations are distributed with the probability [69]

$$P[\psi, \bar{\psi}, A^\mu] \propto \exp\left(-\mathcal{S}^{\text{Eucl.}}_{\text{QCD}}[\psi, \bar{\psi}, A^\mu]\right). \tag{4.9}$$

The vacuum expectation value can then be calculated as the average value of the operator across the set of field configurations. We can then approximate the vacuum expectation value as the weighted average across some sub-ensemble of N gauge fields, generated with a probabilistic weight given in Eq. 4.9,

$$\langle\Omega|\mathcal{O}[\psi,\bar{\psi},A^{\mu}]|\Omega\rangle \approx \frac{1}{N}\sum_{i=1}^{N}\mathcal{O}_i[\psi,\bar{\psi},A^{\mu}]. \tag{4.10}$$

4.1.2. Discretisation

In order to evaluate such expectations, we need to write the theory in such a way that we are able to represent it on a computer. This involves defining the theory in terms of finite operators such as sums instead of integrals, and representing continuous space as a set of discrete locations. This process is know as discretisation [65].

We can approximate the continuous space-time, x^{μ}, with a four-dimensional grid of space-time points, referred to as a *lattice*. This is done via the transformation

$$x^{\mu} \rightarrow x^{\mu} = an^{\mu}, \tag{4.11}$$

where $n^{\mu} \in \mathbb{Z}^4$ are integer coordinates in lattice space, marking the vertices of the lattice, and a, the *lattice spacing*, that is, the spacing between vertices on the lattice. By discretising space-time in this way, the fermion fields $\psi(x)$ are restricted to exist on the vertices of the lattice, or the lattice sites. In order to use this lattice in numerical calculations, we restrict the lattice extents to a finite subset $\mathbb{L} \subset \mathbb{Z}^4$. Typically the spatial dimensions are chosen to be the same, such that the lattice space-time volume

$$V = L_s^3 \times L_t = (N_s a)^3 \times (N_t a), \tag{4.12}$$

where N_s, N_t are integers and refer to the number of sites in the spatial and temporal directions respectively.

By discretising space-time in this way, we can replace derivatives with finite differences

$$\partial_{\mu}\psi(x) \rightarrow \frac{1}{2a}\big(\psi\left(x+a\hat{\mu}\right) - \psi\left(x-a\hat{\mu}\right)\big), \tag{4.13}$$

where $\hat{\mu}$ is a unit-vector in the μ direction, and integrals over Euclidean space-time can be replaced with sums over the lattice volume

$$\int d^4x \to a^4 \sum_{n^\mu} = \sum_{x^\mu}. \tag{4.14}$$

Recalling our fermion field transformations under a local gauge transformation from Eq. 2.14, we can consider the discretised derivative

$$\partial_\mu \psi(x) \xrightarrow{\Omega} \frac{1}{2a}\big(\Omega\left(x + a\hat{\mu}\right)\psi\left(x + a\hat{\mu}\right) - \Omega\left(x - a\hat{\mu}\right)\psi\left(x - a\hat{\mu}\right)\big). \tag{4.15}$$

As this is not gauge covariant, we restore gauge covariance by introducing the gluon fields as links between the lattice sites. These take the form of parallel transport operators from one lattice site to the next

$$U_\mu(x) \equiv P \exp\left(-ig\int_x^{x+a\hat{\mu}} dz_\mu A_\mu(z)\right), \tag{4.16}$$

where P denotes the path ordering. The link variables also have the property that Hermitian conjugation 'reverses' the link:

$$U_\mu^\dagger(x) = U_{-\mu}(x + a\hat{\mu}). \tag{4.17}$$

Figure 4.1 shows a two-dimensional representation of the discretised space-time in the $\mu - \nu$ plane, with the fermion field $\psi(x)$ and link variable $U_\nu(x)$ shown.

Under a local gauge transformation, the gluon fields transform as

$$U_\mu(x) \xrightarrow{\Omega} \Omega(x)U_\mu(x)\Omega^\dagger(x + a\hat{\mu}), \tag{4.18}$$

$$U_\mu^\dagger(x) \xrightarrow{\Omega} \Omega(x + a\hat{\mu})U_\mu^\dagger(x)\Omega(x)^\dagger. \tag{4.19}$$

We can then define the covariant finite difference operator, in analogy to Eq. 2.16, as

$$\nabla_\mu(x)\psi(x) \equiv \frac{1}{2a}\big(U_\mu(x)\psi(x + a\hat{\mu}) - U_\mu^\dagger(x - a\hat{\mu})\psi(x - a\hat{\mu})\big), \tag{4.20}$$

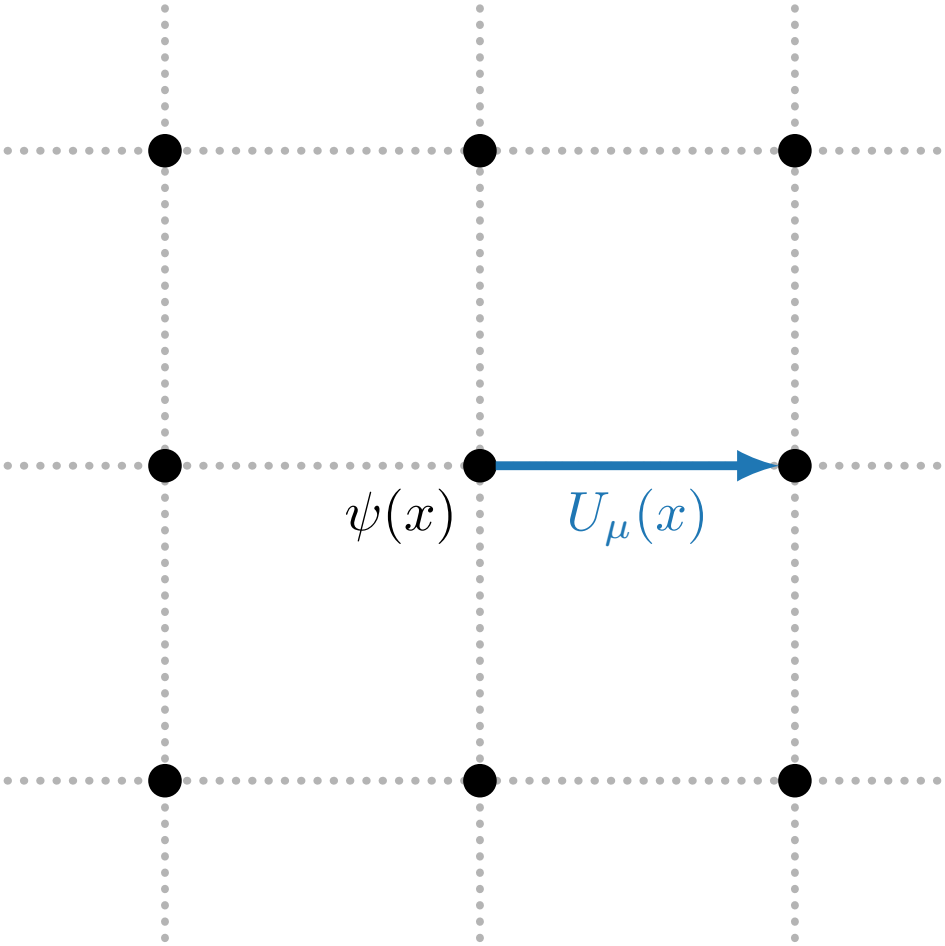

Figure 4.1. Two-dimensional representation of a discretised section of space-time. $\psi(x)$ is the fermion field at the lattice site x, while $U_\mu(x)$ is the link variable going from x to $x + a\mu$.

which transforms under a local gauge transformation as

$$\nabla_\mu(x)\psi(x) \xrightarrow{\Omega} \Omega(x)\nabla_\mu(x)\psi(x). \tag{4.21}$$

Note that as $a \to 0$, $\nabla_\mu \to D_\mu$.

Using these formulations for discretised quark and gluon fields, and lattice forms of integrals and covariant derivatives, we can derive a discretised form of the QCD action

$$\mathcal{S}^{\text{Latt}}_{\text{QCD}}[\psi, \bar{\psi}, U_\mu] = \mathcal{S}^{\text{Latt}}_{\text{G}}[U_\mu] + \mathcal{S}^{\text{Latt}}_{\text{F}}[\psi, \bar{\psi}, U_\mu]. \tag{4.22}$$

4.1.3. Gluonic action

Starting with the gluonic term in our QCD action, $\mathcal{S}^{\text{Latt}}_{\text{G}}[U_\mu]$, we want to write this in a gauge invariant form that goes to the Euclidean gauge action

$$\int d^4x \frac{1}{2} G^{\mu\nu}(x) G^{\mu\nu}(x) \tag{4.23}$$

in the continuum limit $a \to 0$.

Recalling Eq. 4.16, it is easy to see that a series of link variables forming a closed loop is gauge invariant. The simplest form of this, known as a plaquette, as shown in Figure 4.2, is

$$\begin{aligned} P_{\mu\nu}(x) &\equiv U_\mu(x) U_\nu(x + a\hat{\mu}) U_{-\mu}(x + a\hat{\mu} + a\hat{\nu}) U_{-\nu}(x + a\hat{\nu}) \\ &= U_\mu(x) U_\nu(x + a\hat{\mu}) U^\dagger_\mu(x + a\hat{\nu}) U^\dagger_\nu(x). \end{aligned} \tag{4.24}$$

The plaquette takes the value (see Appendix B.1 for details)

$$P_{\mu\nu}(x) = \exp\left(iga^2 G_{\mu\nu}(x) + \mathcal{O}(a^3)\right). \tag{4.25}$$

Expanding this form for the plaquette using a Taylor expansion, we get

$$P_{\mu\nu}(x) = \mathbb{I} + iga^2 G_{\mu\nu}(x) - \frac{1}{2} g^2 a^4 G_{\mu\nu}(x) G_{\mu\nu}(x) + \mathcal{O}(a^3). \tag{4.26}$$

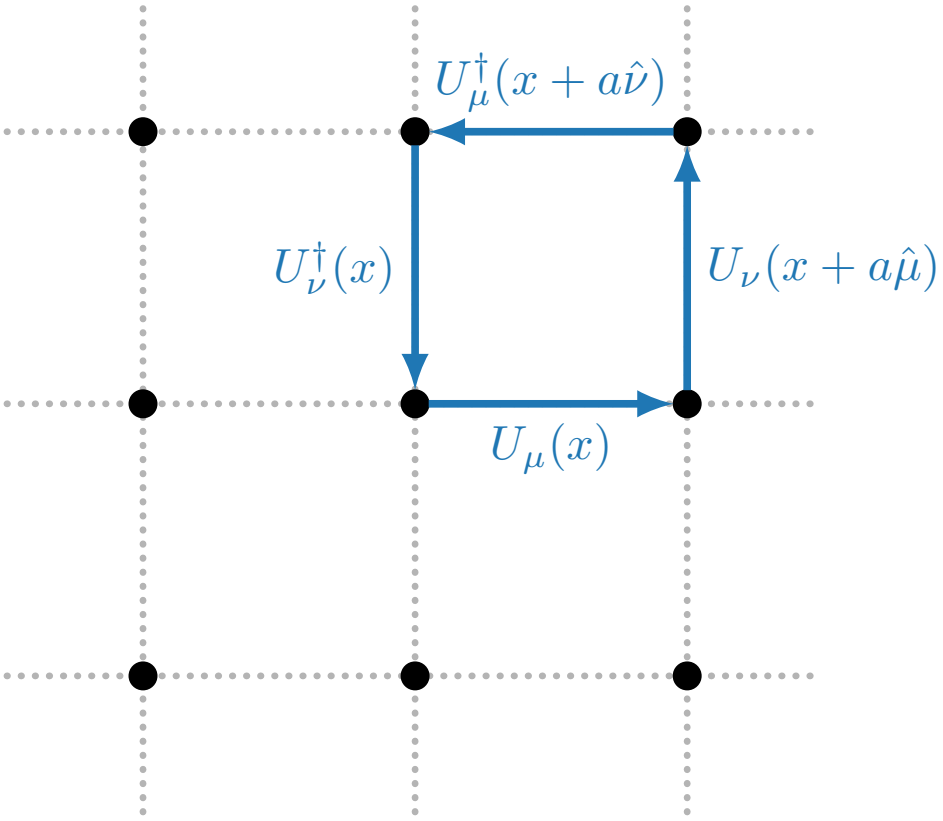

Figure 4.2. The simplest series of link variables forming a closed loop, the 1x1 Plaquette $P_{\mu\nu}(x)$

We can note that the real part of the plaquette contains the gluon action, and by taking the trace we can obtain

$$\begin{aligned}\frac{1}{2}\operatorname{Tr}\left(P_{\mu\nu}(x)+P_{\mu\nu}^{\dagger}(x)\right) &= \operatorname{Tr}\left(\mathbb{I}-\frac{1}{2}g^2a^4G_{\mu\nu}(x)G_{\mu\nu}(x)\right)\\ &= 3-\frac{1}{2}g^2a^4\operatorname{Tr}\left(G_{\mu\nu}(x)G_{\mu\nu}(x)\right)+\mathcal{O}(a^6).\end{aligned} \tag{4.27}$$

Putting this into our gauge action in Eq. 4.23 and discretising, we get the Wilson gauge action [65],

$$\mathcal{S}_G^W[U_\mu]=\beta\sum_x\sum_{\mu>\nu}\left[1-\frac{1}{6}\operatorname{Tr}\left(P_{\mu\nu}(x)+P_{\mu\nu}^{\dagger}(x)\right)\right], \tag{4.28}$$

where β is the inverse lattice coupling $\beta\equiv 6/g^2$. Note that the sum on $\mu>\nu$ avoids double-counting the plaquettes. The Wilson gauge action has errors of $\mathcal{O}(a^2)$, so in practice we use improved gauge actions to suppress these errors by introducing Wilson loops of higher dimensions, such as the 2×1 loop shown in Figure 4.3. By including these extra terms we are able to cancel out higher order a terms. This process is known as Symanzik improvement [70].

One such method of improvement is the Lüscher-Weisz gauge action, which includes terms from the 1×1 plaquette $P_{\mu\nu}^{1\times1}$ (Eq. 4.27), as well as the 2×1 rectangle diagram[1] $R_{\mu\nu}^{2\times1}$, and the $1\times1\times1$ parallelogram $R_{\mu\nu}^{1\times1\times1}$ [71],

$$\mathcal{S}_G^{LW}[U_\mu]=\frac{\beta}{3}\sum_x\sum_{\mu>\nu}\left[c_0\left(1-P_{\mu\nu}^{1\times1}\right)+c_1\left(1-R_{\mu\nu}^{2\times1}\right)+c_2\left(1-R_{\mu\nu}^{1\times1\times1}\right)\right], \tag{4.29}$$

where the coefficients c_i are functions of g^2, chosen to satisfy $c_0+8c_1+8c_2=1$. This ensures discretisation errors are cancelled up to $\mathcal{O}(a^4)$. In this work we use the tree-level improved action, which sets $c_0=20/12$, $c_1=-1/12$, $c_2=0$.

4.1.4. Fermion Action

Next we consider the fermion action. Similarly as for the gluonic action, we want to write the lattice fermion action, $S_{\mathrm{F}}^{\mathrm{Latt}}[U_\mu]$, in a gauge invariant form that goes to the

[1] Note that this includes both the 2×1 and 1×2 rectangle.

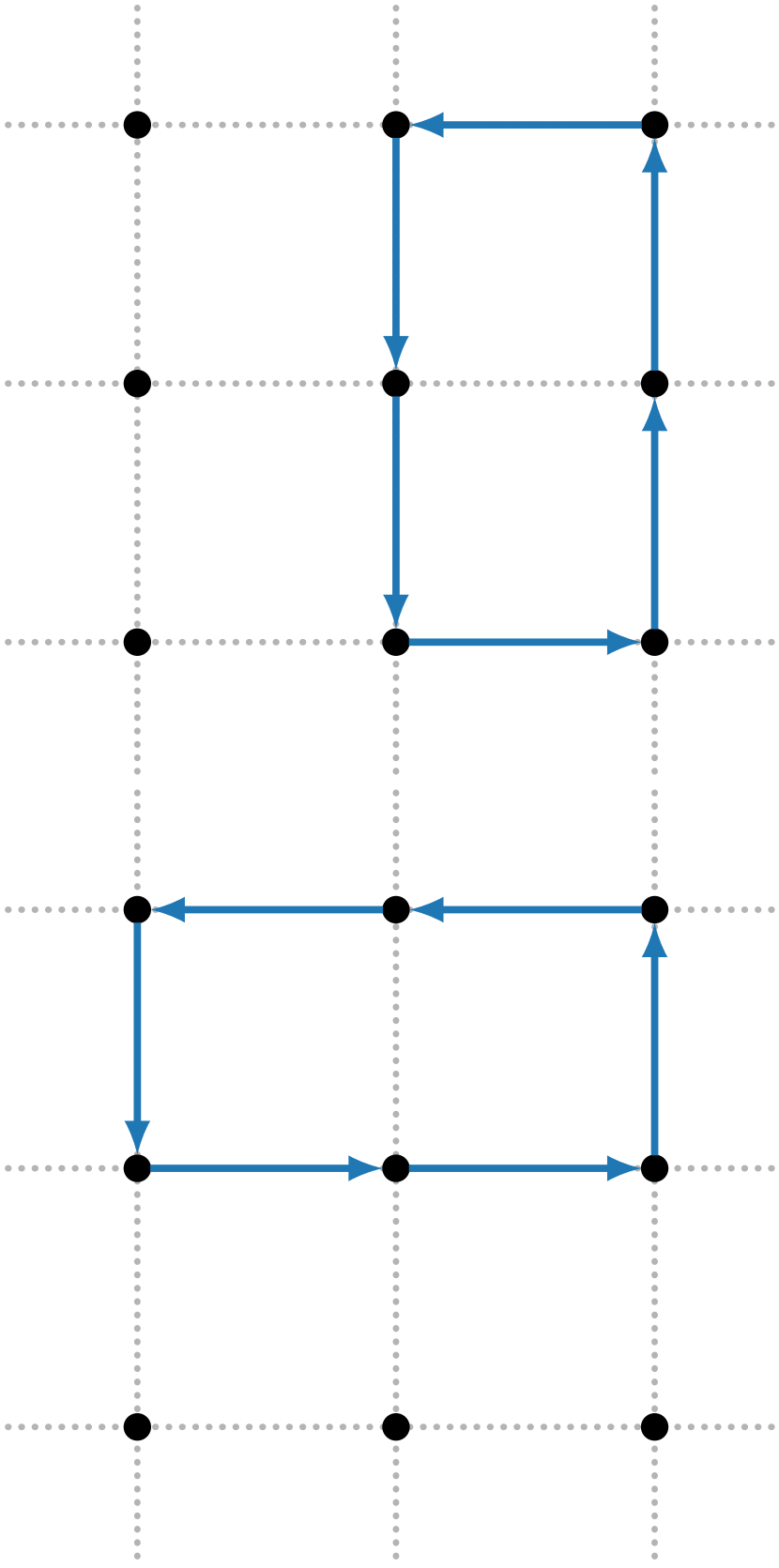

Figure 4.3. The 2×1 and 1×2 rectangle Wilson loops.

Euclidean fermion action

$$\mathcal{S}_{\mathsf{F}}[U_\mu] = \bar{\psi}(x)\left[\not{D}(x) + m\right]\psi(x) \tag{4.30}$$

in the continuum limit $a \to 0$.

Recalling our definition for the covariant finite difference operator Eq. 4.20, the fermion action can be written

$$\begin{aligned}\mathcal{S}_{\mathsf{F}}^{\mathsf{Latt}} &= a^4 \sum_x \bar{\psi}(x)\left[\not{\nabla}(x) + m\right]\psi(x) \\ &= a^4 \sum_x \bar{\psi}(x)\left[ig\not{A} + \not{\partial} + \mathcal{O}(a^2) + m\right]\psi(x).\end{aligned} \tag{4.31}$$

Despite this formalisation allowing us to recover the continuum fermion action in the limit $a \to 0$, it has two issues. First, it introduces $\mathcal{O}(a^2)$ errors to our fermion action. The larger issue is that in the continuum limit we get $2^4 = 16$ fermion species instead of the one physical species. This is known as the fermion doubling problem.

In coordinate space, the finite difference operator Eq. 4.20 couples fermion fields at $x + a\hat{\mu}$ and $x - a\hat{\mu}$, *i.e.* fermion fields separated by two lattice sites. This results in even and odd lattice sites being decoupled along each space-time axis, which gives us the $2^4 = 16$ decoupled fermion fields. This is also seen in momentum space, where the finite difference operator instead takes a sinusoidal form, which results in $2^4 = 16$ poles, of which only the single pole at $(0, 0, 0, 0)$ is physical.

There are a number of methods to remove the fermion doubling problem [72–76]. We will focus on the Wilson fermion action [65].

Wilson Action

The Wilson fermion action removes the nonphysical doublers by adding an irrelevant term into the action (one that vanishes in the continuum limit), which suppresses the non-physical quark species at finite lattice spacing. This Wilson term is defined as Δ such that

$$\bar{\psi}(x)\Delta\psi(x) \equiv \frac{1}{a^2}\sum_\mu \bar{\psi}(x)\left(2\psi(x) - U_\mu(x)\psi(x + a\hat{\mu}) - U_\mu^\dagger(x - a\hat{\mu})\psi\left(x - a\hat{\mu}\right)\right). \tag{4.32}$$

Adding this to the naive fermion action in Eq. 4.31, we arrive at the Wilson action

$$\mathcal{S}_{\mathsf{F}}^{\mathsf{W}}\left[\psi,\bar{\psi},U_{\mu}\right] \equiv a^{4}\sum_{x}\bar{\psi}(x)\left(\nabla\!\!\!/(x)+\frac{ra}{2}\Delta+m\right)\psi(x), \tag{4.33}$$

where r is the Wilson parameter, which is commonly set to $r=1$.

We can write the Wilson fermion action in a compact form as

$$\mathcal{S}_{\mathsf{F}}^{\mathsf{W}}\left[\psi,\bar{\psi},U_{\mu}\right] = a^{4}\sum_{x}\bar{\psi}(x)\mathcal{M}(x,y)\psi(y), \tag{4.34}$$

where $\mathcal{M}$ is the Wilson fermion matrix

$$\frac{\mathcal{M}(x,y)}{C_f} = \delta_{x,y} - \kappa\sum_{\mu}\left[(r-\gamma_{\mu})\,U_{\mu}(x)\delta_{x+a\hat{\mu},y} + (r+\gamma_{\mu})\,U_{\mu}^{\dagger}(x-a\hat{\mu})\delta_{x-a\hat{\mu},y}\right], \tag{4.35}$$

where κ is the hopping parameter, which acts to couple the fermion field at each lattice site to its neighbours. The constant C_f is given by

$$C_f \equiv m_f + \frac{4r}{a} = \frac{1}{2a\kappa_f}, \tag{4.36}$$

$$\kappa_f \equiv \frac{1}{2m_f a + 8r}. \tag{4.37}$$

We can absorb C_f into the definition of the quark fields with $r=1$,

$$\psi(x) \to \frac{\psi(x)}{\sqrt{2a\kappa}}. \tag{4.38}$$

We can define the quark mass in terms of the hopping parameter,

$$m_f = \frac{1}{2}\left(\frac{1}{\kappa_f} - \frac{1}{\kappa_c}\right), \tag{4.39}$$

where κ_c is the critical value of the hopping parameter, where the quark mass vanishes.

While the Wilson action removes the nonphysical fermion doublers, it does so at the cost of increasing discretisation errors from $\mathcal{O}(a^2)$ to $\mathcal{O}(a)$, as well as explicitly breaking chiral symmetry [77].

Clover Action

We can remove the $\mathcal{O}(a)$ errors from the Wilson action by including higher order terms via Symanzik improvement scheme, in particular by including the Sheikholeslami-Wohlert term [78],

$$\mathcal{S}_{\mathsf{F}}^{\mathsf{SW}} = \mathcal{S}_{\mathsf{F}}^{\mathsf{W}} - \sum_{x} \frac{igaC_{SW}\kappa r}{4} \bar{\psi}(x)\sigma_{\mu\nu}G_{\mu\nu}(x)\psi(x), \tag{4.40}$$

where the discretised field strength tensor, $G_{\mu\nu}$, can be related to the plaquette by Eq. 4.25. We can then find an expression for the field strength tensor in terms of the sum of plaquettes around the fermion site, which form a 'clover' diagram, (see Figure 4.4), written as

$$G_{\mu\nu}(x) = \frac{1}{8iga^2}\left(\mathcal{C}_{\mu\nu}(x) - \mathcal{C}_{\mu\nu}^{\dagger}(x) - \frac{1}{3}\,\mathrm{Tr}\left(\mathcal{C}_{\mu\nu}(x) - \mathcal{C}_{\mu\nu}^{\dagger}(x)\right)\right), \tag{4.41}$$

where

$$\begin{aligned}\mathcal{C}_{\mu\nu}(x) = {} & U_{\mu}(x)U_{\nu}(x+a\hat{\mu})U_{\mu}^{\dagger}(x+a\hat{\nu})U_{\nu}^{\dagger}(x) \\ & + U_{\nu}(x)U_{\mu}^{\dagger}(x+a\hat{\nu}-a\hat{\mu})U_{\nu}^{\dagger}(x-a\hat{\nu})U_{\mu}(x-a\hat{\mu}) \\ & + U_{\mu}^{\dagger}(x-a\hat{\mu})U_{\nu}^{\dagger}(x-a\hat{\mu}-a\hat{\nu})U_{\mu}(x-a\hat{\mu}-a\hat{\nu})U_{\nu}(x-a\hat{\nu}) \\ & + U_{\nu}^{\dagger}(x-a\hat{\nu})U_{\mu}(x-a\hat{\nu})U_{\nu}(x+a\hat{\mu}-a\hat{\nu})U_{\mu}^{\dagger}(x).\end{aligned} \tag{4.42}$$

This clover term often leads to the Sheikholeslami-Wohlert fermion action being referred to as the clover action. The coefficient, C_{SW}, can be tuned to fully remove $\mathcal{O}(a)$ errors (see e.g. [78, 79]).

4.1.5. Discretised Path Integral

We follow the method laid out in [80]. Now that we have a discretised form of the QCD Lagrangian written in Euclidean space-time, we can return to the path integral

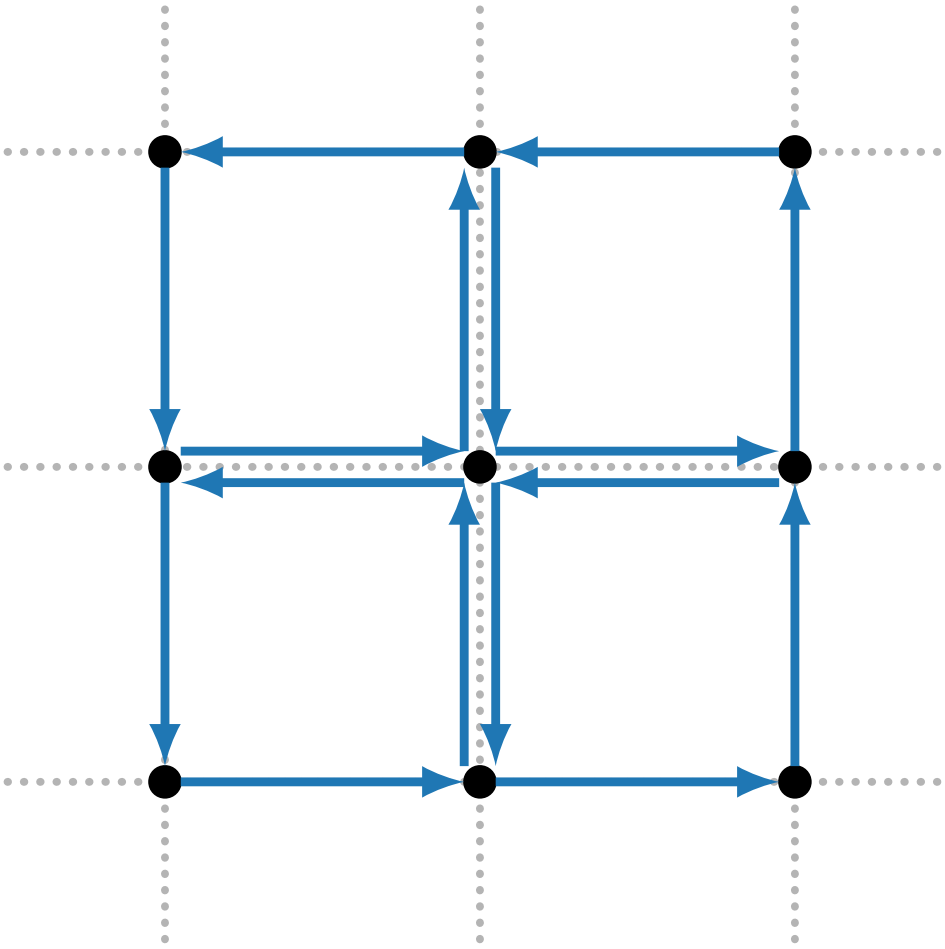

Figure 4.4. The series of link variables to form the clover term $\mathcal{C}_{\mu\nu}(x)$.

expressions we outlined in Section 4.1.1. First considering the partition function

$$\begin{aligned}\mathcal{Z} &= \int \mathcal{D}\psi\,\mathcal{D}\bar{\psi}\,\mathcal{D}U_\mu\,\exp\left(-\mathcal{S}_{\mathsf{QCD}}^{\mathsf{Latt}}[\psi,\bar{\psi},U_\mu]\right)\\ &= \int \mathcal{D}\psi\,\mathcal{D}\bar{\psi}\,\mathcal{D}U_\mu\,\exp\left(-\mathcal{S}_{\mathsf{G}}^{\mathsf{Latt}}[U_\mu]-\mathcal{S}_{\mathsf{F}}^{\mathsf{Latt}}[\psi,\bar{\psi},U_\mu]\right)\\ &= \int \mathcal{D}U_\mu\,\exp\left(-\mathcal{S}_{\mathsf{G}}^{\mathsf{Latt}}[U_\mu]\right)\int \mathcal{D}\psi\,\mathcal{D}\bar{\psi}\,\exp\left(-\mathcal{S}_{\mathsf{F}}^{Latt}[\psi,\bar{\psi},U_\mu]\right).\end{aligned} \tag{4.43}$$

The quark action $\mathcal{S}_{\mathsf{F}}^{\mathsf{Latt.}}$ can be expressed for each flavour of quark in terms of the fermion matrix M, with dimensions $(N_s^3\times N_t\times N_c\times N_D)^2$, where $N_c=3$ is the number of colour charges, and $N_D=4$ is the number of Dirac spin components

$$\mathcal{S}_{\mathsf{F}}^{\mathsf{Latt}}[\psi,\bar{\psi},U_\mu]=\sum_{x,y}\bar{\psi}_\alpha^a(x)M_{\alpha\beta}^{ab}(x,y)\psi_\beta^b(y), \tag{4.44}$$

with spin and Dirac indices restored for clarity, following the convention set in Table 2.1. Multiple quark flavours can be simply summed over.

As the fermion fields $\psi,\bar{\psi}$ act as Grassmann variables, we can write the fermionic integral of the partition function as

$$\int \mathcal{D}\psi\,\mathcal{D}\bar{\psi}\,\exp\left(-\sum_{x,y}\bar{\psi}_\alpha^a(x)M_{\alpha\beta}^{ab}(x,y)\psi_\beta^b(y)\right)=\det(M), \tag{4.45}$$

where we have one $\det(M)$ for each quark flavour, which are multiplied together. For simplicity we will consider a single quark flavour unless otherwise specified. We can then integrate out the fermionic degrees of freedom, and reduce the partition function to

$$\mathcal{Z}=\int \mathcal{D}U_\mu\,\exp\left(-\mathcal{S}_{\mathsf{G}}^{\mathsf{Latt.}}[U_\mu]\right)\det(M[U_\mu]). \tag{4.46}$$

When looking at the vacuum expectation value

$$\langle\Omega|\mathcal{O}[\psi,\bar{\psi},U_\mu]|\Omega\rangle=\frac{1}{\mathcal{Z}}\int \mathcal{D}\psi\,\mathcal{D}\bar{\psi}\,\mathcal{D}U_\mu\,\mathcal{O}[\psi,\bar{\psi},U_\mu]\exp\left(-\mathcal{S}_{\mathsf{QCD}}^{\mathsf{Latt}}[\psi,\bar{\psi},U_\mu]\right), \tag{4.47}$$

we must take care as the operator $\mathcal{O}$ is also dependent on the quark fields. We can still get an expression similar to Eq. 4.45, by noting that the operators of interest typically involve products of an equal number of fermion and anti-fermion fields, such that the

fermionic part of the integral becomes

$$\int \mathcal{D}\psi\,\mathcal{D}\bar{\psi}\,\psi^{a_1}_{\alpha_1}(x_1)...\psi^{a_n}_{\alpha_n}(x_n)\bar{\psi}^{b_1}_{\beta_1}(y_1)...\bar{\psi}^{b_n}_{\beta_n}(y_n) \times \exp\left(-\sum_{x,y}\bar{\psi}^{a}_{\alpha}(x)M^{ab}_{\alpha\beta}(x,y)\psi^{b}_{\beta}(y)\right). \tag{4.48}$$

It is shown in [80] that we can express this in terms of Wick contractions of all possible fermion anti-fermion pairs in the operator. We can then replace each contraction with a quark propagator, $S[U_\mu]$, with the correct colour, Dirac and spatial indices, defined by

$$\sum_{x,a,\alpha} M^{ca}_{\gamma\alpha}(z,x)S^{ab}_{\alpha\beta}(x,y) \equiv \delta^{cb}\delta_{\gamma\beta}\delta_{zy}. \tag{4.49}$$

In the simplest case, where our operator contains a single fermion anti-fermion field pair, the fermionic part of the integral is written

$$\int \mathcal{D}\psi\,\mathcal{D}\bar{\psi}\,\psi^{a_1}_{\alpha_1}(x_1)\bar{\psi}^{b_1}_{\beta_1}(y_1)\exp\left(-\sum_{x,y}\bar{\psi}^{a}_{\alpha}(x)M^{ab}_{\alpha\beta}(x,y)\psi^{b}_{\beta}(y)\right) = \det(M)S^{a_1b_1}_{\alpha_1\beta_1}(x_1,y_1). \tag{4.50}$$

If we extend this to include multiple fermion field pairs in the operator, we replace the single propagator with the set of fully contracted quark propagators.

We then have a form for our vacuum expectation value with the fermionic parts integrated out, in terms of fully contracted quark propagators and the Dirac matrix. We can define our operator in terms of these quark propagators $S[U_\mu]$,

$$\mathcal{O}[U_\mu, S[U_\mu]]. \tag{4.51}$$

It is then sufficient to evaluate the vacuum expectation value across a sub-ensemble of gauge field configurations, U^i_μ, distributed according to the probability

$$P[U^i_\mu] = \det\left(M\left[U^i_\mu\right]\right)\exp\left(-S^{\text{Latt.}}_{\text{G}}\left[U^i_\mu\right]\right), \tag{4.52}$$

and calculate the average value of the operator across each sub-ensemble

$$\langle\Omega|\mathcal{O}[\psi,\bar{\psi},U_\mu]|\Omega\rangle \approx \frac{1}{N}\sum_{i}^{N}\mathcal{O}\left[U_\mu^i, S\left[U_\mu^i\right]\right], \tag{4.53}$$

where $\mathcal{O}\left[U_\mu^i, S\left[U_\mu^i\right]\right]$ is the measurement of the operator on the i^{th} background gauge configuration. These gauge configuration sub-ensembles are typically generated using Hybrid Monte Carlo [81].

4.2. Lattice QCD+QED

We can introduce QED onto the lattice by modifying the gauge action in Eq. 4.22 to include the non-compact U(1) gauge action of the photon,

$$\mathcal{S}_{\text{A}}^{\text{Latt}}[A_\mu^{\text{QED}}] = \frac{1}{2}\beta_{\text{QED}}\sum_{x,\nu<\mu}\left[A_\nu^{\text{QED}}(x) + A_\mu^{\text{QED}}(x+a\hat{\nu}) - A_\nu^{\text{QED}}(x+a\hat{\mu}) - A_\mu^{\text{QED}}(x)\right]^2, \tag{4.54}$$

where β_{QED} is the QED coupling parameter, and modify the fermion action $\mathcal{S}_F[\psi,\psi,U_\mu]$ term to include couplings between the quarks and photons. This is achieved by modifying the Wilson fermion matrix in Eq. 4.35 to include a QED term,

$$\begin{aligned}\frac{\mathcal{M}_q(x,y)}{C_f} = \delta_{x,y} - \kappa_Q\sum_\mu\Big[&(r-\gamma^\mu)\,e^{-ie_qA_\mu^{\text{QED}}}(x)U_\mu(x)\delta_{x+a\hat{\mu},y} \\ &+ (r+\gamma^\mu)\,e^{ie_qA_\mu^{\text{QED}}}(x-a\hat{\mu})U_\mu^\dagger(x-a\hat{\mu})\delta_{x-a\hat{\mu},y}\Big],\end{aligned} \tag{4.55}$$

where e_q is the charge of a quark with flavour q. The complete QCD +QED lattice action can then be written as

$$\mathcal{S}_{\text{QCD+QED}}^{\text{Latt}}[\psi,\bar{\psi},U_\mu,A_\mu^{\text{QED}}] = \mathcal{S}_{\text{G}}^{\text{Latt}}[U_\mu] + \mathcal{S}_{\text{A}}^{\text{Latt}}[A_\mu^{\text{QED}}] + \mathcal{S}_{\text{F}}^{\text{SW}}[\psi,\bar{\psi},U_\mu,A_\mu^{\text{QED}}]. \tag{4.56}$$

The clover coefficient is tuned using pure QCD [79], and we do not include a clover term for the electromagnetic field. One issue that comes from defining charged states on a finite-volume is that the vanishing photon mass implies that the finite-volume effects are not exponentially suppressed with the lattice-volume, as in the pure QCD case. This leads to singularities from photon zero-modes which must be dealt with.

The method used in this work to account for these effects is the QED$_L$ formulation [82], where the zero modes of the photon field are removed on each time slice for the valence quarks. Other methods of formulating QED on the lattice exist, such as the QED$_{TL}$ formulation [83], but these were not explored in this work.

More details about the method used to include QED effects on the lattice as relevant to this work can be found in Refs. [84], [85] and [86].

Chapter 5.

Lattice Methods

In the previous chapter we have shown how to calculate the vacuum expectation value of an operator by considering that operator over a sub-ensemble of gauge field configuration, U_μ^i. In this chapter we will show explicitly how this is calculated in the example case of a meson operator and define the two-point correlation function which allows us to calculate physical quantities using the lattice formalisation defined in the previous chapter.

We will also discuss the various lattice systematics and how we can relate lattice quantities to physical measurements.

5.1. Correlation Functions

In this section we will explore explicitly the example case of the meson two-point correlation function. We start with the meson operator,

$$\chi^{fg}_{\alpha\beta}(x,\Gamma) \equiv \bar{q}^f_\alpha(x)\Gamma^{\alpha\beta}q^g_\beta(x), \tag{5.1}$$

where q^f is the fermion field for a quark of flavour f, and Γ is the spin structure made from γ-matrices to produce the state of interest. We can also write the operator

$$\chi^{\dagger}{}^{fg}_{\alpha\beta}(x,\Gamma) = \bar{q}^g_\alpha(x)\Gamma^{\alpha\beta}q^f_\beta(x), \tag{5.2}$$

where $\chi^\dagger$ and χ are operators which respectively create and annihilate meson states of interest. The gauge-invariant meson correlator can then be constructed on a specific

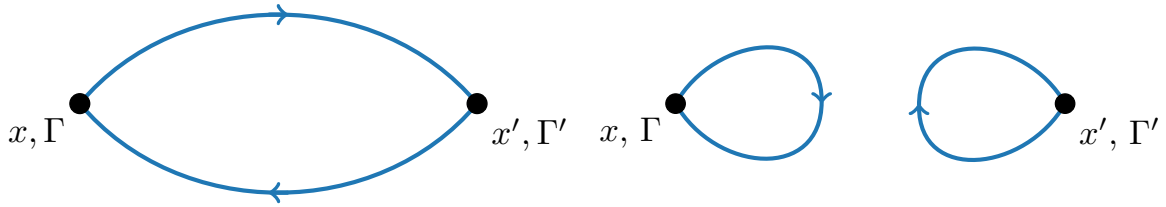

(a) Quark-line connected term.

(b) Quark-line disconnected term.

Figure 5.1. Meson quark flow diagrams for a meson two-point function. Note that the gluon lines are suppressed.

gauge field configuration U^i as

$$\begin{aligned}\langle \chi^{fg}_{\alpha\beta}(x,\Gamma)\chi^{\dagger,f'g'}_{\alpha'\beta'}(x',\Gamma')\rangle_{U^i} &= \langle \bar{q}^{f}_{\alpha}(x)\Gamma^{\alpha\beta}q^{g}_{\beta}(x)\bar{q}^{g'}_{\alpha'}(x')\Gamma^{\alpha'\beta'}q^{f'}_{\beta'}(x')\rangle_{U^i} \\ &= -\left\langle \mathrm{Tr}\left(S^{f'f}_{\beta'\alpha}(x',x)\Gamma^{\alpha\beta}S^{g'g}_{\beta\alpha'}(x,x')\Gamma^{\alpha'\beta'}\right)\delta_{ff'}\delta_{gg'}\right\rangle_{U^i} \\ &\quad + \left\langle \mathrm{Tr}\left(S^{fg}_{\beta\alpha}(x,x)\Gamma^{\alpha\beta}\right)\mathrm{Tr}\left(S^{g'f'}_{\alpha'\beta'}(x',x')\Gamma^{\alpha'\beta'}\right)\delta_{fg}\delta_{f'g'}\right\rangle_{U^i},\end{aligned} \tag{5.3}$$

where colour indices have been suppressed, and we have replaced the Wick contractions over fermion fields with quark propagators. The first term corresponds to the connected quark contribution, shown in Figure 5.1a, and the second term to the disconnected quark contribution shown in Figure 5.1b.

We now have a form for the operator that satisfies Eq. 4.51, *i.e.* only depends on the quark propagators. Now by evaluating this operator across a sub-ensemble of gauge field configurations distributed according to Eq. 4.52 we can write our meson vacuum expectation value according to Eq. 4.53 as

$$\begin{aligned}\langle\Omega|\chi(x,\Gamma)\bar{\chi}(x',\Gamma')|\Omega\rangle \approx \frac{1}{N}\sum_{i}^{N}\Bigg(&-\left\langle \mathrm{Tr}\left(S^{f'f}_{\beta'\alpha}(x',x)\Gamma^{\alpha\beta}S^{g'g}_{\beta\alpha'}(x,x')\Gamma^{\alpha'\beta'}\right)\delta_{ff'}\delta_{gg'}\right\rangle_{U^i} \\ &+\left\langle \mathrm{Tr}\left(S^{fg}_{\beta\alpha}(x,x)\Gamma^{\alpha\beta}\right)\mathrm{Tr}\left(S^{g'f'}_{\alpha'\beta'}(x',x')\Gamma^{\alpha'\beta'}\right)\delta_{fg}\delta_{f'g'}\right\rangle_{U^i}\Bigg).\end{aligned} \tag{5.4}$$

For now we will focus just on the connected term. In Chapter 9 we will revisit the disconnected term, as we explore possible future work.

5.1.1. Two-point Correlation Functions

We can describe how a hadronic system propagates from some source location $(\vec{x'}, t')$ to a sink location $(\vec{x}, t)$ using a two-point correlation function. Diagrammatically, this can be seen in Figure 5.1. We can define the meson two-point function as

$$\mathcal{G}(\vec{p}, \Delta t) = \sum_{\vec{x}, \vec{x'}} e^{-i\vec{p}\cdot(\vec{x}-\vec{x'})} \langle \Omega | \chi(x) \chi^{\dagger}(x') | \Omega \rangle \,, \tag{5.5}$$

where we define $\Delta t = t - t'$, and have Fourier projected into 3-momentum on the sink operator, while the source operator remains in real space [69]. Due to practical limitations in computational power, and the size of a full x' to x correlation function (referred to as all-to-all), we limit the source location x' to a single point, $x' = 0 = (\vec{0}, 0)$, called a point-to-all correlation function.

We can think of our correlation function as the sum of contributions from the tower of all possible energy eigenstates. We can show this by inserting the complete set of states over energy, momentum and spin,

$$\mathbb{I} = \sum_{\alpha, \vec{p'}, s} |\alpha; \vec{p'}; s\rangle \langle \alpha; \vec{p'}; s| \tag{5.6}$$

into the two-point correlation function

$$\mathcal{G}(\vec{p}, t) = \sum_{\alpha, \vec{p'}, s} \sum_{\vec{x}} e^{-i\vec{p}\cdot\vec{x}} \langle \Omega | \chi(x) | \alpha; \vec{p'}; s \rangle \langle \alpha; \vec{p'}; s | \chi(0) | \Omega \rangle \,. \tag{5.7}$$

By invoking translational invariance, we can translate our operator in Euclidean space-time to the origin using

$$\chi(x) = e^{\hat{H}t} e^{-i\vec{P}\cdot\vec{x}} \chi(0) e^{-\hat{H}t} e^{i\vec{P}\cdot\vec{x}}, \tag{5.8}$$

where $\hat{H}$ is the Hamiltonian operator and $\hat{P}$ is the momentum operator, and we have the property

$$\hat{H}\,|\alpha;\vec{p'};s\rangle = E_{\alpha,\vec{p'},s}\,|\alpha;\vec{p'};s\rangle\,, \tag{5.9}$$
$$\hat{P}\,|\alpha;\vec{p'};s\rangle = \vec{p'}\,|\alpha;\vec{p'};s\rangle\,, \tag{5.10}$$
$$\hat{H}\,|\Omega\rangle = 0, \tag{5.11}$$
$$\hat{P}\,|\Omega\rangle = 0. \tag{5.12}$$

Combining the operator translation and the identity

$$\sum_{\vec{x}} e^{i(\vec{p}-\vec{p'})\cdot\vec{x}} = \delta_{\vec{p}\vec{p'}}\,, \tag{5.13}$$

we can write Eq. 5.7 as

$$\begin{aligned}\mathcal{G}(\vec{p},t) &= \sum_{\alpha,\hat{p'},s}\sum_{\vec{x}} e^{-i\vec{p}\cdot\vec{x}}\,\langle\Omega|e^{\hat{H}t}e^{-i\vec{P}\cdot\vec{x}}\chi(0)e^{-\hat{H}t}e^{i\vec{P}\cdot\vec{x}}|\alpha;\vec{p'};s\rangle\,\langle\alpha;\vec{p'};s|\chi(0)|\Omega\rangle \\ &= \sum_{\alpha,\vec{p'},s}\sum_{\vec{x}} e^{i(\vec{p}-\vec{p'})\cdot\vec{x}}e^{-E_\alpha t}\,\langle\Omega|\chi(0)|\alpha;\vec{p'};s\rangle\,\langle\alpha;\vec{p'};s|\chi(0)|\Omega\rangle \\ &= \sum_{\alpha,s} e^{-E_\alpha t}\,\langle\Omega|\chi(0)|\alpha;\vec{p};s\rangle\,\langle\alpha;\vec{p};s|\chi(0)|\Omega\rangle\,. \end{aligned} \tag{5.14}$$

Hence we have shown that the two-point correlation function can be represented as a sum exponentially weighted contributions from all possible energy eigenstates. This definition will be useful later when working with correlation functions in Chapter 7.

5.2. Lattice Systematics

In order to represent QCD on a finite lattice, we have introduced parameters defining the lattice spacing and volume (Eq. 4.12), as well as defining the quark mass in terms in the tunable hopping parameter (Eq. 4.39), and quark charge in terms of the QED coupling, β_{QED}. We are also free to include only some flavours of quark in our calculation. In this work (as in many) we have restricted ourselves to the up, down and strange quarks. At the energy scales we are interested in the large majority of the contribution will come from these three quark flavours. However, in order to relate lattice results back to experiment, we must quantify these systematics.

5.2.1. Quark Mass

As mentioned in Section 4.1.4, we are free to tune the mass of our quarks using the hopping parameter κ_f. If let every quark in the simulation have its physical quark mass, we call this simulating at the *physical point*. We find that the computational expense associated with resolving the action increases with decreasing quark mass, and for quark masses at the physical point where the up and down quarks have very small mass, this becomes very large. Due to this reason, the generation of gauge field configurations at the physical point is very expensive, and it is common to perform lattice calculations with nonphysical quark masses, and then extrapolate to the physical point. As algorithms improve and super computing resources increase, it is becoming more common to perform calculations with physical or near physical quark mass, in what are called "gold-plated" calculations, as in [87, 88].

There are several schemes to choose the nonphysical quark masses and path taken to the physical point. One common option is to start with all quarks fixed to some heavy quark mass, such that the up, down and strange quark all have the physical strange quark mass, and then vary the up and down quark mass towards the physical point.

The method used in this work, however, is to start with defining the SU(3) flavour-symmetric point, where all three quarks have the same mass, and vary each quark mass towards the physical point, while keeping the flavour singlet quark mass fixed to the physical value, such that

$$\bar{m} \equiv \frac{1}{3}(m_u + m_d + m_s) = \text{constant}. \tag{5.15}$$

In practice this is achieved by defining the symmetric point in terms of the connected-only neutral pseudoscalar meson masses,

$$M^2(u\bar{u}) = M^2(d\bar{d}) = M^2(s\bar{s}) = M^2(n\bar{n}) = X_\pi^2, \tag{5.16}$$

where X_π^2 is the average pseudoscalar mass, defined by

$$X_\pi^2 = \frac{1}{3}\left(2M_k^2 + M_\pi^2\right), \tag{5.17}$$

where M_k^2 and M_π^2 are the real-world physical masses. This is done in the Dashen scheme (discussed in Section 5.2.6) using experimental measurements of the π^+, K^+ and K^-.

This has some key advantages [85, 89]. Firstly, this scheme allows us much more control over the flavour breaking effects as we move away from the SU(3) flavour-symmetric point. Secondly, by keeping the singlet mass fixed, we have a simpler expansion in the flavour breaking expansions, as well as flavour-symmetry effects being constant at leading order. The flavour-breaking expansion will be discussed in more detail in Section 5.2.5.

5.2.2. Lattice Spacing and Scale setting

In lattice calculations, we calculate all dimensionful quantities with respect to the lattice spacing, a. This parameter is determined indirectly, by setting the bare QCD coupling, β_{QCD}, and the quark mass. The scale is determined by matching to physical values, detailed in [90]. In these simulations, the scale was set by extrapolating a series of SU(3) flavour singlet quantities, for fixed β_{QCD} and varying κ, along trajectories to the physical point [86, 89, 91]. Once determined, the lattice spacing is fixed for all configurations with fixed β_{QCD}. The effects of using a discrete lattice spacing on the fermion and gauge actions have been discussed above in Section 4.1.4 and Section 4.1.3, as well as some methods to reduce the discretisation errors. For a full continuum extrapolation, multiple values for a, and hence β_{QCD} are required. Changing the lattice spacing also changes the volume, however, so smaller lattice spacings result in a smaller lattice volume, which introduces finite -volume errors, which in turn require an increase of the number of lattice sites, which introduces additional computational complexity. In this work, the ensembles used have all been generated with a fixed inverse coupling, and hence fixed lattice spacing.

The gauge field sub-ensembles used in this work were generated by the QCDSF collaboration. We use two volumes for the majority of this work, three ensembles with a volume of $32^3 \times 64$, and three with a volume of $48^3 \times 96$. In addition in Chapter 9 we used a smaller, $24^3 \times 48$ lattice in order to do some exploratory studies into the QED corrections to the disconnected contributions to the anomalous magnetic moment of the muon.

These gauge field sub-ensembles, listed in Table 5.1, all include physical sea quark charges of $e_u = +\frac{2}{3}, e_d = e_s = -\frac{1}{3}$, in units of the electron charge. The strong coupling was chosen to be $\beta_{\text{QCD}} = 5.50$, which leads to a lattice spacing of $a = 0.068(1)$fm [84].

	β_{QCD}	e^2	Lattice Volume	κ_u	κ_d	κ_s
A*	5.5	1.25	$32^3 \times 64$	0.124362	0.121713	0.121713
B				0.124440	0.121676	0.121676
C				0.124508	0.121821	0.121466
D*			$48^3 \times 96$	0.124362	0.121713	0.121713
E				0.124440	0.121676	0.121676
F				0.124508	0.121821	0.121466
G*			$24^3 \times 48$	0.124362	0.121713	0.121713

Table 5.1. Details of the lattice simulation parameters used in this work. Ensembles denoted with * indicate the SU(3) flavour-symmetric point.

We expect that any QED corrections to the hadronic contribution of the anomalous magnetic moment of the muon to be very small, and therefore hard to calculate on the lattice. In order to compensate for this we use an exaggerated QED coupling. The simulations use $\beta_{\text{QED}} = 0.8$, which corresponds to $e^2 = 1.25, \alpha_{\text{EM}} = e^2/(4\pi) \approx 0.1$, approximately 10 times the physical coupling. It has been observed in this region any QED terms scale linearly in e^2 [84]. We also see this effect later in this work for the vector current renormalisation Figure 6.4. In this work we will assume that any non-linear terms are negligible, but further study using ensembles with different values of β_{QED} will be able to confirm this.

Further details about these gauge field sub-ensembles can be found in Refs. [84], [86] and [92].

5.2.3. Finite-Volume

In restricting the lattice to a finite-volume, we have to address the boundaries of this volume. We do this by introducing periodic boundary conditions in space, and anti-periodic boundary conditions in time. This will introduce errors from 'wrap-around' effects, which can be thought of as adjacent copies of the lattice volume in each spatial direction, and 'backwards propagating states' in time [93]. In order to investigate the presence of any potential finite-volume effect in our results, we have used multiple lattice volumes, outlined in Table 5.1.

Details on how we can attempt to correct for finite-volume effects are shown in Section 7.2.3.

5.2.4. Lattice Units

In lattice calculations, we replace the physical variables with their dimensionless counterparts, written in terms of the lattice spacing, which we refer to as 'lattice units'.

$$m_{\text{lat}} = a m_{\text{phys}} \tag{5.18}$$

$$x_{\text{lat}} = a^{-1} x_{\text{phys}}. \tag{5.19}$$

The physical units can be recovered by multiplying or dividing by the appropriate power of the lattice spacing and $\hbar c \approx 0.1973\,\text{GeV fm}$. For example, the physical mass can be recovered by $\frac{\hbar c}{a} m_{\text{lat}}$ in units of energy. Throughout this thesis, variables (apart from the lattice spacing itself) are assumed to be written in lattice units, unless otherwise specified.

We also often refer to momentum in terms of *momentum units*, which are an integer count of the discretised momentum in each space-time direction. For example, we might refer to a momentum as $p = (1, 0, 0, 1)$ which indicates 1 unit of momentum in the temporal direction, and 1 unit in the z-spatial direction. Physical units can be restored via

$$Q_\mu = \frac{2\pi}{L_\mu} p_\mu, \tag{5.20}$$

where L_μ is the lattice extent in the μ direction.

5.2.5. Flavour Breaking Expansion

We follow the flavour-breaking program outlined in [89, 94], initially for QCD, and extended to include electromagnetic (EM) interactions in [84, 86]. As mentioned above, we start at the SU(3) flavour-symmetric point, where $m_u = m_d = m_s$, and the average quark mass is kept constant at the physical value, $\bar{m} \equiv \frac{1}{3}(m_u + m_d + m_s)$. We are then able to adjust all quark masses towards the physical quark masses by varying

$\delta m_q \equiv m_q - \bar{m}$. This leads to highly constrained polynomials in δm_q and e_q^2 for quark flavour q, and reduces the number of free parameters drastically.

The full meson mass expansion including both QCD and QED terms is presented in [86], however as we are only interested in neutral mesons in this work, we can simplify this considerably. For neutral mesons of flavour $q\bar{q}$, the meson mass expansion is

$$\begin{aligned} M^2(q\bar{q}) =& M_0^2 + 2\alpha\delta\mu_q + \frac{1}{6}\beta_0(\delta m_u^2 + \delta m_d^2 + \delta m_s^2) + 2\beta_1\delta\mu_q^2 + 2\beta_1^{\mathsf{EM}} e_q^2 \\ &+ \gamma_0^{\mathsf{EM}}(e_u^2\delta m_u + e_d^2\delta m_d + e_s^2\delta m_s) + 2\gamma_1^{\mathsf{EM}} e_q^2\delta\mu_q \\ &+ 2\gamma_5^{\mathsf{EM}} e_q(e_u^2\delta m_u + e_d^2\delta m_d + e_s^2\delta m_s), \end{aligned} \tag{5.21}$$

where M_0^2 represents the mass in the SU(3) limit with all quark charges turned off. We have differentiated between the sea and valence quark masses as m_q and μ_q respectively, and we define $\delta\mu_q = \mu_q - \bar{m}$ as the distance of the valence quark mass from the SU(3) flavour-symmetric point, and with δm_q similarly defined.

In order to better constrain the coefficients of the flavour breaking-expansion above we employ a range of partially-quenched valance quarks, corresponding to the neutral pseudoscalar meson mass in range $230\,\text{MeV} \lesssim m_{\bar{q}q} \lesssim 790\,\text{MeV}$. The full list of values used is listed in Table C.1.

5.2.6. Dashen Scheme

The introduction of the quark charges complicates the definition of the SU(3) symmetric point due to EM renormalisation of the quark masses. In order to deal with this, we follow the renormalisation method outlined in [86], and use the Dashen scheme, which absorbs all EM effects in the neutral, purely connected pseudoscalar mesons, $m_\pi^{q\bar{q}}$, into the definition of the quark mass. We call this the "Dashen mass" δm_q^D. As a consequence of this, the distance from the SU(3) symmetric point to the chiral limit is now independent of the quark charge. In this scheme, we define the SU(3) symmetric point as where $m_\pi^{u\bar{u}} = m_\pi^{d\bar{d}} = m_\pi^{s\bar{s}}$. By adopting the Dashen scheme, we can drastically simplify the flavour-breaking expansion for neutral pseudoscalar mesons listed above by replacing the bare quark masses $\delta\mu_q$ with the Dashen equivalents $\delta\mu_q^D$.

In the Dashen scheme, the coefficient β_1^{EM} in the flavour-breaking expansion for neutral pseudoscalar mesons is zero [84] and the expansion can be rewritten as

$$M^2(q\bar{q}) = M_0^2 + 2\alpha\delta\mu_q^D + \frac{1}{6}\beta_0(\delta m_u^2 + \delta m_d^2 + \delta m_s^2) + 2\beta_1(\delta\mu_q^D)^2, \tag{5.22}$$

where the Dashen mass $\delta\mu_q^D$ is defined by

$$\delta\mu_q^D = \delta\mu_q + \Bigg[\frac{1}{2}\gamma_0^{EM}(e_u^2\delta m_u + e_d^2\delta m_d + e_s^2\delta m_s) + \gamma_1^{EM}e_q^2\delta\mu_q + \gamma_5^{EM}e_q(e_u\delta m_u + e_d\delta m_d + e_s\delta m_s)\Bigg]/\alpha. \tag{5.23}$$

The SU(3) symmetric point then corresponds to a Dashen mass of zero, $\delta\mu_q^D = 0$, while the physical up and down quark masses occur at a negative Dashen mass, and the strange quark mass is positive in Dashen mass.

Chapter 6.

Vector Current Renormalisation

6.1. Vector Current

As mentioned in Section 3.2.3, the leading order hadronic contribution, $a_\mu^{\text{HVP,LO}}$, can be calculated from the cross section of a virtual photon decaying into hadrons. This can be related to the vacuum polarisation, which is useful as we are able to compute this on the lattice. The vacuum polarisation tensor, $\Pi_{\mu\nu}(Q)$, is defined as

$$\Pi_{\mu\nu}(Q) = \int d^4x\, e^{iQ\cdot x} \left\langle J_\mu(x) J_\nu(0) \right\rangle , \tag{6.1}$$

where $J_\mu(x) = \frac{2}{3}\bar{u}\gamma_\mu u - \frac{1}{3}\bar{d}\gamma_\mu d - \frac{1}{3}\bar{s}\gamma_\mu s + \ldots$ is the electromagnetic current operator.

In order to compute this on the lattice we use the local vector current for each flavour of quark,

$$V_{\mu,f}^{local}(x) = \bar{\psi}_f(x)\gamma_\mu\psi_f(x). \tag{6.2}$$

In the Wilson lattice formulation, this vector current is not conserved, due to the explicit breaking of chiral symmetry in the Wilson action. We attempt to overcome this be using the point-split vector current

$$V_{\mu,f}^{PS}(x) = \frac{1}{2}\left(\bar{\psi}_f(x+a\hat{\mu})(1+\gamma_\mu)U_\mu^\dagger(x)\psi_f(x) - \bar{\psi}_f(x)(1-\gamma_\mu)U_\mu(x)\psi_f(x+a\hat{\mu})\right) \tag{6.3}$$

which is conserved, even at finite lattice spacing. If we replace the EM current operator in Eq. 6.1 with the conserved vector current, we find the correlator $\langle V_\mu^{PS}(x) V_\nu^{PS}(0)\rangle$ can

be expanded (only showing the connected terms), as in Section 5.1, to

$$\begin{aligned}\langle V^{PS}_{\mu,f}(x)V^{PS}_{\nu,g}(0)\rangle =&\frac{1}{4}\Big\{\overbrace{\bar\psi_f(x+a\hat\mu)(1+\gamma_\mu)U^\dagger_\mu(x)\psi_f(x)\bar\psi_g(a\hat\nu)(1+\gamma_\nu)U^\dagger_\nu(0)\psi_g(0)}\\ &-\overbrace{\bar\psi_f(x)(1-\gamma_\mu)U^\dagger_\mu(x)\psi_f(x+a\hat\mu)\bar\psi_g(a\hat\nu)(1+\gamma_\nu)U^\dagger_\nu(0)\psi_g(0)}\\ &-\overbrace{\bar\psi_f(x+a\hat\mu)(1+\gamma_\mu)U^\dagger_\mu(x)\psi_f(x)\bar\psi_g(0)(1-\gamma_\nu)U^\dagger_\nu(0)\psi_g(a\hat\mu)}\\ &+\overbrace{\bar\psi_f(x)(1-\gamma_\mu)U^\dagger_\mu(x)\psi_f(x+a\hat\mu)\bar\psi_g(0)(1-\gamma_\nu)U^\dagger_\nu(0)\psi_g(a\hat\mu)}\Big\} \quad (6.4)\\ =&\frac{1}{4}\,\mathrm{Tr}\Big\{(1+\gamma_\mu)U^\dagger_\nu(0)\gamma_5 S^\dagger(x+a\hat\mu,0)\gamma_5(1+\gamma_\nu)U^\dagger_\nu(0)S(x,a\hat\nu)\\ &-(1+\gamma_\mu)U^\dagger_\nu(0)\gamma_5 S^\dagger(x,0)\gamma_5(1-\gamma_\nu)U_\mu(x)S(x+a\hat\mu,a\hat\nu)\\ &-(1-\gamma_\nu)U_\nu(0)\gamma_5 S^\dagger(x+a\hat\mu,a\hat\nu)\gamma_5(1+\gamma_\mu)U^\dagger_\mu(x)S(x,0)\\ &+(1-\gamma_\nu)U_\nu(0)\gamma_5 S^\dagger(x,a\hat\nu)\gamma_5(1-\gamma_\mu)U_\mu(x)S(x+a\hat\mu,0)\Big\}. \quad (6.5)\end{aligned}$$

Here we can see that we must compute five point-to-all propagators; One which starts from the origin $S(x,0)$ as usual, and four corresponding to $S(x,a\hat\nu)$, which have each been shifted by one lattice spacing in a different direction.

In order to keep the computational cost under control, in this work we only use the conserved vector current at the sink, and use the local vector current, Eq. 6.2, at the source, allowing the correlator to be computed from a single point-to-all propagator, reducing the cost by a factor of five. This mixed point-split/local correlator is written

$$\langle V^{PS}_{\mu,f}(x)V^{local}_{\nu,f}(0)\rangle\,. \quad (6.6)$$

The inclusion of the local vector current requires the inclusion of a renormalisation procedure which is consistent with $\mathcal{O}(a)$ improvements,

$$V^R_{\mu,f} = Z_V^{m_f,e_f}V^{local}_{\mu,f}\left(1+c_\nu\frac{\partial_\nu T_{\mu\nu,f}}{V_{\mu,f}}\right), \quad (6.7)$$

where $Z_V^{m_f,e_f}$ is the mass- and charge-dependent vector current renormalisation factor for quark flavour f (for simplicity, we will refer to this as Z_V^f from now on). The improvement coefficient c_ν is currently unknown for our gauge feld configurations, and as such we are unable to completely remove $\mathcal{O}(a)$ artefacts from our simulation. This will be discussed in more depth towards the end of this chapter in Section 6.4.

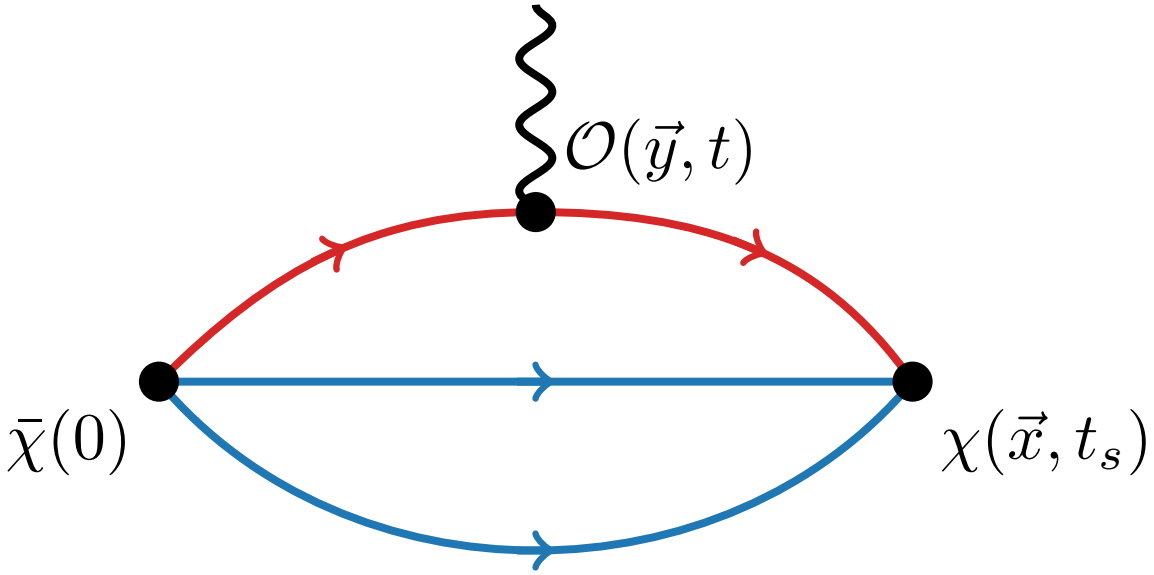

Figure 6.1. Three point correlation function, with the operator inserted on the singly represented quark at $(\vec{y},t)$.

The procedure employed here for computing Z_V^f is to enforce charge conservation in the calculation of the nucleons EM form factor, $F_1(Q^2=0)$. However, before discussing the results, we must first discuss nucleon three-point correlation functions.

6.2. Three-point Correlation Functions

To calculate the vector current renormalisation factor, we must first define an additional type of correlator, called a three-point correlator. This three-point correlator is analogous to the previously discussed two-point correlator, with the addition of a current insertion operator, $\mathcal{O}$. In the three-point function, the inserted operator $\mathcal{O}$ interacts with one of the quark lines at some point $(\vec{y},t)$ between the annihilation operator at the sink $(\vec{x},t_s)$, and the creation operator at the source $(\vec{0},0)$, shown in Figure 6.1.

The three-point correlation function can then be written as

$$C^f_{3pt}(\vec{p}\,',t_s,\vec{q},t,\mathcal{O}) \equiv \sum_{\vec{x},\vec{y}} e^{-i\vec{p}\,'\cdot\vec{x}} e^{+i\vec{q}\cdot\vec{y}} \langle\Omega|\chi^f_N(\vec{x},t_s)\mathcal{O}(\vec{y},t)\bar{\chi}^f_N(\vec{0},0)|\Omega\rangle\,, \tag{6.8}$$

Note that in Eq. 6.8 there are two independent momenta; $\vec{q}$ which corresponds to the momentum at $(\vec{y},t)$, the current insertion point, and $\vec{p}\,'$ which corresponds to the sink

momentum, at $(\vec{x}, t_s)$. The source momentum can then be inferred though momentum conservation as $p^\mu = p'^\mu - q^\mu$.

Following the method laid out for the two-point correlation function in Section 5.1.1, we can use translational invariance, and insert two complete sets of states, $N_1 = |\alpha, \vec{k}, s_1\rangle$ and $N_2 = |\beta, \vec{k}\,', s_2\rangle$, to transform Eq. 6.8 into

$$\begin{aligned} C_{3pt}(\vec{p}\,', t_s, \vec{q}, t, \mathcal{O}) &= \sum_{\vec{x},\vec{y}} e^{-i\vec{p}\,'\cdot\vec{x}} e^{+i\vec{q}\cdot\vec{y}} \langle\Omega|\chi(\vec{x}, t_s)\mathcal{O}(\vec{y}, t)\bar{\chi}(\vec{0}, 0)|\Omega\rangle\,, \\ &= \sum_{N_1,N_2} \sum_{\vec{x},\vec{y}} e^{-i\vec{p}\,'\cdot\vec{x}} e^{i\vec{q}\cdot\vec{y}} \langle\Omega|\chi(\vec{x}, t_s)|N_1\rangle \langle N_1|\mathcal{O}(\vec{y}, t)|N_2\rangle \langle N_2|\bar{\chi}(\vec{0}, 0)|\Omega\rangle\,, \\ &= \sum_{\alpha,s_1,\beta,s_2} e^{-E_\alpha(t_s-t)} e^{-E_\beta t} \langle\Omega|\chi(0)|\alpha, \vec{p}\,', s_1\rangle \langle\alpha, \vec{p}\,', s_1|\mathcal{O}(0)|\beta, \vec{p}, s_2\rangle \\ &\qquad \times \langle\beta, \vec{p}, s_2|\bar{\chi}(0)|\Omega\rangle\,. \end{aligned} \tag{6.9}$$

In order to calculate the three-point function, there are two common methods used [95, 96]; Sequential source through the sink, and through the operator. In this work we use the sequential source through the sink method. For this work, it is enough to know that this sequential source method allows us free choice of the current insertion operator, $\mathcal{O}$, the insertion time, t, and the current (or source) momentum, $\vec{q}$ (or $\vec{p}$), for each sequential propagator, which will allow us simplify the extraction of the matrix element $\langle N_1|\mathcal{O}(q)|N_2\rangle$.

We can extract the matrix element by taking specific combinations of the ratio between two- and three-point functions.

$$R(\vec{p}\,', t_s, \vec{p}, t, \mathcal{O}) = \frac{C_{3pt}(\vec{p}\,', t_s, \vec{q}, t, \mathcal{O})}{C_{2pt}(\vec{p}, t_s)} \sqrt{\frac{C_{2pt}(\vec{p}\,', t) C_{2pt}(\vec{p}\,', t_s) C_{2pt}(\vec{p},\ t_s - t)}{C_{2pt}(\vec{p},\ t) C_{2pt}(\vec{p},\ t_s) C_{2pt}(\vec{p}\,', t_s - t)}}. \tag{6.10}$$

So long as we consider a sufficiently large time such that the ground state dominates the signal, this ratio cancels off the exponential factors, as well as the momentum dependent overlap factors [97].

In this work, we will only study the specific case of zero momentum insertion, $\vec{q} = 0 \Rightarrow \vec{p}\,' = \vec{p}$, along with our sink time t_s fixed, which allows us to simplify the ratio to

$$R(\vec{p}, t_s, \vec{p}, t, \mathcal{O}) = \frac{C_{3pt}(\vec{p}, t_s, \vec{0}, t, \mathcal{O})}{C_{2pt}(\vec{p}, t_s)}. \tag{6.11}$$

We can now look at how we can use this matrix element to calculate the required renormalisation factor for the local vector current.

6.3. Vector Current Renormalisation factor

As discussed earlier in this chapter, we use a local vector current at the source in our lattice calculation, which requires the renormalisation given in Eq. 6.7, as it is not conserved. In addition to the regular mass-dependence of Z_V^f, the vector current renormalisation factor of the local vector current also has a dependence on the quark charge, as first noted in [98].

The renormalisation factor Z_V^f can be determined by computing matrix elements of the electromagnetic current J_μ [97],

$$\langle \mathcal{B}(p',s')|J_\mu(q)|\bar{\mathcal{B}}(p,s)\rangle = \bar{\psi}(p',s')\left[\gamma_\mu F_1(Q^2) + \frac{i\sigma_{\mu\nu}q^\nu}{2m_{\mathcal{B}}}F_2(Q^2)\right]\psi(p,s), \tag{6.12}$$

where F_1 and F_2 are the Dirac and Pauli form factors, $\psi(p,s)$ is a Dirac spinor with momentum p and spin s, q is the momentum transfer, $Q^2 = -q^2$, and $m_{\mathcal{B}}$ is the mass of the baryon state $\mathcal{B}$, to which the operator is coupled to.

The Dirac and Pauli form factors can be written in a linear combination to form the Sachs electric and magnetic form factors for each nucleon, respectively given as

$$G_E(Q^2) = F_1(Q^2) - \frac{Q^2}{4M^2}F_2(Q^2), \tag{6.13}$$

$$G_M(Q^2) = F_1(Q^2) + F_2(Q^2), \tag{6.14}$$

which link directly to measurable quantities in experiments [99, 100].

In the case of zero momentum transfer, the electric form factor simply becomes

$$G_E(0) = F_1(0), \tag{6.15}$$

which is equal to the baryon charge [101], $G_E^{proton}(0) = 1,\ G_E^{neutron}(0) = 0$.

By restricting ourselves to zero-momentum, $p = p' = 0$, we find that the spatial components of the vector current vanish, and the temporal component gives us the

electric form factor at $Q^2 = 0$, *i.e.* the ratio of three- and two-point correlation function as in Eq. 6.11 simplifies to

$$R(0, t_s, 0, t, J_\mu) = \frac{C_{3pt}(0, t_s, 0, t, J_\mu)}{C_{2pt}(0, t_s)} = F_1(0). \tag{6.16}$$

If we restrict the current operator to act on a single quark flavour, f, with unit charge, as we do in lattice calculations, then $F_1(0)$ acts as a count of the number of quarks with flavour f in the baryon in question. In the case of the down quark in the proton, we expect $F_1^d(0) = 1$. Any deviation from this is due to the current not being conserved, which leads us to the multiplicative renormalisation factor Z_V^f being required to correct this.

We determine Z_V^f by computing the singly-represented (or "down") quark contribution to the nucleon's Dirac electromagnetic form factor at zero-momentum transfer, where the mass and charge of the singly-represented "down" quark in the nucleon is varied over the full range of quark masses and charges considered in this work (See Table C.1). The spectator, doubly-represented (or "up") quarks are set to be electrically neutral.

To achieve this, we calculate the nucleon three-point function at zero momentum

$$C_{3pt}^f(t_s, t) = \langle \chi_N^f(\vec{x}, t_s) V_{4,f}(\vec{y}, t) \bar{\chi}_N^f(\vec{0}, 0) \rangle \,, \tag{6.17}$$

where $V_{4,f}$ is the time-component of the local vector current given in Eq. 6.2 for quark flavour f, and χ_N^f is the standard nucleon interpolating operator, here constructed from two electrically neutral quarks (n) and a single quark of flavour f with mass m_f and charge e_f,

$$\chi_N^f(x) = \epsilon^{abc} \left(\psi_n^a(x) C \gamma_5 \psi_f^b(x) \right) \psi_n^c(x). \tag{6.18}$$

The local vector current renormalisation, Z_V^f, can then be determined from the ratio

$$\frac{1}{Z_V^f} = R^f(t) = \frac{C_{3pt}^f(t_s, t)}{C_{2pt}^f(t_s)}, \tag{6.19}$$

where $C^f_{2pt}(t)$ is the nucleon two-point function with flavour content matching that of the three-point function in Eq. 6.17,

$$C^f_{2pt}(t) = \sum_{\vec{x}} \langle \chi^f_N(\vec{x}, t) \bar{\chi}^f_N(\vec{0}, 0) \rangle \,. \tag{6.20}$$

6.3.1. Results

In this work, the source-sink separation for the three-point function is chosen to be $t_s = 14$, with the current insertion time, t, allowed to vary between the source and sink times. While there might be some concern of excited state contribution to nucleon matrix elements if insufficient source-sink separation is chosen, this is not an issue for the time component of the electromagnetic current at zero momentum transfer, due to charge conservation.

Figure 6.2 shows an example of $R^f(t)$ in Eq. 6.19, using the Dashen tuned symmetric point up quark. Fitting over the indicated time window gives a value of $Z_V = 0.8260(22)$. Also shown in Figure 6.2 is a check for the point-split vector current, $V^{PS}_{4,f}$, which clearly shows $Z_V = 1$, indicating that this current is correctly conserved.

This ratio is computed over each simulated quark mass/charge combination in Table C.1. The calculated Z^f_V values are shown in Figure 6.3 as a function of the neutral pseudoscalar meson mass squared, $m^2_{q\bar{q}}$. The complete list of values for Z^f_V calculated for each quark mass/charge combination are also shown in Table C.1.

As can be clearly seen, there is both a clear mass- and charge-dependence present in the vector current renormalisation factor.

In order to better understand the charge-dependence of Z^f_V, we require results of Z^f_V for multiple quark charges at a fixed quark mass. In order to achieve this, we extrapolated the results of each quark charge in Figure 6.3 linearly in $m^2_{q\bar{q}}$ to the chiral limit. The fit parameters of this extrapolation is shown in Table 6.1, using a linear fit of the form $Z^f_V = a\, m^2_\pi + b$.

These extrapolated values can then be plotted as a function of the quark charge squared, e^2_f, shown in Figure 6.4. We observe a linear e^2_f dependence over the range of charges considered, and can note that for the $e^2_f = 0$ case, our result agrees with those found in pure QCD studies [102].

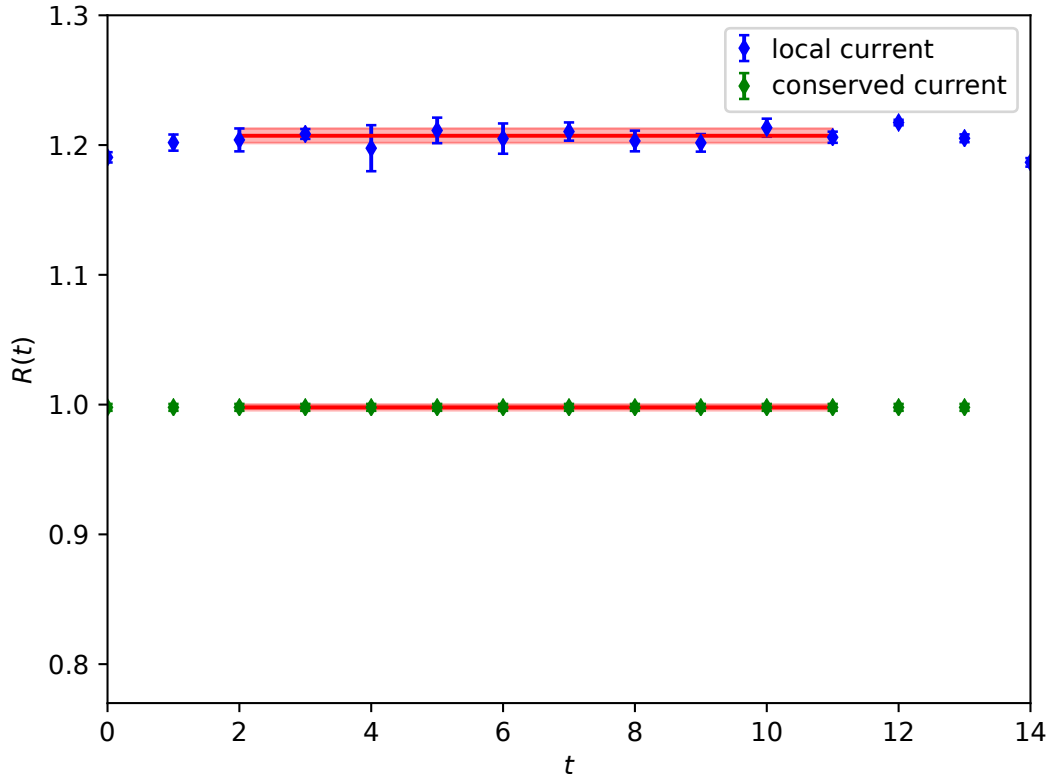

Figure 6.2. Example of the ratio in Eq. 6.19 at the SU(3) symmetric point. When using the point-split current we correctly resolve a value of 1, indicating the charge is conserved. In the case of the local current, we can calculate the required value of Z_v^f in order to restore charge conservation.

Quark	a	b
Up	0.056(4)	0.815(2)
Down	0.054(4)	0.851(2)
Neutral	0.056(3)	0.863(1)

Table 6.1. Fit parameters for the extrapolation of Z_V^f for each quark flavour. The fit is of the form $Z_V^f = a\, m_\pi^2 + b$.

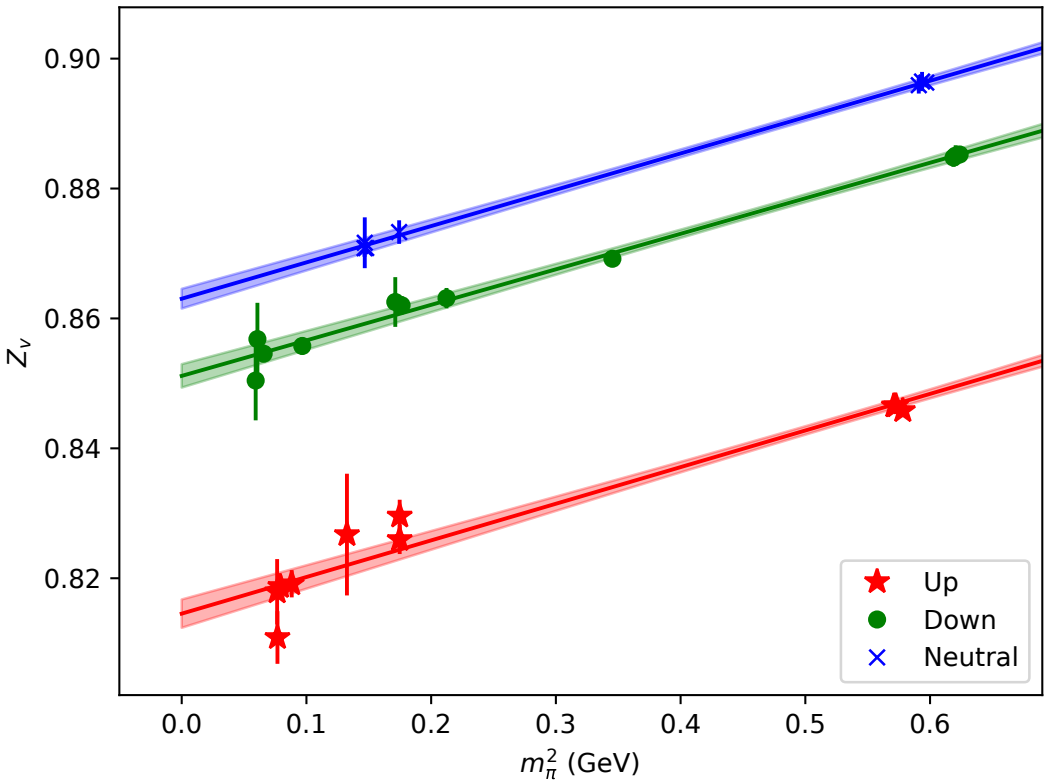

Figure 6.3. Vector current renormalisation as a function of the neutral pseudoscalar meson mass (squared) for each quark charge, where up indicates a charge of $+\frac{2}{3}$, down is $-\frac{1}{3}$ and neutral has zero charge. Each charge forms a distinct trend.

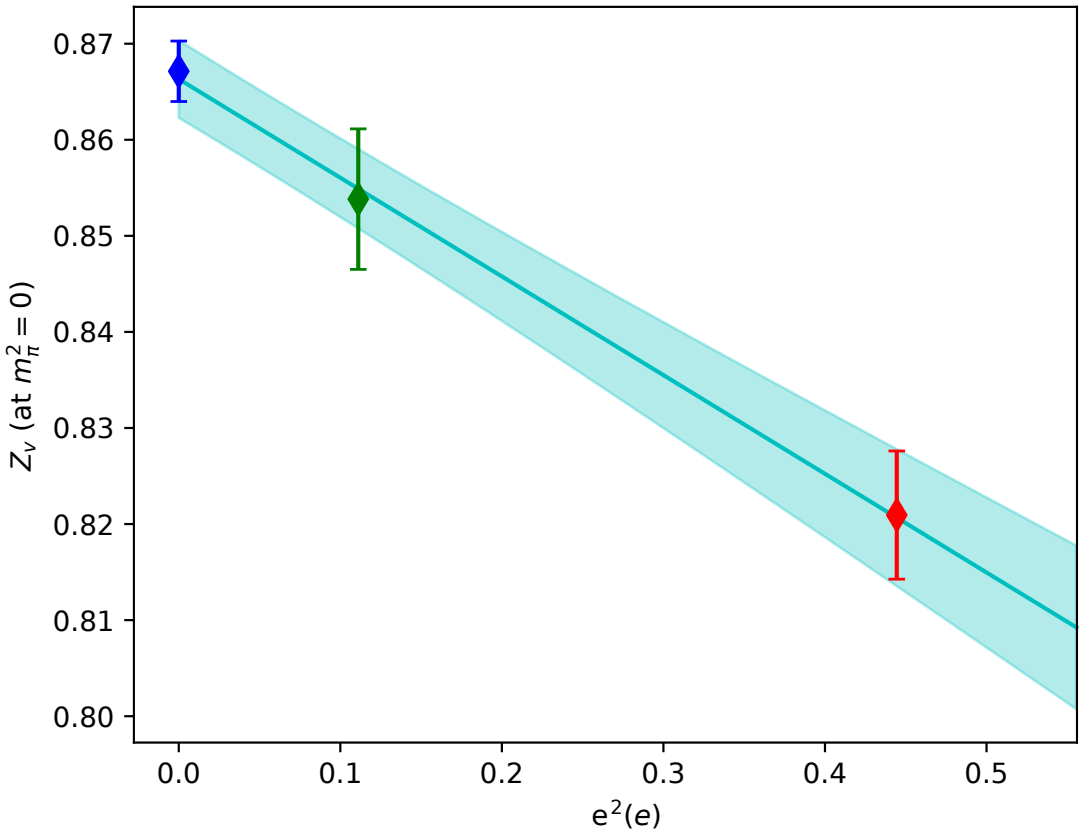

Figure 6.4. Z_v^f values for each quark flavour, extrapolated to the chiral limit. This shows a linear e_f^2 dependence, and agrees with results found in pure QCD studies at $e_f^2 = 0$. x-axis shows quark charge squared, in units of electron charge.

6.4. $\mathcal{O}(a)$ Improvements

As mentioned at the start of this chapter, the improvement coefficient c_ν in Eq. 6.7 is currently unknown for the gauge field configurations used in this work, and as such we are unable to completely remove $\mathcal{O}(a)$ artefacts from our simulations. We are, however, able to get an idea of the size of the remaining $\mathcal{O}(a)$ corrections by looking at the last term in Eq. 6.7,

$$\frac{\partial_\nu T_{\mu\nu,f}}{V_{\mu,f}}. \tag{6.21}$$

By defining the correlation function,

$$G^f_\nu(t) = -\frac{a^3}{3}\sum_{k=1}^{3}\sum_{\vec{x}} q_f^2 \left\langle V^{PS}_{k,f}(t,\vec{x}) T_{k\nu}(0)\right\rangle , \tag{6.22}$$

taking the divergence, $\partial_\nu G^t_\nu(t)$, we can then write Eq. 6.21 as the ratio

$$\frac{\partial_\nu T_{\mu\nu,f}}{V_{\mu,f}} = \frac{G^f_\nu(t)}{G^f(t)}, \tag{6.23}$$

where $G^f(t)$ is defined in terms of the mixed point-split/local correlator of Eq. 6.6, and computed on the lattice via

$$G^f(t) = -\frac{a^3}{3}\sum_{k=1}^{3}\sum_{\vec{x}} q_f^2 Z_V^{m_f} \left\langle V^{PS}_{k,f}(t,\vec{x}) V^{local}_{k,f}(0)\right\rangle . \tag{6.24}$$

For sufficiently large Euclidean times we should get a constant value, giving the improvement term multiplying c_ν in Eq. 6.7. In Figure 6.5 we show this ratio, for 3 different quark charges ($q_f = 0, -\frac{1}{3}, \frac{2}{3}$) at the Dashen tuned $SU(3)_{\text{flavour}}$-symmetric point. This result indicates that the matrix element for the improvement term is nearly an order of magnitude smaller than the signal term, and is also independent of the quark charge.

We can also note that $c_\nu = 0$ at tree level, and is expected to contribute at $\mathcal{O}\left(e^2\right)$. As this term is small and expected to be largely charge-independent, when combined with the ratio, $\frac{\partial_\nu T_{\mu\nu}}{V_\mu}$, which is also small and charge-independent, we have confidence that discretisation effects will be negligible for determining the EM effects in a_μ, which is the major aim of this work.

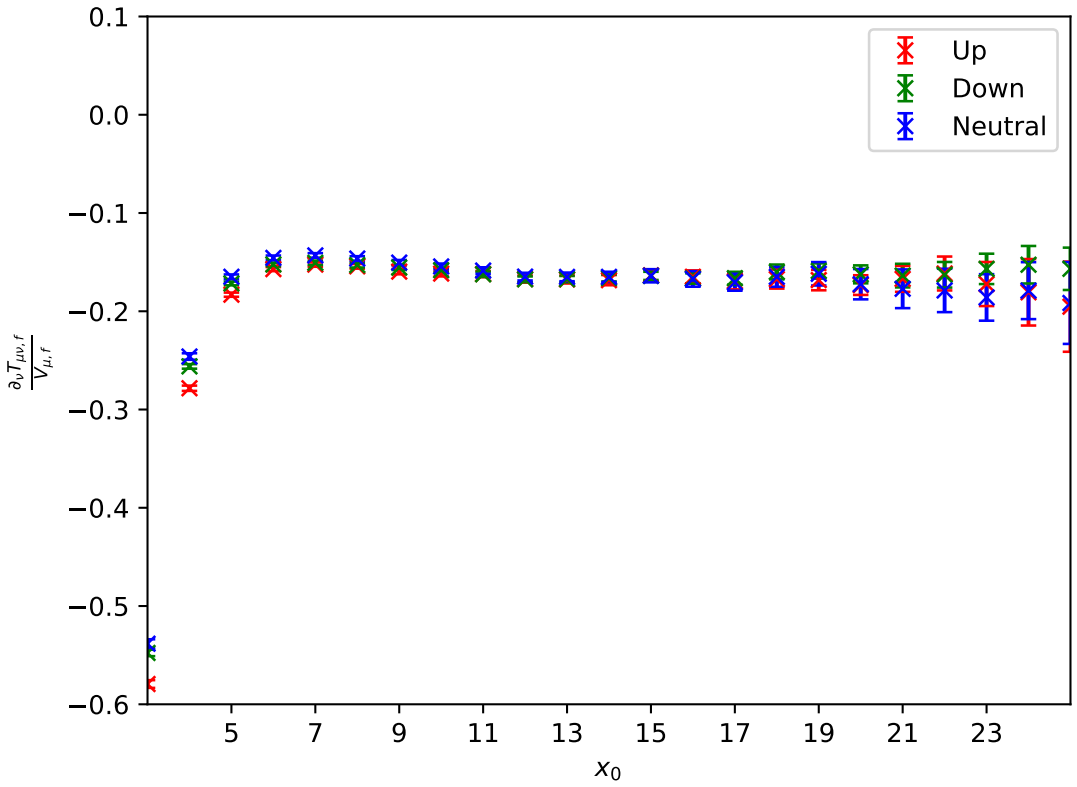

Figure 6.5. The ratio $\frac{\partial_\nu T_{\mu\nu,f}}{V_{\mu,f}}$ for three quark charges, $e_f = (\frac{2}{3}, -\frac{1}{3}, 0)$. This result indicates the term is charge independent, and small.

Chapter 7.

g-2 on the lattice

There are two popular methods for calculating the HVP contribution to the anomalous magnetic moment on the lattice; computing and using the vacuum polarisation tensor directly [103], and the time-momentum method [104]. Both of these methods are explored in order to gain a better understanding of any systematics which may be present, and will be explained in this chapter. In this chapter we will only consider the connected contributions, and will have a look at an initial investigation of the disconnected contributions in Chapter 9.

The first method, which we will refer to as the vacuum polarisation tensor method, provides us with a simple way to check the presence of any finite-volume effects [105], and give a first look into the relative magnitude of these effects between the two volumes used in this work. The vacuum polarisation tensor method used here will serve as our initial investigation into calculating a_μ^{HVP} on the lattice.

The second method, the time-momentum representation [104], is a more recent method of calculating the HVP term to a_μ on the lattice. This technique has quickly become one of the dominant methods of calculation on the lattice, and is the method used to obtain the majority of the results in this work.

As mentioned in Section 5.2, we only include contributions from the up, down and strange quarks. Due to the inclusion of QED effects, we do not have any up/down degenerate 'light' quarks as in some studies, but do use a down/strange degenerate 'negative' quark at and around the SU(3) symmetric point.

7.1. Hadronic Vacuum Polarisation Tensor

We can express the leading order HVP contribution to the anomalous magnetic moment of the muon, using the method proposed in [103, 106, 107], as

$$a_\mu^{\text{HVP,LO}} = \left(\frac{\alpha}{\pi}\right)^2 \int_0^\infty dQ^2 K(Q^2; m_\mu^2)\hat{\Pi}(Q^2), \tag{7.1}$$

where $m_\mu = 0.1056$ GeV is the muon mass, Q^2 is the Euclidean momentum flowing though the quark loop, and $K(Q^2; m_\mu^2)$ is a known QED kernel function,

$$K(Q^2; m_\mu^2) = m_\mu^2 Q^2 Z^3(Q^2) \frac{1 - Q^2 Z(Q^2)}{1 + m_\mu^2 Q^2 Z^2(Q^2)}, \tag{7.2}$$

$$Z(Q^2) = \left(\sqrt{Q^4 + 4m_\mu^2 Q^2} - Q^2\right) / (2m_\mu^2 Q^2). \tag{7.3}$$

$\hat{\Pi}(Q^2)$ is the subtracted vacuum polarisation function,

$$\hat{\Pi}(Q^2) = 4\pi^2 \left(\Pi(Q^2) - \Pi(0)\right), \tag{7.4}$$

where the polarisation function, $\Pi(Q^2)$, is determined from the polarisation tensor

$$\Pi_{\mu\nu}(Q) = \int d^4x\, e^{iQ\cdot x} \langle J_\mu(x) J_\nu(0)\rangle = (\delta_{\mu\nu} Q^2 - Q_\mu Q_\nu)\Pi(Q^2), \tag{7.5}$$

and finally $J_\mu(x)$ is the electromagnetic vector current.

We can think of Eq. 7.1 as mapping onto Figure 7.1, where the QED kernel K contains the information about the muon and photon vertices, and the polarisation function, $\hat{\Pi}$, contains the hadronic $q\bar{q}$ loop.

This method of calculating a_μ^{HVP} has a few difficulties, which we will attempt to address. Firstly, the integrand in Eq. 7.1 is peaked at small momentum, around the region $Q^2 \approx m_\mu^2/4 \approx 0.01\,\text{GeV}^2$. As mentioned in Section 5.2.4, the available momentum states on the lattice are discretised based on the lattice spacing and the spatial volume. This puts a limit on the resolution we can have in the data in the region which contributes most to the integrand.

One can attempt to get around this limitation by using twisted boundary conditions in order to access lower momentum [108–110], however this was not investigated in this work.

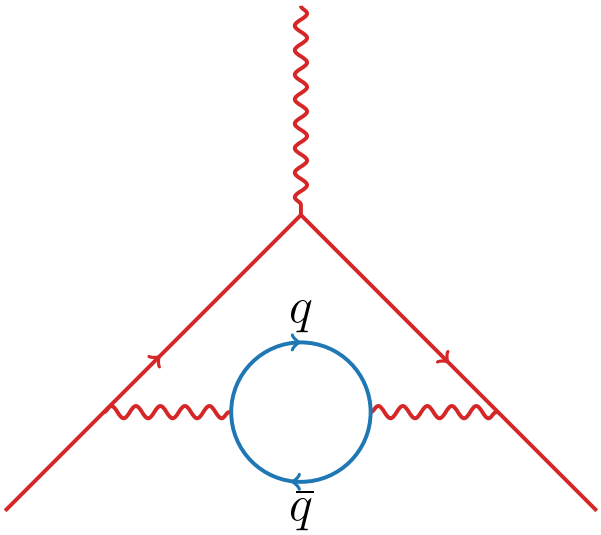

Figure 7.1. Leading order diagram for the HVP contribution to the anomalous magnetic moment. This diagram can be mapped onto Eq. 7.1. The QED kernel, K, represents the parts marked in red, while the polarisation function, $\hat{\Pi}$, represents the hadronic loop marked in blue.

The second difficulty comes from calculating the subtracted vacuum polarisation function. This requires us to know $\Pi(0)$, but Eq. 7.5 is undefined at $Q = 0$, which forces us to obtain $\Pi(0)$ by performing an extrapolation to $Q^2 = 0$. This runs the risk of introducing model dependence into our evaluation of $\hat{\Pi}(Q^2)$. This also leads back into the first difficulty, as the accuracy of $\hat{\Pi}(Q^2)$ is going to depend on the accuracy of our extrapolation at $Q^2 = 0$, which in turn is limited by the available of low Q^2 data.

In the next section we will give an overview of how we compute this on the lattice, using the $32^3 \times 64$ volume symmetric point ensemble as an example, and compare the results with a larger $48^3 \times 96$ volume lattice with the same quark masses in order to test for the presence of finite-volume effects.

7.1.1. Calculating on the lattice

The lattice vacuum polarisation tensor for quark flavour, f, computed in this work is

$$\Pi^f_{\mu\nu}(Q) \equiv Z_v^{m_f} q_f^2 \sum_x e^{i\hat{Q}\cdot x} \langle V^{PS}_{\mu,f}(x) V^{local}_{\nu,f}(0) \rangle \,, \tag{7.6}$$

where we have Fourier transformed into momentum space, $Z_v^{m_f}$ is the vector current renormalisation discussed in Chapter 6, q_f is the charge of a quark with flavour f, and

$\hat{Q}_\mu$ is the discrete momentum, $\hat{Q}_\mu = \frac{2\pi n_\mu}{L_\mu}$ where n_μ is the integer momentum number, and L_μ is the lattice extent, both in the μ direction. The PS and $local$ labels refer to the point-split and local current operators defined in Chapter 6.

At this stage we set $q_f^2 = 1$ in Eq. 7.6, such that the polarisation tensor is weighted the same for all quark flavours, and reintroduce the q_f^2 term with the appropriate value when combining the contributions for individual quark flavours to calculate the total $a_\mu^{\text{HVP,LO}}$ contribution.

From here, we will use the lattice momentum

$$Q_\mu = \frac{2}{a} \sin\left(\frac{a\hat{Q}_\mu}{2}\right), \tag{7.7}$$

which we associate with the continuum momentum, and better satisfies the Ward-Takahashi identity at finite lattice spacing, which we will see below.

It has been noted in Refs. [105] and [104] that the vacuum polarisation tensor is non-zero at $Q = 0$ in finite-volume, *i.e.* $\Pi_{\mu\nu}(0) \neq 0$. In order to reduce any finite-volume effects, we can subtract the unphysical constant $\Pi_{\mu\nu}(0)$ from the polarisation tensor by modifying Eq. 7.6 to

$$\hat{\Pi}^f_{\mu\nu}(Q) \equiv \Pi^f_{\mu\nu}(Q) - \Pi^f_{\mu\nu}(0) = Z_v^{m_f} \sum_x (e^{i\hat{Q}\cdot x} - 1) \left\langle V^{PS}_{\mu,f}(x) V^{local}_{\nu,f}(0) \right\rangle . \tag{7.8}$$

Before attempting to compute the vacuum polarisation function in Eq. 7.5, we first verify that the vector correlator satisfies the Ward-Takahashi identity. If both vector currents were fully conserved, we would expect

$$Q_\mu \hat{\Pi}_{\mu\nu}(Q) = 0 = \hat{\Pi}_{\mu\nu}(Q) Q_\nu. \tag{7.9}$$

However, as we only have the conserved vector current at the first index, this only holds true at the sink, and is violated by the local current:

$$\begin{aligned} Q_\mu \hat{\Pi}_{\mu\nu}(Q) &= 0, \\ \hat{\Pi}_{\mu\nu}(Q) Q_\nu &\neq 0. \end{aligned} \tag{7.10}$$

In Ref. [111] they show that additional irrelevant operators introduced into the lattice action modify the Ward identity for $\hat{\Pi}_{\mu\nu}$. The Schwinger-Dyson equation for $\hat{\Pi}_{\mu\nu}$

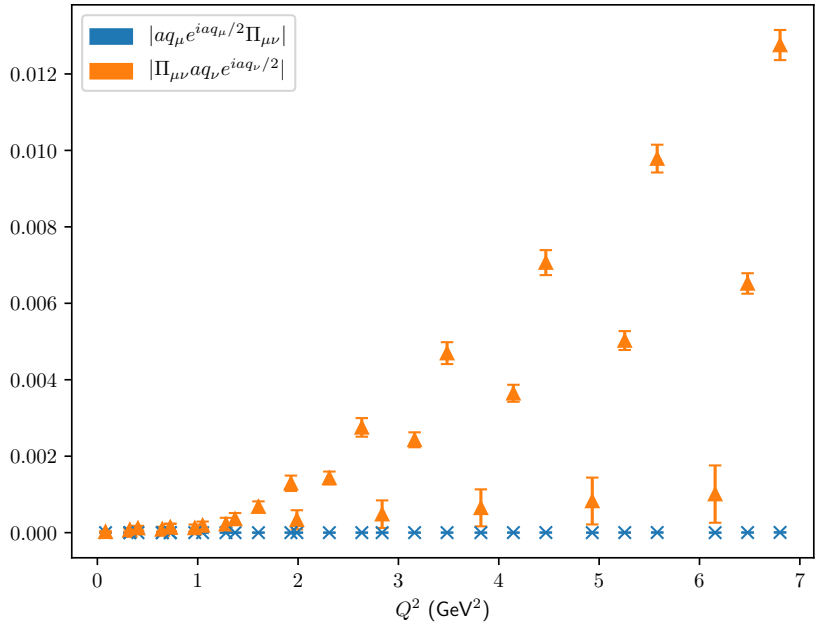

Figure 7.2. Modified Ward-Takahashi identify. It is correctly conserved for the point-split (blue cross), but not the local current (orange triangle).

in coordinate space is

$$\langle \left(\Delta_\mu V_\mu^{PS}(x)\right) V_\nu^{local}(0)\rangle + \left\langle \left(\frac{V_\nu^{local}(0)\overleftarrow{\partial}}{\partial\psi(x)}\psi(x) \right) - \left(\bar{\psi}(x)\frac{V_\nu^{local}(0)\overleftarrow{\partial}}{\partial\bar{\psi}(x)} \right) \right\rangle = 0, \quad (7.11)$$

where Δ_μ is the backwards lattice derivative. As the local current is not conserved, the second term here vanishes, and we are left with the modified Ward identity

$$\sum_\mu e^{iaQ_\mu/2} Q_\mu \hat{\Pi}_{\mu\nu} = 0. \quad (7.12)$$

Figure 7.2 shows this modified Ward-Takahashi identity is correctly conserved for the point split vector current.

We can now extract the vacuum polarisation function $\Pi(Q^2)$ as defined in Eq. 7.5. We choose momenta up to $Q^2 = 7$ GeV^2, including momenta limited to both the spatial and temporal directions independently, as well as terms with mixed momentum. In order to calculate the subtracted vacuum polarisation function, we need to extrapolate back to $Q^2 = 0$. As the integrand in Eq. 7.1 is very sensitive to the small Q^2 region, any

N	M	χ^2/dof	$\Pi(0)$
1	1	95.73	-0.1603(60)
1	2	13.54	-0.1505(4)
2	2	0.814	-0.1409(6)
2	3	0.544	-0.1425(17)

Table 7.1. Padé approximations of order $[N, M]$, showing the χ^2 value of the fit, as well as extracted $\Pi(0)$ value. The choice of $[2, 2]$ gives the most precise results with an acceptable χ^2.

systematics or model dependent effects around $Q^2 = 0$ can had a large effect on the calculated value of $a_\mu^{\text{HVP,LO}}$.

Following the suggestion in [112], we use a Padé approximation of order $[N, M]$ to fit the polarisation function,

$$\Pi_{[N,M]}(Q^2) = \Pi(0) + \frac{a_1 Q^2 + a_2 Q^4 + ... + a_N Q^{2N}}{1 + b_1 Q^2 + b_2 Q^4 + ... + b_M Q^{2M}}. \tag{7.13}$$

We found that an order $[2, 2]$ Padé approximation had an acceptable χ^2/dof while also giving a small statistical uncertainty, and is used to fit the data and provided a precise value for $\Pi(0)$. Table 7.1 shows an example of the results from different choices on N and M.

The calculated values for $\Pi(Q^2)$ are shown in Figure 7.3, along with the fitted $\Pi_{[2,2]}(Q^2)$. Using this extrapolation, we are able to calculate the subtracted vacuum polarisation function in Eq. 7.4. This is shown in Figure 7.4.

It should be noted that while in theory we need to evaluate the integral in Eq. 7.1 to $Q^2 = \infty$, the kernel function $K(Q^2; m_\mu^2)$ suppresses any contribution from high Q^2. The region $Q^2 > 5\text{GeV}^2$ contributes less than 0.07% to the total integral, which is well below the level of uncertainty in our data, hence we can truncate our integral at the largest Q^2 value in our datasets. Evaluating the integral on this ensemble we get a result for $a_\mu^{HVP,LO} = 6.88(48) \times 10^{-8}$.

So far the results shown have been calculated on a lattice with volume $32^3 \times 64$ and $a = 0.068$ fm, which allows a smallest Q^2 value of 0.0811 GeV^2, which is a significant distance away from the peak of the integrand, at approximately 0.01 GeV^2.

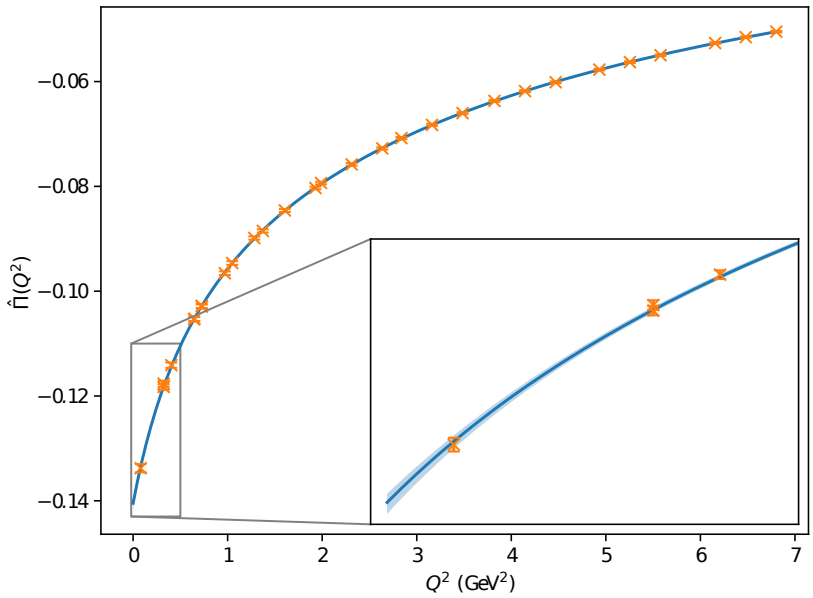

Figure 7.3. The vacuum polarisation function (Eq. 7.5) and Padé $[2, 2]$ fit, showing extrapolation to $Q^2 = 0$.

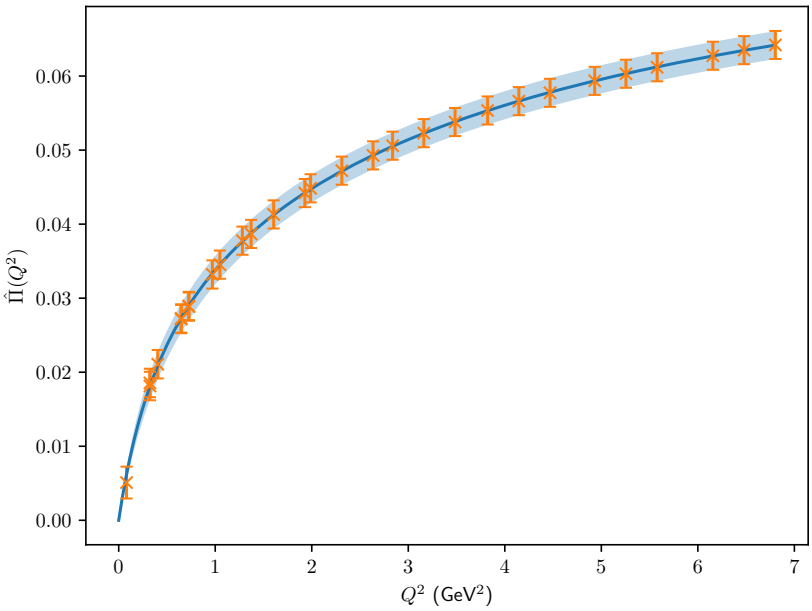

Figure 7.4. The subtracted vacuum polarisation function (Eq. 7.4), using the value for $\Pi(0)$ obtains from the Padé $[2, 2]$ fit shown in Figure 7.3.

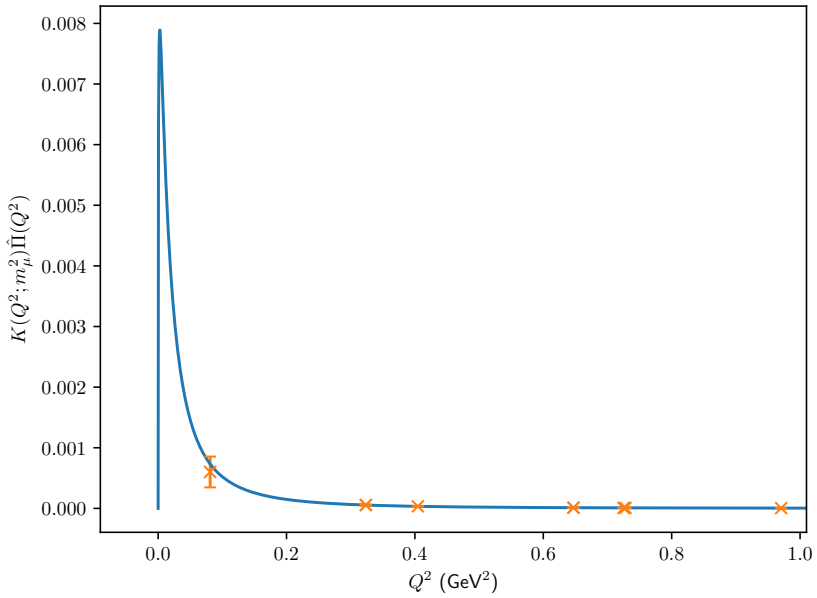

Figure 7.5. The integrand of Eq. 7.1, computed on the $32^3 \times 64$ volume lattice.

To try and get a more accurate representation of the integrand, a larger lattice is used with volume $48^3 \times 96$ and the same lattice spacing and quark masses as before. This allows us to access a smallest Q^2 of 0.036 GeV^2. Figure 7.6 shows the same integrand, evaluated on a $48^3 \times 96$ volume lattice with the same lattice spacing and quark mass as above. The higher resolution at of the low Q^2 region allows us to evaluate the integral with higher precision, resulting in a value of $a_\mu^{HVP,LO} = 6.48(27) \times 10^{-8}$.

7.1.2. Irreducible representations

We can see in the previous section that the limited availability of low momentum due to the finite-volume limits the precision with which we can resolve the integral up to. In addition to reducing the availability of lower momentum values, the finite lattice volume can have other effects on the calculation of the anomalous magnetic moment.

One way in which we can investigate the relative size of any finite-volume effect is suggested in [105]. It is proposed that in the finite-volume, Eq. 7.5 can be defined in terms of five different irreducible representations of the cubic group, which are all

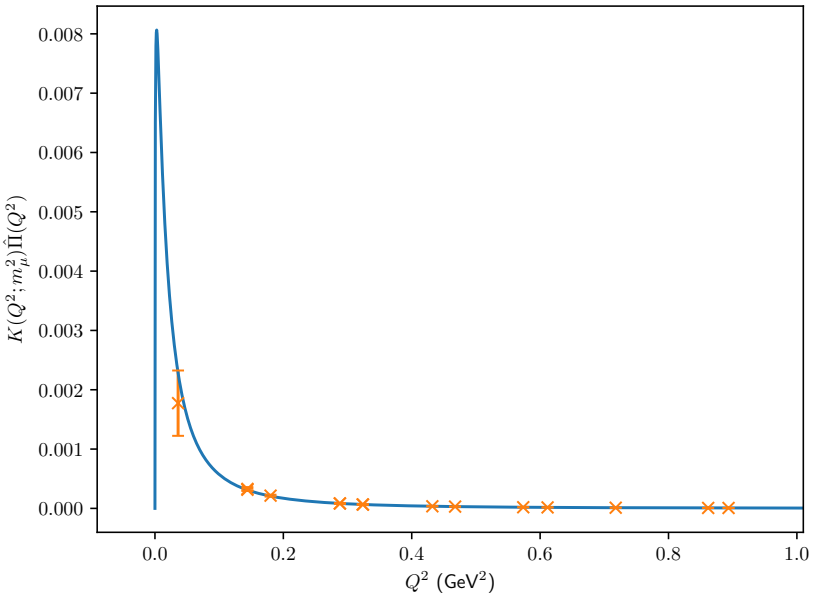

Figure 7.6. The integrand of Eq. 7.1, computed on the $48^3 \times 96$ volume lattice. Note that the larger volume allows us to access lower overall momentum values, as well as more choices in the low momentum region.

equal in the infinite-volume limit:

$$\begin{aligned}
A_1 &: \sum_i \Pi_{ii} = (3Q^2 - \vec{Q}^2)\Pi_{A_1}, \\
A_1^{44} &: \Pi_{44} = \vec{Q}^2 \Pi_{A_1^{44}}, \\
T_1 &: \Pi_{4i} = -Q_4 Q_i \Pi_{T_1}, \\
T_2 &: \Pi_{ij} = -Q_i Q_j \Pi_{T_2}, i \neq j, \\
E &: \Pi_{ii} - \sum_i \Pi_{ii}/3 = (-Q_i^2 + \vec{Q}^2/3)\Pi_E.
\end{aligned} \tag{7.14}$$

As these representations should all agree in the infinite-volume limit, by comparing the calculated values for the anomalous magnetic moment of the muon on a finite-volume using each of these representations, we should be able to determine the presence and relative size of any finite-volume effects in our data. We should note that we do not expect the uncertainties of all the representations to be similar, as the different representations rely on different momentum values. For example, Π_{A_1} allows us to access momenta with a single unit in the temporal direction, and none in the spatial directions, which is the smallest non-zero momentum accessible on our lattice. Π_{T_2} on the other hand requires at least one unit of momentum in two different spatial directions, which results in a Q^2 eight times larger than the minimum value for Π_{A_1}.

By considering each of these irreducible representations, we are able to repeat the method outlined above and compute a value for the anomalous magnetic moment of the muon. As these representations only differ due to finite-volume artefacts, any inconsistencies between the values is an indication of the presence of finite-volume effects. Table 7.2 shows the values for the anomalous magnetic moment calculated from each of these irreducible representations on two volumes at the same quark masses, first the $32^3 \times 64$, and then the $48^3 \times 96$ volumes. This is done using the up quark from ensemble C and F in Table 5.1. These values are also shown in Figure 7.7.

First looking at the results on the $32^3 \times 64$ volume, we see that there is a significant scatter between the values we compute for a_μ^{HVP} for the different representation, as well as large uncertainties for some of the representations which rely on larger values of momentum. In Figure 7.8, in order to remove some of the correlated statistical uncertainty, we display the deviation from 1 of the ratios of the results obtained from the various representations to that obtains using $\Pi_{A_1^{44}}$. This helps to highlight the disagreement in the results from the irreducible representations, which indicates the presence of significant finite-volume effects in the $32^3 \times 64$ volume.

Next comparing the results from the $48^3 \times 96$ volume, we can see the uncertainties are much smaller thanks to the small momentum values available to us. Here we see that four of the different representations agree with each other within uncertainty, but the value for $a_\mu^{\text{HVP,LO}}$ computed from the Π_{A_1} representation still differs from that calculated using the other representations. Looking at the ratio in Figure 7.8 we can see that the A_1 representation still produces a value for $a_\mu^{\text{HVP,LO}}$ that is statistically distinct from the other, which suggests that there are still some finite-volume effects present in the larger volume. However, there is a much higher level of agreement overall between the representations in the $48^3 \times 96$ than the smaller volume, which is expected. As the $48^3 \times 96$ volume is still not large enough to suppress finite-volume effects, we must be careful when considering the extrapolation towards the physical mass in the next section, and be careful to correct for these finite-volume effects.

7.2. Time-Momentum Representation

In the time-momentum representation, proposed in [104], the subtracted vacuum polarisation function in Eq. 7.4 can be expressed in terms of the spatially summed two-

	Volume	
Representation	$32^3 \times 64$	$48^3 \times 96$
A_1	$7.63(35) \times 10^{-8}$	$6.47(11) \times 10^{-8}$
A_1^{44}	$7.16(13) \times 10^{-8}$	$7.10(11) \times 10^{-8}$
T_1	$9.3(14) \times 10^{-8}$	$7.08(12) \times 10^{-8}$
T_2	$8.2(19) \times 10^{-8}$	$7.04(25) \times 10^{-8}$
E	$1.7(14) \times 10^{-7}$	$7.7(8) \times 10^{-8}$

Table 7.2. Values computed for a_μ^{HVP} on each of the representations listed in Eq. 7.14, on each volume, computed for the up quark from ensembles C and F from Table 5.1.

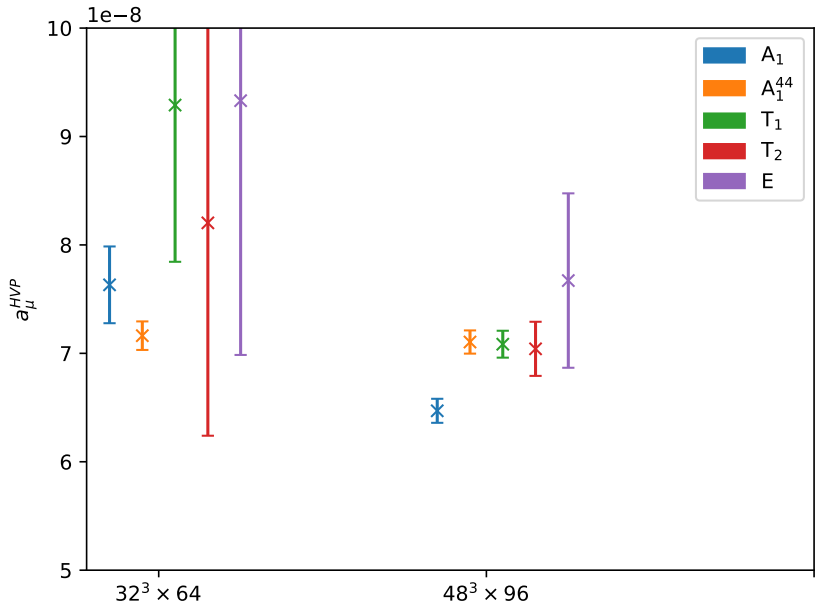

Figure 7.7. The anomalous magnetic moment evaluated on the different irreducible representations listed in Eq. 7.14, computed for the up quark from ensembles C and F from Table 5.1.

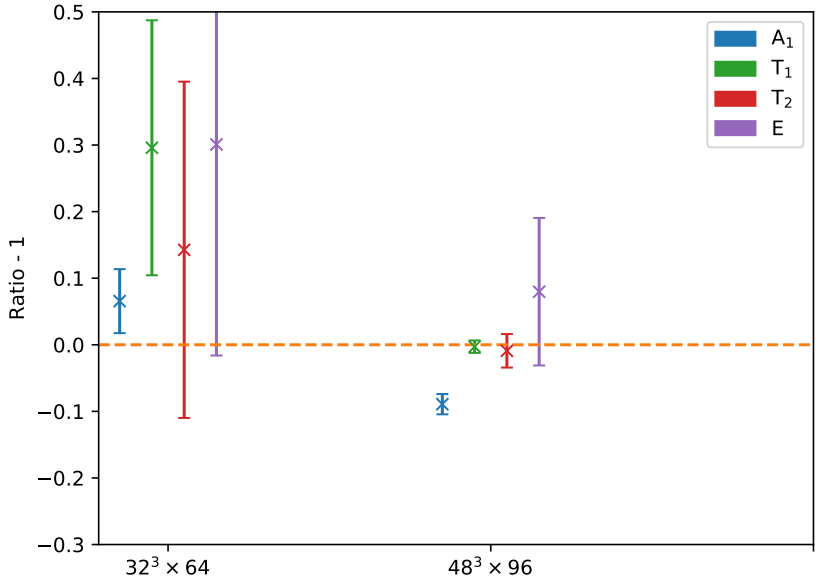

Figure 7.8. Correlated ratio of $a_\mu^{\text{HVP,LO}}$ computed from each representation listed in Eq. 7.14 with the A_1^{44} representation (minus 1), evaluated on each volume. This removes any correlated statistical uncertainty between the calculated values to better isolate any signs of finite-volume effects. The zero line (marked with the dashed line) shows when the value calculated from each representation is in agreement with that from the A_1^{44} representation.

point correlation function of the electromagnetic current, $G(x_0)$,

$$\hat{\Pi}(Q^2) = 4\pi^2 \int_0^\infty dx_0\, G(x_0) \left(x_0^2 - \frac{4}{Q^2} \sin^2\left(\frac{Qx_0}{2}\right)\right), \tag{7.15}$$

$$G(x_0) = -\sum_{i=1,2,3} \int d^3x\, \langle J_i(x)\, J_i(0)\rangle\,, \tag{7.16}$$

where we have zero spatial momentum.

If we take this form for the subtracted vacuum polarisation function, we can insert it into Eq. 7.1 and rearrange the integral to get

$$a_\mu^{\text{HVP,LO}} = \left(\frac{\alpha}{\pi}\right)^2 \int_0^\infty dx_0\, G(x_0) \tilde{K}(x_0; m_\mu), \tag{7.17}$$

where the x_0-dependent kernel function $\tilde{K}(x_0; m_\mu)$ is written in terms of the kernel function $K(Q^2; m_\mu^2)$ from Eq. 7.1,

$$\tilde{K}(x_0; m_\mu) = 4\pi^2 \int_0^\infty dQ^2\, K(Q^2; m_\mu^2) \left(x_0^2 - \frac{4}{Q^2} \sin^2\left(\frac{Qx_0}{2}\right)\right). \tag{7.18}$$

We employ a numerical from of $\tilde{K}(x_0; m_\mu)$, which is derived in [113]. This is written as

$$\begin{aligned} m_\mu^2 \tilde{K}(x_o) =& \frac{\pi^2 \hat{x}_0^4}{9} + \frac{\pi^2 \hat{x}_0^6 (120 \ln(\hat{x}_0) + 120\gamma_E - 169)}{5400} \\ &+ \frac{\pi^2 \hat{x}_0^8 (210 \ln(\hat{x}_0) + 210\gamma_E - 401)}{88200} + \frac{\pi^2 \hat{x}_0^{10} (360 \ln(\hat{x}_0) + 360\gamma_E - 787)}{2916000} \\ &+ \frac{\pi \hat{x}_0^{12} (3080 \ln(\hat{x}_0) + 3080\gamma_E - 7353)}{768398400} + \mathcal{O}(\hat{x}_0^{14}), \end{aligned} \tag{7.19}$$

where $\hat{x}_0 \equiv m_\mu x_0$ and γ_E is Euler's constant. This expression is used up to $\hat{x}_0 = 1.05$, where the relative accuracy is better than 3.3×10^{-6}. For $\hat{x}_0 \geq 1.05$ we use the expression [113]

$$\begin{aligned} m_\mu^2 \tilde{K}(x_0) =& 2\pi^2 \hat{x}_0^2 - 4\pi^3 \hat{x}_0 + 4\pi^2 (4 \ln(\hat{x}_0) + 4\gamma_E - 1) + \frac{8\pi^2}{\hat{x}_0^2} \\ &- \frac{2\pi^{5/2}}{\sqrt{\hat{x}_0}} e^{-2\hat{x}_0} \big(0.0197159 (\hat{x}_0^{-1} - 0.7)^6 - 0.0284086 (\hat{x}_0^{-1} - 0.7)^5 \\ &+ 0.0470604 (\hat{x}_0^{-1} - 0.7)^4 - 0.107632 (\hat{x}_0^{-1} - 0.7)^3 \\ &+ 0.688813 (\hat{x}_0^{-1} - 0.7)^2 + 4.71371 (\hat{x}_0^{-1} - 0.7) + 3.90388 \big), \end{aligned} \tag{7.20}$$

which has a similar accuracy for all $\hat{x}_0 \geq 1.05$.

7.2.1. Calculating on the lattice

When computing the vector correlator on the lattice, the two-point correlation function $G(x_0)$ is written as

$$G^f(x_0) = -\frac{a^3}{3} \sum_{\mu=1}^{3} q_f^2 Z_V^{m_f} \sum_{\vec{x}} \langle V_{\mu,f}^{PS}(x) V_{\mu,f}^{local}(0) \rangle \,, \tag{7.21}$$

where as before, we will set the charge term $q_f^2 = 1$ at this stage such that the correlators for each quark flavour are weighted the same. We will include the correct charge factors when combining the different quark flavours together to calculate the total $a_\mu^{\text{HVP,LO}}$ contribution.

In order to evaluate the integral in Eq. 7.17, we are required to know $G(x_0)$ to infinite time. Of course on a finite lattice, we can only evaluate the correlator up to some finite time. Additionally, as we approach the middle time slices, the signal is contaminated

with noise from the backwards propagating state due to the anti-periodic boundary conditions used.

In order to overcome this, we must split the correlation function $G(x_0)$ into two parts for small and large x_0. We perform this split at $x_0 = x_0^{\text{cut}}$, such that

$$G^f(x_0) = \begin{cases} G^f(x_0)_{\text{data}} & x_0 \leq x_0^{\text{cut}}, \\ G^f(x_0)_{\text{ext}} & x_0 > x_0^{\text{cut}}. \end{cases} \tag{7.22}$$

For $G^f(x_0)_{\text{data}}$, we perform a cubic spline interpolation on the numerical data to obtain a continuous form of the correlator. For $G^f(x_0)_{\text{ext}}$, we are required to fit some functional form to the lattice data, which we can then extrapolate to large time.

The obvious functional form to fit to the correlator is a sum of exponentials,

$$G^f(x_0)_{\text{ext}} = \sum_i^N A_i e^{-E_i x_0}, \tag{7.23}$$

where we have included the first N energy states, starting from the ground state, and then adding the first, second, and so on excited states. For large x_0 the signal is dominated by the ground state, and as we include smaller values of x_0 the first, and then second and so on, excited states start to contribute more significantly. In this investigation we have included up to the first three energy states (that is the ground state and first two excited states) in order to ensure we have an accurate extrapolation of the correlator $G^f(x_0)_{\text{ext}}$ for values $x_0 > x_0^{\text{cut}}$.

These fits are all performed on a window starting from x_0^{cut} and extend until the signal is either lost to noise, or until contamination from the backwards propagating states become statistically significant. The fit windows are further fine tuned using a correlated χ^2/dof metric. In Table 7.3 an example (using the lightest negative quark from Ensemble B) of the fitted energy state is shown for one, two and three state fits, as well as Figure 7.9 showing these fits against the raw correlator data. By including the higher energy states in the fit, we are able to use a smaller value of x_0^{cut}. We can see that all three fits give consistent results for the ground state energy, as well as the first excited state on the two and three state fits. However the two, and particularly the three, state fits are less well constrained than the single state fit. The higher state fits are also more sensitive to small statistical fluctuations in the data. Hence, in our analysis we use the single exponential fit in order to construct $G^f(x_0)_{\text{ext}}$, however we are able

State	E_0	E_1	E_2	$a_\mu^{\text{HVP,LO}}$
1	$0.282(11)$	-	-	$798(54) \times 10^{-10}$
2	$0.276(14)$	$0.709(68)$	-	$809(59) \times 10^{-10}$
3	$0.246(77)$	$0.56(21)$	$1.26(80)$	$822(304) \times 10^{-10}$

Table 7.3. Fitted energy states for $G^f(x_0)_{\text{ext}}$ for one, two and three state fits. Note that the ground state energy is consistent as we decrease x_0^{cut} and include more energy states, but the uncertainty in the fit values, as well as the value for $a_\mu^{\text{HVP,LO}}$ we calculate with it, increases as we fit earlier to include the higher states.

to use the multi-state fits in order to ensure that any contamination from excited states in the determination of E_0 are suppressed.

In Figure 7.9 it can been seen that after sufficiently large x_0^{cut} the single state fit agrees with the two state fit, and is a very accurate representation of the correlator data. This ensures us that the first excited state has sufficiently decayed by the point where our single state fit starts. While the two state fit also closely matches the correlator data, the uncertainty in the fit is greater than the very small statistical error on the early data points, which results in the later, single state fit reducing the overall uncertainty in $G(x_0)$. Much of the uncertainty in the multi-state fits comes from the high time region.

In addition to using the multi-state fits to ensure our choice of x_0^{cut} is sufficient for a single state fit, we can also use a method known as the bounding method.

The bounding method is an alternative approach of constraining the large-time dependence of the correlator $G(x_0)$, proposed in Ref. [114]. This method involves replacing our expression for $G^f(x_0)_{\text{ext}}$ in Eq. 7.23 with

$$G^f(x_0)_{\text{ext}} = G^f(x_0^{\text{cut}})e^{-E(x_0-x_0^{\text{cut}})}, \tag{7.24}$$

where we converge on a value for x_0^{cut} by setting an upper and lower bound for the energy E and choosing x_0^{cut} to be where Eq. 7.24 converged. The lower bound of E is determined from the local effective mass, $E_{\text{lower}} = \log\left(\frac{G^f(x_0^{\text{cut}})}{G^f(x_0^{\text{cut}}+1)}\right)$, while the upper bound uses the same ground state energy from the single state fit, $E_{\text{upper}} = E_0$.

The bounding method was checked in order to ensure the values chosen for x_0^{cut} agree.

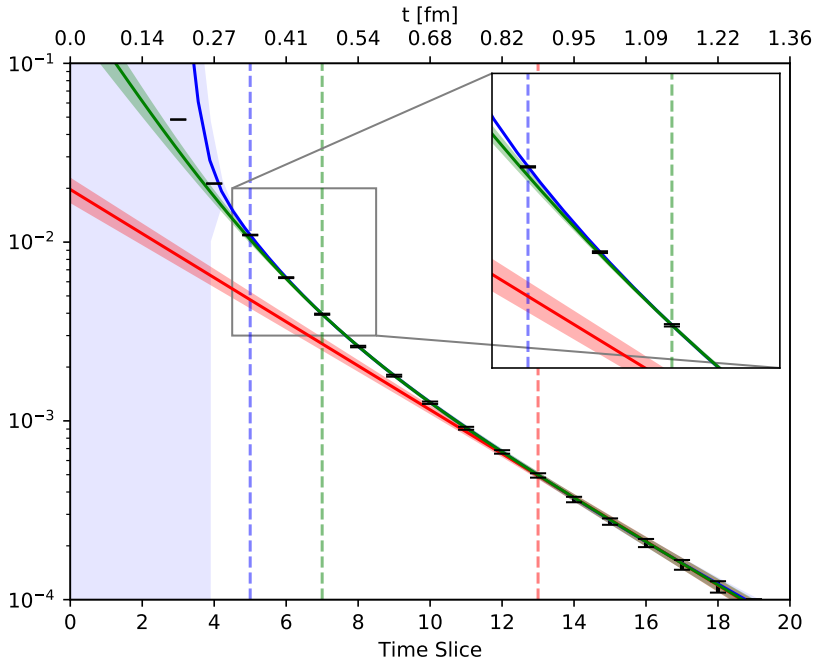

Figure 7.9. Multiple state fits to an example correlation function, $G(x_0)$ (shown by the black markers). The red, green and blue curves show the one, two and three state fits respectively, with the dashed vertical lines indicating the corresponding x_0^{cut} value for each fit.

Now that the large-time dependence is under control, we can look at computing Eq. 7.17 to get values for $a_\mu^{\text{HVP,LO}}$ on each ensemble. Figure 7.11 shows an example, again using the lightest negative quark on ensemble B, of the integrand, where $G(x_0)_{\text{data}}$ and $G(x_0)_{\text{ext}}$ are distinguished. We can see that after the cut point, $G(x_0)_{\text{ext}}$ closely matches the data until the signal is lost to noise and backwards propagating states, at which point $G(x_0)_{\text{ext}}$ continues to decay towards zero. Due to this asymptotic behaviour we are able to evaluate the integral numerically.

By performing this process over all ensembles, we are able to calculate values for $a_\mu^{\text{HVP,LO}}$ for all of our different quark charges and masses. These values are shown in Table 7.5.

7.2.2. Flavour-breaking expansion

Now that we have calculated values for $a_\mu^{\text{HVP,LO}}$ for a range of different quark charges and masses, we need a way to extrapolate these values to the physical quark mass. As the SU(3) flavour properties of $a_\mu^{\text{HVP,LO}}$ are the same the vector meson mass, we

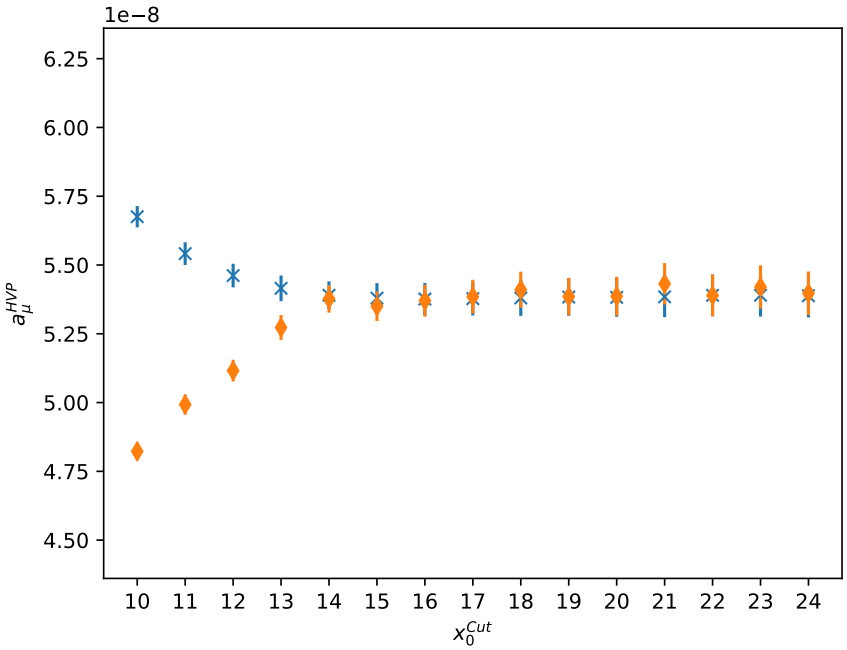

Figure 7.10. Bounding method example for the strange quark (line 6) on ensemble C in Table 7.5. We see the upper and lower bounds converging after $x_0^{\text{cut}} = 14$, which agrees with the chosen x_0^{cut} value for the single state exponential fit.

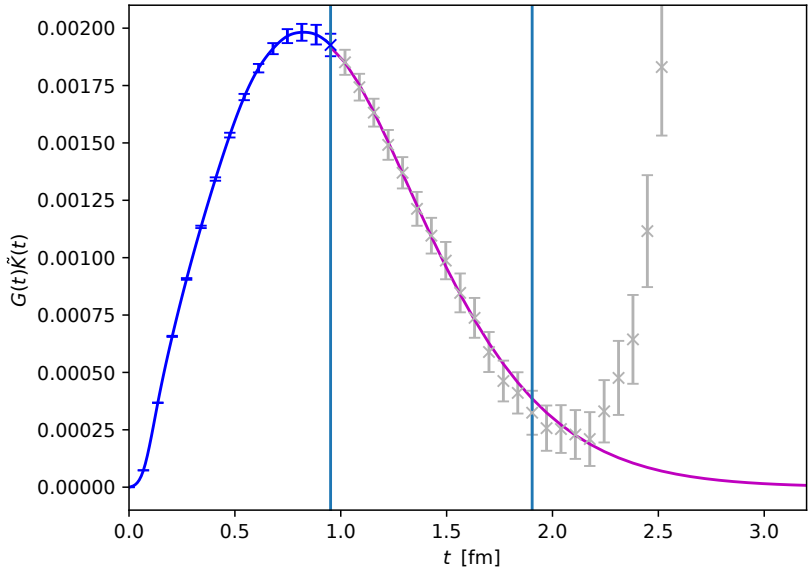

Figure 7.11. Plot of the full integrand in Eq. 7.17. Blue points are the integrand data used in $G(x_0)_{\text{data}}$, with the blue curve showing the cubic spline. The magenta curve is the single exponential fit showing $G(x_0)_{\text{ext}}$. x_0^{cut} is marked with the first vertical line, while the second vertical line marks the end of the fit window used to constrain $G(x_0)_{\text{ext}}$. The grey crosses mark the integrand from the raw lattice data, showing $G(x_0)_{\text{data}}$ after x_0^{cut}. We can see that $G(x_0)_{\text{ext}}$ matches the data closely in the fit window.

can apply the same flavour-breaking expansion presented in Section 5.2.5 for $a_\mu^{\text{HVP,LO}}$ to extrapolate to the physical quark masses, starting with the flavour expansion of an octet quantity of a vector meson, from Eq. 5.21, and replacing the valence quark mass with the Dashen scheme quark mass.

This expansion can be written as

$$\begin{aligned} a_\mu^{\text{HVP,LO}}(q\bar{q}) = a_{\mu,0}^{HVP} &+ 2\alpha\delta\mu_q^D + \frac{1}{6}\beta_0(\delta m_u^2 + \delta m_d^2 + \delta m_s^2) + 2\beta_1(\delta\mu_q^D)^2 \\ &+ 2\beta_1^{EM} e_q^2 + \gamma_0^{EM}(e_u^2\delta m_u + e_d^2\delta m_d + e_s^2\delta m_s) + 2\gamma_1^{EM} e_q^2 \delta\mu_a^D \\ &+ 2\gamma_5^{EM} e_q(e_u\delta m_u + e_d\delta m_d + e_s\delta m_s), \end{aligned} \tag{7.25}$$

where we have used the Dashen mass defined in Section 5.2.6.

Using this expansion, we are able to perform a fit to the individual a_μ values. This is shown in Figure 7.12, where we have performed the fit over all quark flavours, and plotted the extrapolation in terms of the Dashen mass $\delta\mu_q^D$ for each quark charge. Note that in our extrapolation the down and strange quark are only distinct by mass, so share an expansion trajectory. In order to show this extrapolation on a 2D plot, we need to compress the extra dimensions so we only have $a_\mu^{\text{HVP,LO}}$ and $\delta\mu_q^D$ varying. To achieve this the sea quark masses $\delta m_{u,d,s}$ are fixed at the physical sea quark masses. This results in the data points shown in Figure 7.12 being shifted by the difference in Eq. 7.25 evaluated at each simulation point for the sea quark masses used and the physical sea quark mass.

In addition to the up quark and 'negative' (down/strange) quark extrapolation, we have also included the expansion for a fictitious neutral quark, where $e_n = 0$. This will provide a purely QCD signal to which charged quark results can be compared to in Chapter 8 in order to investigate the relative size of any QED corrections to the hadronic contribution of the anomalous magnetic moment of the muon.

Table 7.4 contains the fitted values for the free parameters in the flavour breaking expansion of $a_\mu^{\text{HVP,LO}}$ on the $48^3 \times 96$ volume.

Using this description for the full flavour-breaking effects of the individual quark contributions to $a_\mu^{\text{HVP,LO}}$, we are now able to read off the contribution from each quark at its respective physical quark mass. The physical quark masses are marked in Figure 7.12 by the vertical dashed lines and were determined in [84]. We can note the curious feature of performing the flavour-breaking expansion at the quark level along a quark

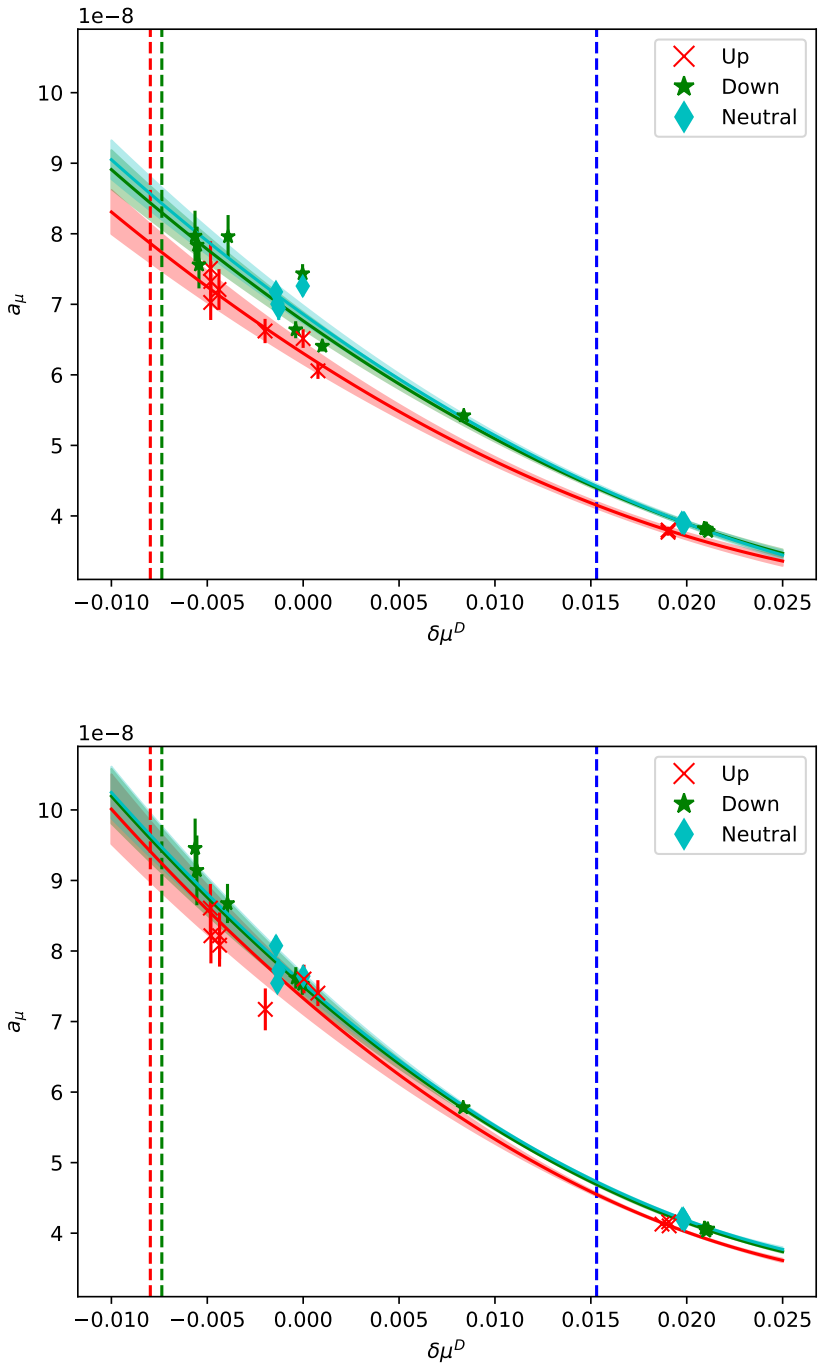

Figure 7.12. Flavour-breaking expansion for $a_\mu^{\text{HVP,LO}}$ plotted as a function of the Dashen mass. *Top*: $32^3 \times 64$ volume. *Bottom*: $48^3 \times 96$ volume. The red/green/blue vertical lines mark the location of the physical up/down/strange valence quark mass, while $\delta\mu^D = 0$ marks the SU(3)-symmetric point.

Parameter	Value	
$a_{\mu,0}^{\mathsf{HVP}}$	$7.30(16)$	$\times 10^{-8}$
α	$-1.181(9)$	$\times 10^{-6}$
β_0	$4.1(14)$	$\times 10^{-5}$
β_1	$1.71(27)$	$\times 10^{-5}$
β_1^{em}	$-2.29(84)$	$\times 10^{-9}$
γ_0	$1(18)$	$\times 10^{-8}$
γ_1	$2.6(43)$	$\times 10^{-8}$
γ_5	$9(15)$	$\times 10^{-9}$

Table 7.4. Fit parameters for flavour breaking expansion on $48^3 \times 96$ lattice volume.

Ensemble	Valence κ	Charge	$m_{\bar{q}q}$ [GeV]	$a\,m_v^{q\bar{q}}$	x_0^{cut}	χ^2/dof	a_μ^{HVP}
A	0.123 850	2/3	0.754(3)	0.370(2)	15	0.906	388(2)
	0.124 362	2/3	0.431(1)	0.321(6)	12	0.942	617(9)
	0.124 383 8	2/3	0.413(1)*	0.308(6)	12	1.265	663(10)
	0.124 520	2/3	0.270(2)	0.285(16)	12	1.357	762(35)
	0.121 100	−1/3	0.784(3)	0.368(2)	16	1.007	384(2)
	0.121 713	−1/3	0.407(1)	0.313(12)	17	1.087	665(11)
	0.121 702 6	−1/3	0.414(1)*	0.278(8)	16	1.156	745(12)
	0.121 865	−1/3	0.235(6)	0.277(15)	12	1.926	831(39)
	0.120 240	0	0.760(4)	0.360(3)	17	1.179	395(2)
	0.120 814 2	0	0.412(1)*	0.283(10)	18	1.038	731(13)
	0.120 855	0	0.378(1)	0.299(5)	13	1.122	722(10)
B	0.123 850	2/3	0.755(2)	0.368(1)	15	1.121	390(1)
	0.124 440	2/3	0.360(2)	0.331(34)	21	1.199	672(14)
	0.124 520	2/3	0.272(2)	0.302(11)	13	0.999	713(21)
	0.121 100	−1/3	0.788(2)	0.367(2)	20	0.918	385(1)
	0.121 676	−1/3	0.459(1)	0.312(4)	15	1.070	644(5)
	0.121 865	−1/3	0.243(2)	0.301(7)	11	1.579	762(19)
	0.120 240	0	0.770(2)	0.357(2)	22	1.144	396(1)
	0.120 855	0	0.369(2)	0.306(10)	17	1.325	706(10)
C	0.123 850	2/3	0.758(2)	0.8458(8)	15	1.092	387(2)
	0.124 508	2/3	0.293(2)	0.303(11)	11	0.809	728(26)
	0.124 520	2/3	0.280(2)	0.304(11)	12	0.998	711(23)
	0.121 100	−1/3	0.788(2)	0.375(2)	15	1.032	381(1)
	0.121 821	−1/3	0.307(2)	0.292(17)	15	1.477	799(29)
	0.121 466	−1/3	0.586(2)	0.328(3)	14	1.157	545(4)
	0.121 865	−1/3	0.255(2)	0.295(14)	13	1.400	759(31)
	0.120 240	0	0.771(2)	0.363(2)	17	1.077	394(2)
	0.120 855	0	0.384(1)	0.304(13)	17	0.984	699(14)

Table 7.5. $a_\mu^{\text{HVP,LO}}$ results on each ensemble for all choices of quark charge and valence kappa values. Ensemble details listed in Table 5.1, SU(3)-symmetric point marked with *. a_μ^{HVP} is in units of 10^{-10}, Charge is in units of e, $m_{\bar{q}q}$ is the neutral pseudoscalar meson mass, $a\,m_v^{q\bar{q}}$ is the ground state energy E_0. χ^2/dof values are from correlated fits.

Ensemble	Valence κ	Charge	$m_{\bar{q}q}$ [GeV]	$a\,m_v^{q\bar{q}}$	x_0^{cut}	χ^2/dof	a_μ^{HVP}
D	0.123 859	2/3	0.764(4)	0.366(3)	17	0.973	390(2)
	0.124 362	2/3	0.432(4)	0.285(11)	16	1.166	717(19)
	0.124 382 4	2/3	0.414(4)*	0.281(10)	16	1.162	737(21)
	0.124 520	2/3	0.255(5)	0.288(11)	11	0.939	838(35)
	0.121 100	−1/3	0.795(4)	0.372(2)	16	1.042	382(2)
	0.121 713	−1/3	0.410(3)	0.291(9)	14	1.259	737(19)
	0.121 703 2	−1/3	0.419(3)*	0.293(8)	14	1.223	728(19)
	0.121 865	−1/3	0.231(3)	0.270(14)	12	1.567	921(46)
	0.120 240	0	0.773(4)	0.368(2)	14	1.081	396(2)
	0.120 813 5	0	0.416(3)*	0.289(8)	14	1.260	740(18)
	0.120 855	0	0.384(2)	0.275(8)	15	1.310	784(17)
E	0.123 850	2/3	0.758(4)	0.367(3)	13	0.945	393(4)
	0.124 440	2/3	0.364(3)	0.317(32)	18	0.959	694(33)
	0.124 520	2/3	0.266(5)	0.288(14)	12	0.559	799(42)
	0.121 100	−1/3	0.791(4)	0.373(3)	18	0.909	379(3)
	0.121 676	−1/3	0.440(2)	0.363(36)	21	0.916	627(19)
	0.121 865	−1/3	0.230(9)	0.280(17)	12	1.348	890(55)
	0.120 240	0	0.777(4)	0.362(3)	16	1.273	397(4)
	0.120 855	0	0.380(2)	0.299(9)	13	1.189	731(16)
F	0.123 850	2/3	0.639(3)	0.364(3)	15	0.935	393(4)
	0.124 508	2/3	0.286(2)	0.287(15)	12	0.577	805(35)
	0.124 508	2/3	0.273(2)	0.290(17)	12	0.677	791(33)
	0.121 100	−1/3	0.751(3)	0.370(3)	15	0.992	388(3)
	0.121 821	−1/3	0.300(2)	0.318(19)	16	0.877	801(31)
	0.121 466	−1/3	0.580(4)	0.324(3)	13	0.974	560(6)
	0.120 240	0	0.689(4)	0.359(3)	18	1.161	401(3)
	0.120 855	0	0.366(5)	0.296(8)	13	1.078	755(19)

Table 7.5. $a_\mu^{\text{HVP,LO}}$ results on each ensemble for all choices of quark charge and valence kappa values. Ensemble details listed in Table 5.1, SU(3)-symmetric point marked with *. a_μ^{HVP} is in units of 10^{-10}, Charge is in units of e, $m_{\bar{q}q}$ is the neutral pseudoscalar meson mass, $a\,m_v^{q\bar{q}}$ is the ground state energy E_0. χ^2/dof values are from correlated fits.

Volume	Quark	$a_\mu^{\text{HVP,LO},q}$
$32^3 \times 64$	Up	$7.89(26) \times 10^{-8}$
$32^3 \times 64$	Down	$8.31(23) \times 10^{-8}$
$32^3 \times 64$	Strange	$4.39(2) \times 10^{-8}$
$48^3 \times 96$	Up	$9.41(43) \times 10^{-8}$
$48^3 \times 96$	Down	$9.42(31) \times 10^{-8}$
$48^3 \times 96$	Strange	$4.69(2) \times 10^{-8}$

Table 7.6. $a_\mu^{\text{HVP,LO}}$ for each quark flavour at the corresponding physical quark mass.

mass trajectory with the average neutral pseudoscalar mass held constant, results in the physical up and down quark masses being closer to the SU(3) flavour-symmetric point, $\delta\mu = 0$ than the physical strange quark mass ($\delta\mu_s = -\delta\mu_u - \delta\mu_d$). The extracted contribution from each quark quark flavour is shown in Table 7.6.

We can obtain the combined contribution from the up, down and strange quarks by summing the contributions of each quark flavour at their respective physical quark mass, weighted by reintroducing the squared quark charge term which we dropped by setting it to 1 in Eq. 7.21,

$$a_\mu^{\text{HVP,LO}} = \frac{4}{9}a_\mu^u + \frac{1}{9}a_\mu^d + \frac{1}{9}a_\mu^s. \tag{7.26}$$

By following this procedure on both lattice volumes, we find values for $a_\mu^{\text{HVP,LO}}$ on both:

$$32^3 \times 64 : a_\mu^{\text{HVP,LO}} = 492 \pm 15 \times 10^{-10}, \tag{7.27}$$
$$48^3 \times 96 : a_\mu^{\text{HVP,LO}} = 579 \pm 23 \times 10^{-10}. \tag{7.28}$$

The difference between the two volumes is not unexpected as we have seen the potential for significant finite-volume effects to be present, as observed in Section 7.1.2 and [104, 105]. In the next section, we will attempt to perform a finite-volume correction in order to account for this.

As a intermediate check, we can attempt to compare our results to other publications which present their results before and after applying finite-volume corrections. In

Ref. [113] they present competitive results for $a_\mu^{\text{HVP,LO}}$ using a set of lattices of similar volume to our $48^3 \times 96$ volume, as well as presenting their results before and after the finite-volume corrections are applied. The results in Ref. [113] are QCD only, but can still be used as a comparison. We will ignore QED corrections here, but come back to them in Chapter 8.

If we only consider their results for the up, down and strange quark (they also include the charm quark contribution which has been discounted here), prior to performing finite-volume corrections they find

$$a_\mu^{\text{HVP,LO}} = 602.4(248)(289) \times 10^{-10}, \tag{7.29}$$

which is consistent with our results on the $48^3 \times 96$ volume lattice.

7.2.3. Finite-volume corrections

As mentioned before, a_μ^{HVP} is known to have significant finite-volume effects, so we are required to perform finite-volume corrections to the lattice data. To do this we calculate the finite-volume correction term, $\Delta a_\mu^{\text{HVP}}$, for each ensemble and valence quark, which can then be added to the calculated a_μ^{HVP} on that ensemble for that particular valence quark before performing the flavour-breaking expansion listed in the previous section. We achieve this by following the method laid out in [113,115] for non-interacting pions.

$\Delta a_\mu^{\text{HVP}}$ is calculated by first computing the finite-volume correction for the correlator, $\Delta G(x_0)$, and then inserting that into Eq. 7.17,

$$\Delta a_\mu^{\text{HVP}} = \left(\frac{\alpha}{\pi}\right)^2 \int_0^\infty dx_0 \, \Delta G(x_0) \tilde{K}(x_0; m_\mu), \tag{7.30}$$

where $\Delta G(x_0) = -[G(x_0, L) - G(x_0, \infty)]$, and

$$G(x_0, L) - G(x_0, \infty) = \frac{1}{3}\left[\frac{1}{L^3}\sum_{\vec{k}} - \int \frac{d^3k}{(2\pi)^2}\right] \frac{\vec{k}^2}{\vec{k}^2 + m_\pi^2} e^{2x_0\sqrt{\vec{k}^2+m_\pi^2}} \tag{7.31}$$

$$= \frac{m_\pi^4 x_0}{3\pi^2} \sum_{\vec{n}\neq 0} \left\{ \frac{K_2\left(m_\pi\sqrt{L^2\vec{n}^2 + 4x_0^2}\right)}{m_\pi^2(L^2\vec{n}^2 + 4x_0^2)} - \frac{1}{m_\pi L|\vec{n}|}\int_1^\infty dy K_0\left(m_\pi y\sqrt{L^2\vec{n}^2 + 4x_0^2}\right)\sinh(m_\pi L|\vec{n}|(y-1))\right\}, \tag{7.32}$$

where K_0 and K_2 are the modified Bessel functions of the second kind, m_π is the pion mass, and L is the spatial lattice extent.

The two different forms (Eq. 7.31 and Eq. 7.32) are useful as the sums and integrals converge at different rates for high and low values of x_0. We compute $\Delta G(x_0)$ separately for $x_0 < x_0^i$ and $x_0 \geq x_0^i$, for $x_0^i = \left(\frac{m_\pi L}{4}\right)^2 / m_\pi$, where we use Eq. 7.32 for $x_0 < x_0^i$ and Eq. 7.31 for $x_0 \geq x_0^i$.

As we calculate $a_\mu^{\text{HVP,LO}}$ independently for each quark flavour, we need to calculate the finite-volume corrections for each quark flavour on each ensemble too. In order to achieve this, we replace the pion mass m_π in Eq. 7.31 and Eq. 7.32 with the pseudoscalar meson mass m_{fg}, determined using the valence quark of interest, f, and each sea quark flavour, g, (see Figure 7.13) and sum the contribution for each sea quark,

$$\Delta G^{valence=f}(x_0) = \sum_{g=u,d,s} \Delta G^{valence=f}_{sea=g}(x_0, m_{fg}). \tag{7.33}$$

Note that despite only π^+ and K^+ states occurring in the full physical result, we must include effects due to all possible valence-sea meson states as we are only considering the connected part of the correlation function. When including the disconnected terms the non-physical states will be removed, but the purely connected contribution will still contain finite-volume effects due to these states.

Performing this finite-volume correction for the $a_\mu^{\text{HVP,LO}}$ values calculated on each valence quark mass/charge, we can repeat the flavour-breaking expansion from before, and combine the different quark flavour contributions to get a total value for the

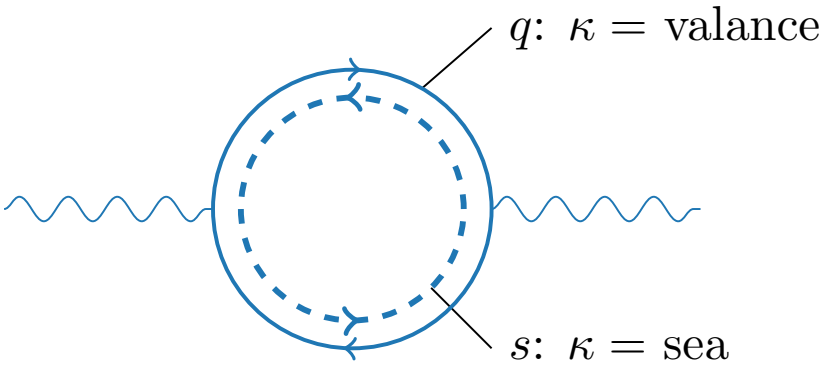

Figure 7.13. Diagram relevant for finite-volume effects of the vacuum polarisation loop, the leading order hadronic contribution to a_μ, showing a pseudoscalar meson (qs) forming between the valence (q) and sea (s) quarks within the $q\bar{q}$ loop.

Volume	Quark	$a_\mu^{\mathrm{HVP,LO},q}$
$32^3 \times 64$	Up	$8.98(27) \times 10^{-8}$
$32^3 \times 64$	Down	$9.35(23) \times 10^{-8}$
$32^3 \times 64$	Strange	$4.49(2) \times 10^{-8}$
$32^3 \times 64$	*Total*	$5.53(15) \times 10^{-8}$
$48^3 \times 96$	Up	$9.94(43) \times 10^{-8}$
$48^3 \times 96$	Down	$9.84(31) \times 10^{-8}$
$48^3 \times 96$	Strange	$4.69(2) \times 10^{-8}$
$48^3 \times 96$	*Total*	$6.03(23) \times 10^{-8}$

Table 7.7. $a_\mu^{\mathrm{HVP,LO}}$ contribution from each quark flavour, and the total value from the up, down and strange quarks with appropriate charge weighting, with finite-volume corrections applied.

leading order hadronic contribution for the anomalous magnetic moment of the muon. Individual values are shown in Figure 7.14.

The finite-volume corrected contribution to $a_\mu^{\mathrm{HVP,LO}}$ for each quark flavour at the physical quark mass is presented in Table 7.7, which combine to give a value of $a_\mu^{\mathrm{HVP,LO}} = 603(23) \times 10^{-10}$ for the $48^3 \times 96$ volume. A complete set of the finite-volume corrections applied to each valence quark mass/charge are listed for completeness in Table C.1.

Table 7.8 shows a selection of results for the connected contribution of $a_\mu^{\mathrm{HVP,LO}}$, using up, down and strange quarks, from other lattice studies for comparison with our results. The value of $a_\mu^{\mathrm{HVP,LO}}$ found in this work is slightly low compared to other studies.

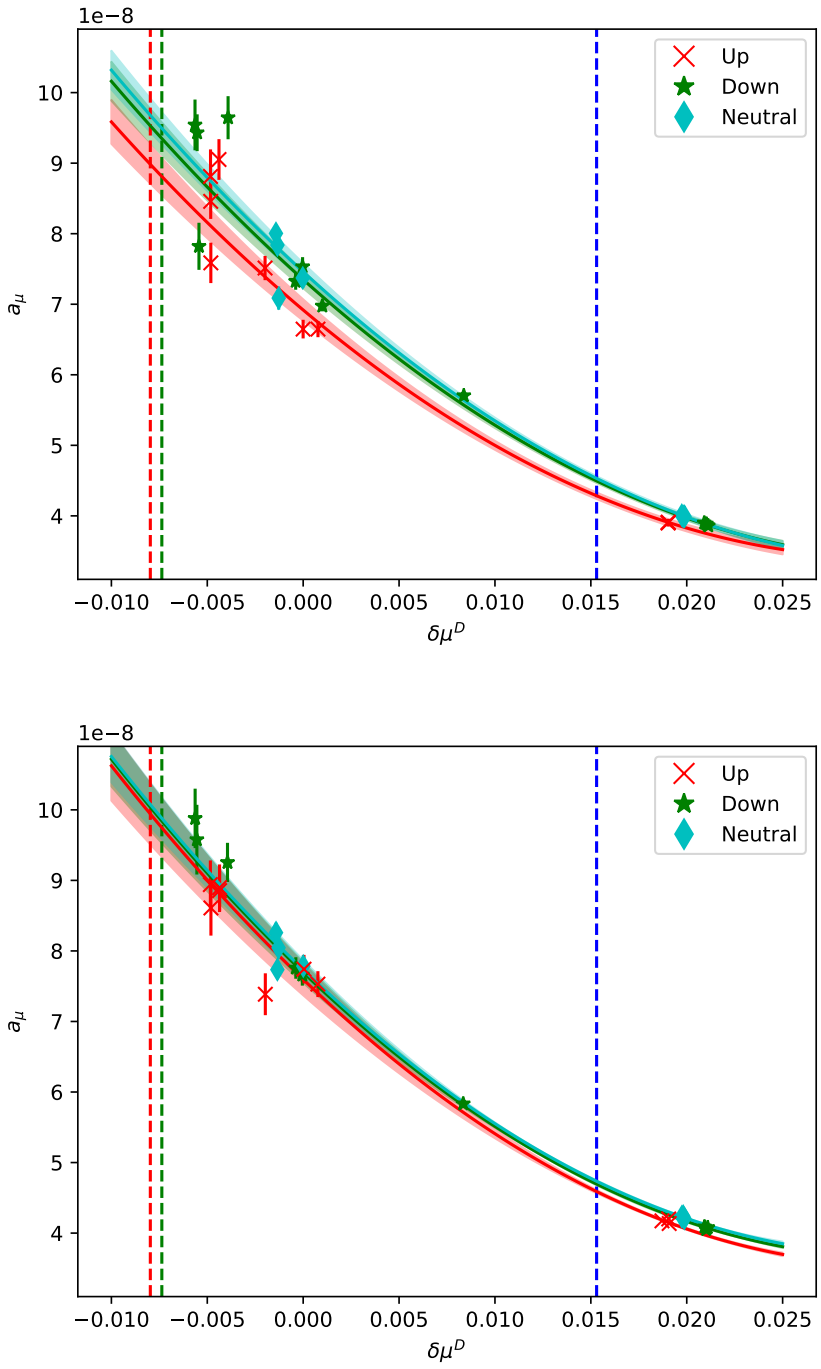

Figure 7.14. Flavour-breaking expansion for $a_\mu^{\mathrm{HVP,LO}}$ plotted as a function of the Dashen mass, as in Figure 7.12, with finite-volume corrections applied to each point. *Top*: $32^3 \times 64$ volume. *Bottom*: $48^3 \times 96$ volume. The red/green/blue vertical lines mark the location of the physical up/down/strange valence quark mass, while $\delta\mu^D = 0$ marks the SU(3) flavour-symmetric point.

Collaboration	$a_\mu^{\text{HVP,LO},u,d,s}$	Ref.
BMW	688.4(46)	[9]
RBC/UKQCD	702.9(15)	[58]
ETM	672.1(180)	[116, 117]
CLS/Mainz	728.5(132)	[62]
HPQCD/Fermilab/MILC	691.2(88)	[61]
PACS	725.1(142)	[60]
Lehner/Meyer	710(29)	[118]
This Study	603(23)	

Table 7.8. Comparison of lattice results for $a_\mu^{\text{HVP,LO}}$ from other studies including effects from up, down and strange quarks.

One possible explanation for the smaller value of $a_\mu^{\text{HVP,LO}}$ is from Section 6.4, where we have not fully included the $\mathcal{O}(a)$ improvements outlined in Eq. 6.7. Recall that the improvement coefficient c_ν is currently unknown on our gauge field configurations. As the main aim of this study is to investigate the QED corrections to the hadronic contribution, this discrepancy is not an issue, as we have shown this improvement term is expected to be charge independent.

It is also likely that there are still some finite-volume effects present. Refs. [60], [63] and [9] have shown that the Gounaris-Sakurai model for the $\pi\pi$ interaction provides a more accurate finite-volume correction than non-interacting pion model used here, and results in a larger finite-volume correction which could help resolve the remaining discrepance between the two volumes, as well as increase our final result to be more inline with other studies. This is a point of further investigation in future work.

Chapter 8.

QED Corrections to $a_\mu^{\text{HVP,LO}}$

In the previous chapter we described the flavour-breaking expansion of $a_\mu^{\text{HVP,LO}}$ as a function of the Dashen mass for quarks with a charge of $\frac{2}{3}e$, $-\frac{1}{3}e$, and 0. In Figure 7.12 we can see that there is some effect in the expansion due to the quark charge, but due to the uncertainties present it is impossible to determine from this alone any evidence of a contribution due to the quark charge. However, as these results are highly correlated, much of this uncertainty will be common between the quark charges, and by comparing the quark charges at the bootstrap level we are able to remove the correlated uncertainty and isolate the QED contribution.

In order to quantify this effect we compare the charged quark contributions to the contribution computed used the 'neutral quark' where we set the quark charge to 0. This is achieved by using our flavour breaking expansion from before in Section 7.2.2, and setting the quark charge terms to zero, *i.e.* removing the EM terms in Eq. 7.25.

We can now take the difference between the charged quark contribution $a_\mu^{u/d/s}$ and this neutral quark contribution a_μ^n at all values of the Dashen mass, $\delta\mu^D$, and normalise this to the neutral quark contribution,

$$a_{\mu,EM}^{u/d/s} = \frac{a_\mu^{u/d/s} - a_\mu^n}{a_\mu^n}. \tag{8.1}$$

This will leave us with the QED contribution, as a proportion of the pure QCD contribution. This is shown in Figure 8.1 as a function of the Dashen scheme mass, $\delta\mu^D$, which shows a small but statistically significant non-zero contribution.

It should be pointed out here once again, as explained in Section 5.2.2, that we are using a QED coupling α^{QED} ten times the physical value, which exaggerates any QED

effects by a factor of ten. For simplicity all the results quoted here already have this effect taken into account. At this scale, any QED terms scale linearly in e^2 [84], this is simply done by dividing the result by 10.

Reading off the effect at the physical quark masses, we find in the Dashen scheme the results from the $48^3 \times 96$ volume show an effect of $a^u_{\mu,EM} = 0.24\% \pm 0.13\%$, $a^d_{\mu,EM} = 0.05\% \pm 0.02\%$ and $a^s_{\mu,EM} = 0.08\% \pm 0.01\%$.

In order to calculate the total QED contribution to the hadronic contribution of the anomalous magnetic moment of the muon, we can combine the separate quark contributions as in Eq. 7.26 using the results from the charged quarks as before, and compare that with the pure QCD contribution, which we obtain from the 'neutral quark' fit shown in Figure 7.12 taken at the physical quark masses:

$$a^{\text{HVP,LO}}_{\mu,\text{charged}} = \frac{4}{9}a^u_\mu + \frac{1}{9}a^d_\mu + \frac{1}{9}a^s_\mu, \tag{8.2}$$

$$a^{\text{HVP,LO}}_{\mu,\text{neutral}} = \frac{4}{9}a^{u_0}_\mu + \frac{1}{9}a^{d_0}_\mu + \frac{1}{9}a^{s_0}_\mu, \tag{8.3}$$

where $a_\mu^{u_0/d_0/s_0}$ refer to the 'neutral quark' fit evaluated at the physical $u/d/s$ quark mass.

Taking the same normalised difference as in Eq. 8.1 for the total $a_\mu^{\text{HVP,LO}}$, we find the QED contribution to $a_\mu^{\text{HVP,LO}}$ to be $0.2\% \pm 0.1\%$. While this is a very small correction, it is also very significant. Current lattice results are now being quoted with errors around $1-2\%$ [57, 58, 60, 61, 63, 116], with recent results as low as 0.7% [9], and are currently targeting at least 0.5% precision. Correctly accounting for QED contributions of 0.2% will play a significant role in achieving this desired precision.

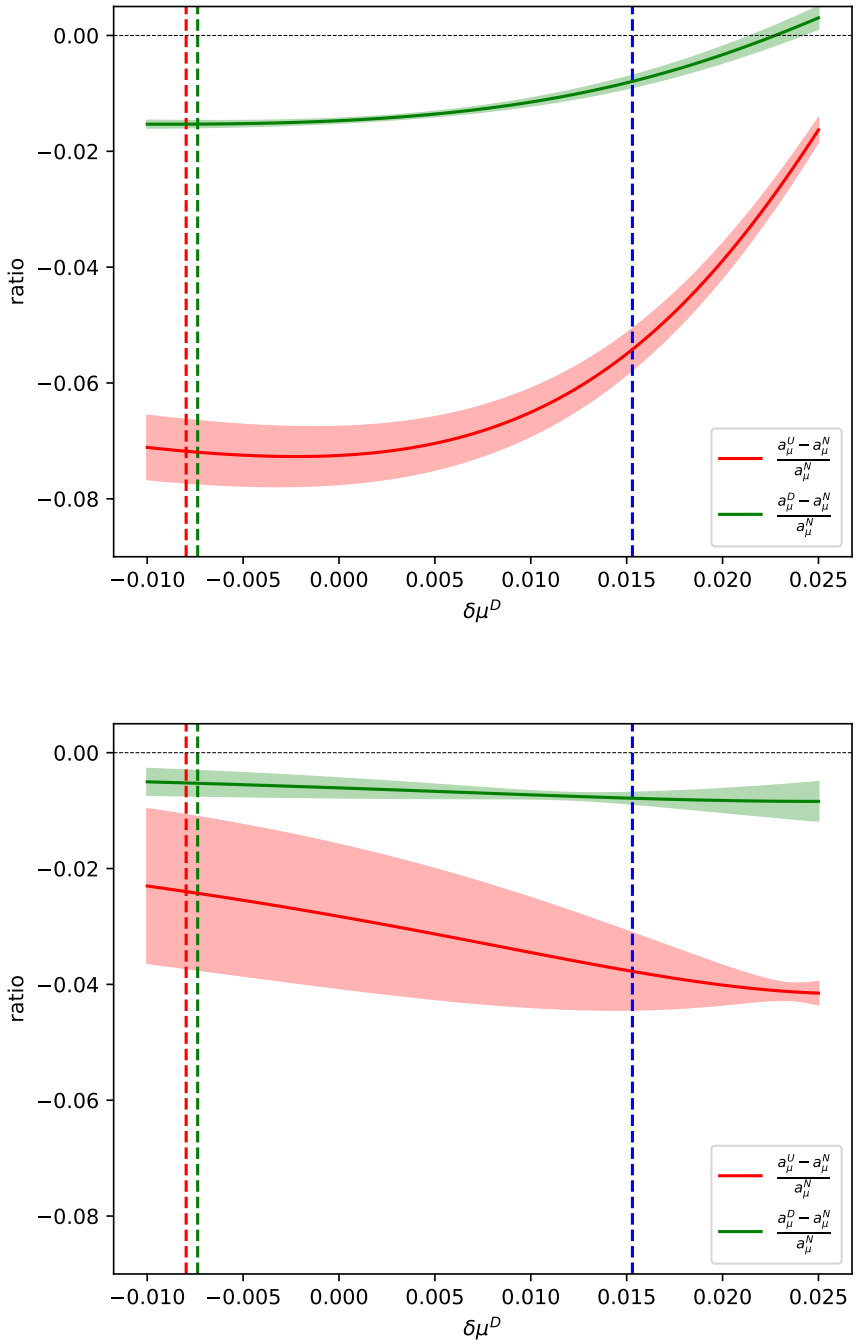

Figure 8.1. Deviation of charged quark contribution from the purely QCD contribution. *Top*: $32^3 \times 64$. *Bottom*: $48^3 \times 96$. As before, the vertical dashed lines mark the physical quark masses for up, down and strange quarks (left to right) in red, green and blue respectively.

Volume	Quark	$a_{\mu,EM}^{\text{HVP,LO},q}$
$32^3 \times 64$	Up	0.72(5)%
$32^3 \times 64$	Down	0.15(1)%
$32^3 \times 64$	Strange	0.08(1)%
$32^3 \times 64$	*Total*	0.64(5)%
$48^3 \times 96$	Up	0.2(1)%
$48^3 \times 96$	Down	0.05(2)%
$48^3 \times 96$	Strange	0.07(1)%
$48^3 \times 96$	*Total*	0.2(1)%

Table 8.1. Total QED contribution to $a_\mu^{\text{HVP,LO}}$ for each quark flavour, as well as the overall QED contribution to $a_\mu^{\text{HVP,LO}}$.

Chapter 9.

Disconnected Contributions

So far all the results presented in this thesis have only considered the quark connected contributions, and any disconnected contributions have been ignored. For a final study, we have performed an initial investigation into the disconnected contributions to the leading order hadronic contribution to the anomalous magnetic moment of the muon.

If the connected correlator can be thought of as a quark and antiquark pair travelling from some source x to some sink y, then the disconnected correlator is a quark starting and ending at x, while another starts and ends at y. In terms of the hadron vacuum polarisation, this is shown in Figure 9.1.

Recalling that for the vector current operator

$$J_\mu(x) = \frac{2}{3}\bar{u}(x)\gamma_\mu u(x) - \frac{1}{3}\bar{d}(x)\gamma_\mu d(x) - \frac{1}{3}\bar{s}(x)\gamma_\mu s(x) + ..., \tag{9.1}$$

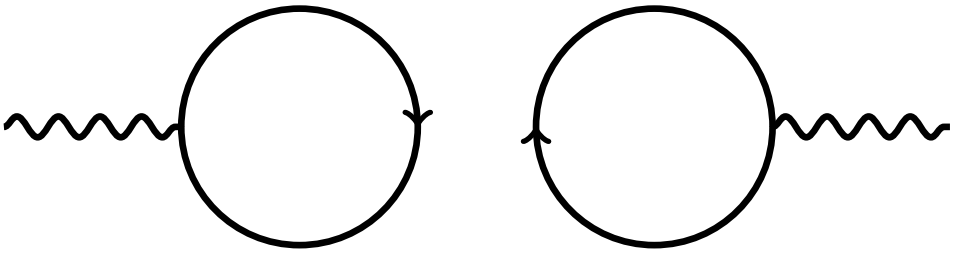

Figure 9.1. The leading order disconnected diagram which contributes to the hadron vacuum polarisation. Note that the interaction between the two quark loops via virtual photons and/or gluons are suppressed in this diagram for clarity, but are included in the full calculation.

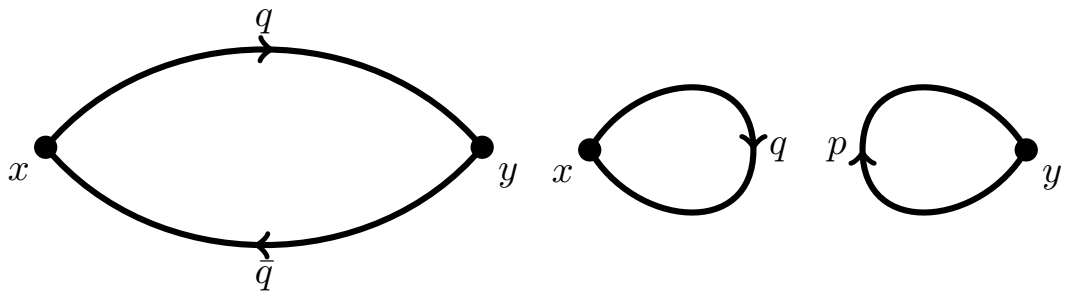

Figure 9.2. *Left*: Connected quark flow diagram $q\bar{q}_{conn}(x,y)$. *Right*: Disconnected quark flow diagram $pq_{dis}(x,y)$.

the correlation function $\langle J_k(x)J_k(y)\rangle$ can be written in terms of connected and disconnected contributions,

$$\begin{aligned}\langle J_k(x)J_k(y)\rangle =&\Bigg\langle \left(\frac{2}{3}\bar{u}(x)\gamma_k u(x) - \frac{1}{3}\bar{d}(x)\gamma_k d(x) - \frac{1}{3}\bar{s}(x)\gamma_k s(x)\right)\\ &\times\left(\frac{2}{3}\bar{u}(y)\gamma_k u(y) - \frac{1}{3}\bar{d}(y)\gamma_k d(y) - \frac{1}{3}\bar{s}(y)\gamma_k s(y)\right)\Bigg\rangle.,\end{aligned} \tag{9.2}$$

Here we will define some notation in order to simplify the expansion of the correlator and split it into the connected and disconnected contributions. The general form for a single element of $J_k(x)J_k(y)$ can be written as

$$Q_q\bar{q}(x)\gamma_k q(x)\, Q_p\bar{p}(y)\gamma_k p(y), \tag{9.3}$$

where Q_q is the charge of quark q. By performing Wick contractions on this we get

$$\begin{aligned}\overbrace{Q_q\bar{q}(x)\gamma_k q(x)\, Q_p\bar{p}(y)\gamma_k p(y)} =&Q_qQ_p\,\mathrm{Tr}\left[S^\dagger_{pq}(x,y)\gamma_k S_{pq}(x,y)\gamma_k\right]\delta_{pq}\\ &+Q_qQ_p\,\mathrm{Tr}\left[S_{pp}(y,y)\gamma_k\right]\mathrm{Tr}\left[S_{qq}(x,x)\gamma_k\right],\\ =&Q_qQ_p q\bar{p}_{conn}(x,y)\delta_{pq} + Q_qQ_p pq_{dis}(x,y),\end{aligned} \tag{9.4}$$

where $q\bar{p}_{conn}(x,y)\delta_{pq} = \mathrm{Tr}\left[S^\dagger_{qq}(x,y)\gamma_k S_{qq}(x,y)\gamma_k\right]\delta_{pq}$ is the connected contribution, and $pq_{dis}(x,y) = \mathrm{Tr}\left[S_{pp}(y,y)\gamma_k\right]\mathrm{Tr}\left[S_{qq}(x,x)\gamma_k\right]$ is the disconnected contribution, as shown in Figure 9.2. Note that in the case where the quarks p and q are different flavours , δ_{pq} ensures that the connected contribution vanishes.

Using this notation, we are able to fully expand Eq. 9.2 as

$$\begin{aligned}\langle J_k(x)J_k(y)\rangle = & \left\langle \left(\frac{2}{3}\bar{u}(x)\gamma_k u(x) - \frac{1}{3}\bar{d}(x)\gamma_k d(x) - \frac{1}{3}\bar{s}(x)\gamma_k s(x)\right)\right. \\ & \left.\times\left(\frac{2}{3}\bar{u}(y)\gamma_k u(y) - \frac{1}{3}\bar{d}(y)\gamma_k d(y) - \frac{1}{3}\bar{s}(y)\gamma_k s(y)\right)\right\rangle \\ = & \left\langle \frac{4}{9}u\bar{u}_{conn}(x,y) + \frac{1}{9}d\bar{d}_{conn}(x,y) + \frac{1}{9}s\bar{s}_{conn}(x,y)\right. \\ & +\frac{4}{9}uu_{dis}(x,y) - \frac{2}{9}ud_{dis}(x,y) - \frac{2}{9}us_{dis}(x,y) \\ & -\frac{2}{9}du_{dis}(x,y) + \frac{1}{9}dd_{dis}(x,y) + \frac{1}{9}ds_{dis}(x,y) \\ & \left.-\frac{2}{9}su_{dis}(x,y) + \frac{1}{9}sd_{dis}(x,y) + \frac{1}{9}ss_{dis}(x,y)\right\rangle. \end{aligned} \tag{9.5}$$

We can see the three familiar connected terms which we have discussed in Chapters 7 and 8, and the nine disconnected terms which include flavour-diagonal and off-diagonal contributions.

9.1. Lattice Methods

As we have discussed earlier in Section 5.1.1, when computing the connected propagator we restricted ourselves to a single source location, $x = 0$, in order to reduce the computational complexity, and compute the connected propagator as a point-to-all propagator. This is effective as a point-to-all propagator only takes a single inversion of the fermion matrix. In the case of the disconnected correlator, we require propagators which loop back on themselves, known as self-to-self or loop propagators. Because of this, we are required to invert the fermion matrix at all source locations in order to Fourier project the source, and compute the all-to-all propagator, from which we can extract the self-to-self propagator, effectively increasing the complexity by a factor of the lattice volume. This would result in the disconnected correlator being prohibitively computationally expensive.

In order to compute the disconnected contribution exactaly we are required to invert the fermion matrix at every lattice site, which requires an increase of $N_s^3 \times N_t$ times

the number of inversions compared with the point-to-all propagator we have used for the connected contribution.

We attempt to solve this by introducing stochastic noise sources which we invert the fermion matrix against in order to approximate the propagator, following the methods laid out in [119, 120]. We do this by using an ensemble of N_r noise sources generated using $\mathbb{Z}_2$ noise, $[\eta_{[r]}(x)]^a_\alpha \in \{-1, 1\}$ where a and α are colour and Dirac indices (see Table 2.1), which exhibit the the property

$$\lim_{N_r\to\infty} \frac{1}{N_r} \sum_{r=1}^{N_r} [\eta_{[r]}(x)]^a_\alpha \, [\eta_{[r]}(y)]^{\dagger\, b}_\beta = \delta^{ab}\delta_{\alpha\beta}\delta_{xy}. \tag{9.6}$$

N_r is chosen such that the introduced stochastic noise is negligible when compared with the gauge noise. We obtain the solution vectors $[\psi_{[r]}(y)]^b_\beta$ from the inversion of the fermion matrix against the noise vector,

$$[M(z,y)]^{cb}_{\gamma\beta} \, [\psi_{[r]}(y)]^b_\beta = [\eta_{[r]}(z)]^c_\gamma, \tag{9.7}$$

such that

$$[\psi_{[r]}(y)]^b_\beta = [M^{-1}(y,z)]^{bc}_{\beta\gamma} \, [\eta_{[r]}(z)]^c_\gamma. \tag{9.8}$$

Using the identity in Eq. 9.6, we can write the propagator in terms of the solution vectors $[\psi_{[r]}(y)]^b_\beta$:

$$\begin{aligned}
[S(y,x)]^{ba}_{\beta\alpha} &= \lim_{N_r\to\infty} \frac{1}{N_r} \sum_{r=1}^{N_r} [\psi_{[r]}(y)]^b_\beta \, [\eta^\dagger_{[r]}(x)]^a_\alpha, \\
&= \lim_{N_r\to\infty} \frac{1}{N_r} \sum_{r=1}^{N_r} [M^{-1}(y,z)]^{bc}_{\beta\gamma} \, [\eta_{[r]}(z)]^c_\gamma \, [\eta^\dagger_{[r]}(x)]^a_\alpha, \\
&= [M^{-1}(y,z)]^{bc}_{\beta\gamma} \, \delta^{ac} \, \delta_{\alpha\gamma} \, \delta_{zx}, \\
&= [M^{-1}(y,x)]^{ba}_{\beta\alpha}.
\end{aligned} \tag{9.9}$$

This is the basis of computing an estimate of the all-to-all propagator using noise sources. In order to recover the exact propagator, we require infinitely many noise sources to fully cancel the $\mathcal{O}(1)$ noise, however in practice, even with a very limited number of noise sources we are able to achieve a suitably precise estimate of the prop-

agator [121], as we only require that the estimate is more precise than the existing gauge noise.

9.1.1. Wall-source dilution

One improvement we can make to the stochastic estimate of the propagator is to dilute our noise source in time, spin and colour such that we can write the noise source as

$$\eta_{[r]}(x) = \sum_{i=1}^{N_d} \eta^i_{[r]}(\vec{x}, t), \tag{9.10}$$

where $N_d = N_t \times N_c \times N_s$, and only one term in the sum is non-zero for each unique combination of time, spin and colour. We can represent this pictorially as

$$\begin{pmatrix} \eta_1 \\ \eta_2 \\ \eta_3 \\ \vdots \end{pmatrix} = \begin{pmatrix} \eta_1 \\ 0 \\ 0 \\ \vdots \end{pmatrix} + \begin{pmatrix} 0 \\ \eta_2 \\ 0 \\ \vdots \end{pmatrix} + \begin{pmatrix} 0 \\ 0 \\ \eta_3 \\ \vdots \end{pmatrix} + \dots, \tag{9.11}$$

where the column vectors in the sum on the right-hand side are the individual $\eta^i_{[r]}(\vec{x}, t)$. This method will require N_d more inversions than if we performed no such dilution, however it has been seen that noise is reduced faster via the use of dilution than by simply introducing additional stochastic noise sources [119].

Spatial interlacing

If one was to introduce full spatial dilution in addition to the time, spin and colour dilution described above, we would effectively be inverting against a point source at every single lattice site, and compute the full all-to-all propagator. As already mentioned, this is prohibitively expensive, so we introduce an alternative approach to introduce a form of spatial dilution. The method used in this work is known as interlacing, whereby the full spatial volume is split into several subsets, X_i, which have no overlap and return the full spatial volume in their union. The noise vector can then be written in terms of

these subsets as (making the spin and colour dilution explicit, at a specific time)

$$[\eta^i_{[r]}(\vec{x}, t_0)]^{aa'}_{\alpha\alpha'} = \zeta_{[r]}(\vec{x})\delta_{aa'}\delta_{\alpha\alpha'}\delta_{\vec{x}\in X_i}, \tag{9.12}$$

where $\zeta_{[r]}(\vec{x})$ is a spatial $\mathbb{Z}_2$ noise vector, and $\delta_{\vec{x}\in X_i} = 1$ if $\vec{x} \in X_i$, and zero otherwise. The propagator can then be computed in the usual way for each dilution element of the noise vector, and summed to construct the full approximation of the all-to-all propagator.

In this work we have chosen to include 8 subsets X_i over which to perform the spatial interlacing. The subsets X_i are constructed by first creating a mask which selects every second point in each spatial direction, and then shifting that mask in all combinations of either zero or one step in each spatial direction. This creates eight distinct masks, each centred on locations: $(0,0,0)$, $(1,0,0)$, $(0,1,0)$, $(0,0,1)$, $(1,1,0)$, $(1,0,1)$, $(0,1,1)$, $(1,1,1)$.

This is shown pictorially in two-dimensions in Figure 9.3.

9.2. Results

In this exploratory study we have only considered a single ensemble at the SU(3)-symmetric point, with a volume of $24^3 \times 48$. As such, we have degenerate down and strange quarks and a distinct up quark, and hence are in the U-spin limit (in contrast with the isospin limit, where we have up-down degeneracy). Due to this down-strange degeneracy, the disconnected contributions in Eq. 9.5 can be further simplified to

$$\begin{aligned}\langle J_k(x)J_k(y)\rangle_{dis} = &\ \frac{4}{9}uu_{dis}(x,y) - \frac{2}{9}ud_{dis}(x,y) - \frac{2}{9}ud_{dis}(x,y) \\ &-\frac{2}{9}du_{dis}(x,y) + \frac{1}{9}dd_{dis}(x,y) + \frac{1}{9}dd_{dis}(x,y) \\ &-\frac{2}{9}du_{dis}(x,y) + \frac{1}{9}dd_{dis}(x,y) + \frac{1}{9}dd_{dis}(x,y) \qquad (9.13)\\ = &\ \frac{4}{9}uu_{dis}(x,y) - \frac{4}{9}ud_{dis}(x,y) - \frac{4}{9}du_{dis}(x,y) \\ &+\frac{4}{9}dd_{dis}(x,y). \qquad (9.14)\end{aligned}$$

In the case of pure QCD, this term is equal to zero at the SU(3)-symmetric point as the quark masses are all the same and so the up and down quarks will become

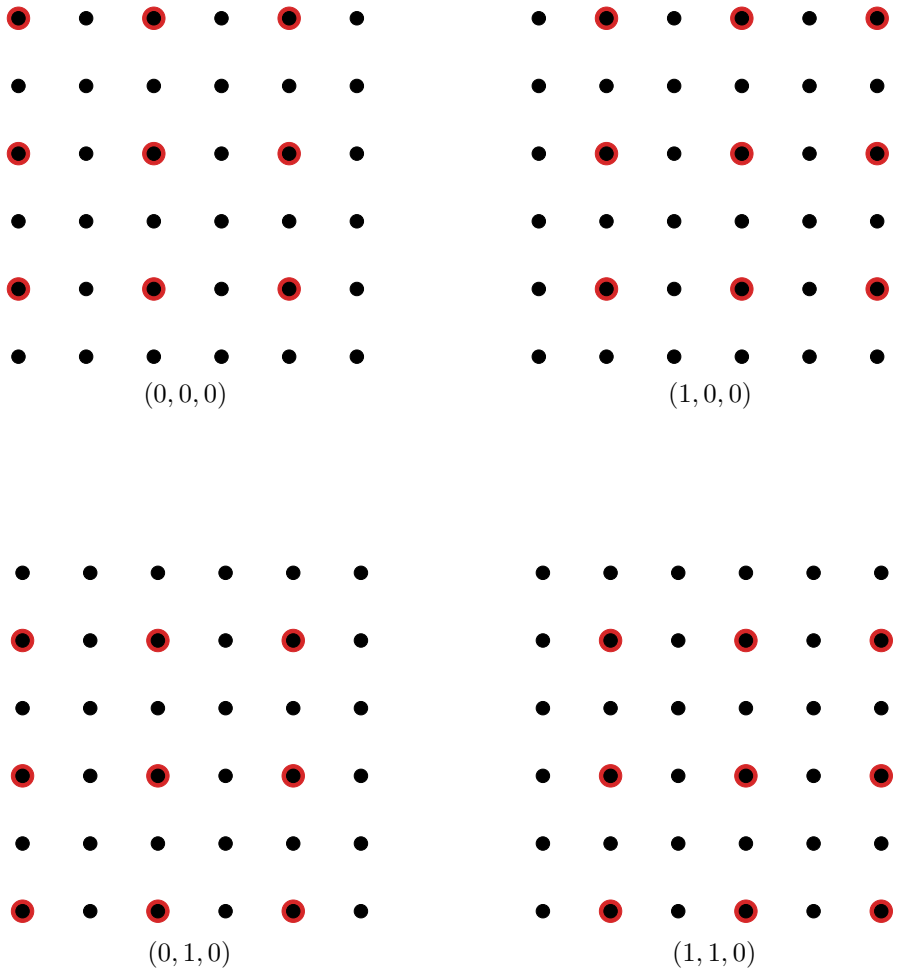

Figure 9.3. Two-dimensional representation of the interlacing, with masked spatial points marked with the red outline. Interlacing mask centred at marked spatial location. In the full three-dimensional space these four masks will be duplicated with a unit shift in the third dimension.

degenerate. In the case where QED is included, however, even when their masses have been tuned to be the same, as is roughly the case here, the up and down quarks are distinguished by electric charge. This means that any non-zero result in Eq. 9.14 at the SU(3)-symmetric point is due to QED contributions.

In order to isolate the disconnected effects, we are able to compare the results for the full correlator (*i.e.* with both the connected and disconnected correlators included), with results from just the connected correlator. As we expect the disconnected correlator to be small [62] relative to the connected correlator, we can compute a value for a_μ^{HVP} using the time-momentum method laid out in Section 7.2 for both the full correlator and the purely connected correlator, and by taking the difference we find the result due to the disconnected contributions:

$$a_{\mu,dis}^{\text{HVP}} = a_{\mu,con+dis}^{\text{HVP}} - a_{\mu,con}^{\text{HVP}}. \tag{9.15}$$

By performing this subtraction at the bootstrap level, any uncertainty due to the connected part should be highly correlated and removed.

Computing the disconnected contribution in this manner, rather than performing the analysis directly on the purely disconnected correlator, has two major advantages. Firstly, it makes the analysis identical to the purely connected case, which provides us with confidence in the methodology and lowers the chance of mistakes in the analysis. Secondly, as the effect we are seeking is expected to be small, this can lead to instability in the fitting process due to the relatively large uncertainties. By using the full correlator, we have a smaller relative uncertainty which leads to the fitting process being much more stable and reliable. As mentioned above, by performing the subtraction at the bootstrap level, we remove any noise due to the purely connected part.

As before when considering only the connected contribution, we must be careful when selecting the fit window for the tail of the correlator so as not to introduce any systematic errors. In Figure 9.4 we have considered a range of fit windows with the start time ranging from 10 to 15, and the end of the window ranging from time 15 to 18.

The small magnitude of the disconnected contribution leads to a dependence on the choice of fit window. In order to avoid the introduction of any systematic effects to our result, we combine results from all the windows using a weighting which combines the χ^2, window size and uncertainty from each window. The method used is defined in Ref. [122].

For a set of N fit windows, we obtain the central value and statistical uncertainty squared by simply taking a weighted average of each fit result and statistical uncertainty squared,

$$\bar{a}_\mu = \sum_{f=1}^{N} w^f a_\mu^f, \tag{9.16}$$

$$\delta_{\text{stat}}\bar{a}_\mu^2 = \sum_{f=1}^{N} w^f \left(\delta a_\mu^f\right)^2, \tag{9.17}$$

for some weighting w^f, where f labels the fit window. The systematic error introduced by the weighting can be expressed as

$$\delta_{\text{sys}}\bar{a}_\mu^2 = \sum_{f=1}^{N} w^f \left(a_\mu^f - \bar{a}_\mu\right)^2, \tag{9.18}$$

and the total uncertainty can then be found by adding these two uncertainties in quadrature,

$$\delta\bar{a}_\mu = \sqrt{\delta_{\text{stat}}\bar{a}_\mu^2 + \delta_{\text{sys}}\bar{a}_\mu^2}. \tag{9.19}$$

The weights w_f are determined in such a way as to penalise fits with large χ^2/dof or a large statistical uncertainty, δa_μ^f. To achieve this we use the weights

$$w^f = \frac{p^f \left(\delta a_\mu^f\right)^{-2}}{\sum_{f'=1}^{N} p^{f'} \left(\delta a_\mu^{f'}\right)^{-2}}, \tag{9.20}$$

where $p^f = \Gamma(N_{dof}/2, \chi_f^2/2)/\Gamma(N_{dof}/2)$, and $\Gamma(x, y)$ is the upper incomplete gamma function, and $\Gamma(x)$ is the regular gamma function.

The weighted average leads to a disconnected contribution at the SU(3) symmetric point of $-0.7(14) \times 10^{-11}$. While this result is consistent with zero, it also has a strong negative bias. We are unable to draw a strong conclusion from this data about the magnitude of the QED effects on the disconnected contribution from this, however it does suggest that the method used is able to resolve disconnected effects.

As an exploratory calculation, we can compare the central value of the QED correction to the disconnected values found by other lattice studies using pure QCD results. In order to do this we will assume that the QED correction is independent of quark

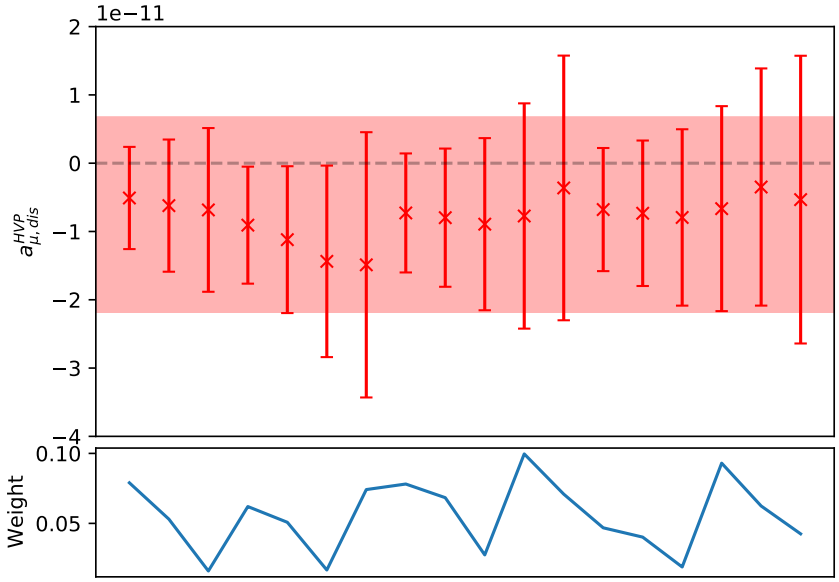

Figure 9.4. Disconnected QCD contribution over multiple fit windows, shown by the red points. The shaded region indicates the weighted average over the windows. The bottom plot shows the weighting used for each window.

Collaboration	$a_{\mu,disc}^{\text{HVP,LO}}$	Ref.
BMW	$-13.15(182) \times 10^{-10}$	[9]
RBC/UKQCD	$-11.2(40) \times 10^{-10}$	[58]
CLS/Mainz	$-23.2(50) \times 10^{-10}$	[62]

Table 9.1. Disconnected contribution to a_{μ}^{HVP} from other lattice studies

mass. While this is not strictly true, Figure 8.1 shows us that the mass dependence of the QED correction in the connected contributions are relatively small. Table 9.1 lists results for the disconnected contribution from several groups, which give an average disconnected contribution of $a_{\mu,disc}^{\text{HVP,LO}} = -15.8(2) \times 10^{-10}$ [5]. Taking the ratio of the QED correction and the QCD disconnected contribution, we estimate the QED correction to be $\mathcal{O}(0.5\%)$, which is in agreement with the QED corrections found in Table 8.1 for the connected contribution.

This result serves as a first step in our analysis of the QED effects to the disconnected contribution, and indicates that this line of enquiry should be pursued in future work.

Chapter 10.

Conclusion

With the first results from Fermilab's E989 experiment for the anomalous magnetic moment of the muon expected very soon, this is a very exciting time for $g-2$ studies. Improvements to the SM calculation will be key in taking advantage of the new experimental results, and resolving the standing 3.7σ discrepancy.

This thesis presents a detailed overview of the work performed to calculate the leading order hadronic contribution of the anomalous magnetic moment of the muon, focusing on the QED corrections to this contribution, using lattice gauge theories.

Chapter 2 provided a overview of the theories of QED and QCD, which served as a basis for Chapter 3, where we discussed the current state of research into the anomalous magnetic moment of the muon, first looking at the experimental results and methods used to measure a_μ, and then going though the current state of the SM calculation. Here we justified why we focus our efforts on the hadronic contribution using lattice methods, and particularly focusing our investigation on the small QED corrections to this contribution.

We then followed this with a summary of how we formulate our theory onto the lattice, and are able to use this to calculate expectation values of operators. This also included a discussion of the various lattice systematics. We also looked at calculating the vector current renormalisation, which allows us to use the local vector current at the source and reduce the computational cost of the calculation.

In Chapter 7 we presented the method used to compute $a_\mu^{\text{HVP,LO}}$ on the lattice using two methods: The hadronic vacuum polarisation tensor approach and the time-momentum representation.

Using the hadronic vacuum polarisation tensor approach, we found there exist substantial finite-volume effects in the small, $32^3 \times 64$ volume. The larger, $48^3 \times 96$ volume has smaller finite-volume effects, but they are still not fully under control and we must be careful to correct for them.

Using the time-momentum representation, we were able to extract a result for the leading order hadronic contribution of $a_\mu^{\text{HVP,LO}} = 603(23) \times 10^{-10}$ on the $48^3 \times 96$ volume. Comparing with other lattice results for up, down and strange quarks, which range from $\approx 670 - 730 \times 10^{-10}$(See Table 7.8), our result appears to be a little low. We propose two possible causes for this. The first is that we are unable to fully include the $\mathcal{O}(a)$ improvements, because the improvement coefficient c_ν is currently unknown on our gauge field configurations. While this may affect our calculated value for $a_\mu^{\text{HVP,LO}}$, we have shown that this term is unlikely to have any effect on the QED contributions, and so this is not a major concern. The other possible cause is an incomplete finite-volume correction. While the finite-volume correction applied has reduced the disagreement between the two lattice volumes we have used in this study, there still remains a discrepancy between these results. Further investigation of the finite-volume effects should be performed in future work.

In Chapter 8 we looked at extracting the QED corrections, and found that QED corrections contributed at $0.2(1)\%$. While relatively small, this correction is becoming increasingly important as we move to higher and higher precision calculations. Current lattice targets aim for a precision of greater than 0.5%, so QED corrections will fast become the dominant uncertainty if not correctly accounted for. This makes it crucial that we have a complete understanding of the QED corrections.

Finally, in Chapter 9 we present an initial investigation into the disconnected contribution including all QCD+QED terms. At the SU(3) symmetric point we found the disconnected contribution to have a value of $-0.7(14) \times 10^{-11}$. While consistent with zero, this result is strongly skewed negative which requires further research to reduce the uncertainty, and investigate the size of QED corrections to the disconnected term away from the SU(3) symmetric point. As an exploratory calculation we compare the central value of the QED correction we find for the disconnected contribution, with the pure QCD contribution calculated in other lattice studies. In this way we estimate the QED correction to be $\mathcal{O}(0.5\%)$, which is comparable with the size of the QED correction found for the connected term.

Appendix A.

Gamma Matrices

The following appendix draws from Ref. [123].

A.1. Pauli Matrices

The Pauli spin-matrices are

$$\sigma_1 = \begin{pmatrix} 0 & 1 \\ 1 & 0 \end{pmatrix}, \sigma_2 = \begin{pmatrix} 0 & -i \\ i & 0 \end{pmatrix}, \sigma_3 = \begin{pmatrix} 1 & 0 \\ 0 & -1 \end{pmatrix}, \tag{A.1}$$

which satisfy the identity

$$\sigma_j \sigma_k = \delta_{jk} + i\epsilon_{jkl}\sigma_l. \tag{A.2}$$

The Pauli matrices are often written as $\vec{\sigma} = \sigma_{1,2,3}$.

A.2. Gamma Matrices

The gamma matrices satisfy the anti-commutator relation

$$\{\gamma_\mu, \gamma_\nu\} = 2\delta_{\mu\nu}. \tag{A.3}$$

We can write the gamma matrices in terms of the Identity and Pauli matrices. Using the $2\otimes 2$ block notation, the gamma matrices can be written in the Dirac representation as

$$\gamma^0 = \begin{pmatrix} \mathbb{I} & 0 \\ 0 & -\mathbb{I} \end{pmatrix}, \vec{\gamma} = \begin{pmatrix} 0 & \vec{\sigma} \\ -\vec{\sigma} & 0 \end{pmatrix}, \gamma_5 = i\gamma_1\gamma_2\gamma_3\gamma^0 = \gamma_5^\dagger = \begin{pmatrix} 0 & \mathbb{I} \\ \mathbb{I} & 0 \end{pmatrix}. \tag{A.4}$$

An example of a Euclidean representation is the Pauli representation, also known as the Sakurai representation. In a Euclidean representation the gamma matrices are Hermitian. In the Pauli representation they are written as

$$\gamma_4 = \begin{pmatrix} \mathbb{I} & 0 \\ 0 & -\mathbb{I} \end{pmatrix}, \vec{\gamma} = \begin{pmatrix} 0 & -i\vec{\sigma} \\ i\vec{\sigma} & 0 \end{pmatrix}, \gamma_5 = \gamma_1\gamma_2\gamma_3\gamma_4 = \gamma_5^\dagger = -\begin{pmatrix} 0 & \mathbb{I} \\ \mathbb{I} & 0 \end{pmatrix}. \tag{A.5}$$

A.3. Gell-Mann matrices

The eight 3×3 Gell-Mann matrices are [124]

$$\begin{aligned} t_1 &= \begin{pmatrix} 0 & 1 & 0 \\ 1 & 0 & 0 \\ 0 & 0 & 0 \end{pmatrix} \quad t_2 = \begin{pmatrix} 0 & -1 & 0 \\ 1 & 0 & 0 \\ 0 & 0 & 0 \end{pmatrix} \quad t_3 = \begin{pmatrix} 1 & 0 & 0 \\ 0 & -1 & 0 \\ 0 & 0 & 0 \end{pmatrix} \\ t_4 &= \begin{pmatrix} 0 & 0 & 1 \\ 0 & 0 & 0 \\ 1 & 0 & 0 \end{pmatrix} \quad t_5 = \begin{pmatrix} 0 & 0 & -1 \\ 0 & 0 & 0 \\ 1 & 0 & 0 \end{pmatrix} \quad t_6 = \begin{pmatrix} 0 & 0 & 0 \\ 0 & 0 & 1 \\ 0 & 1 & 0 \end{pmatrix} \\ t_7 &= \begin{pmatrix} 0 & 0 & 0 \\ 0 & 0 & -1 \\ 0 & 1 & 0 \end{pmatrix} \quad t_8 = \begin{pmatrix} \frac{1}{\sqrt{3}} & 0 & 0 \\ 0 & \frac{1}{\sqrt{3}} & 0 \\ 0 & 0 & \frac{-2}{\sqrt{3}} \end{pmatrix} \end{aligned} \tag{A.6}$$

Appendix B.

Lattice Appendix

B.1. The Plaquette

The plaquette is written as

$$P_{\mu\nu}(x) = U_\mu(x)U_\nu(x+a\hat{\mu})U_\mu^\dagger(x+a\hat{\nu})U_\nu^\dagger(x). \tag{B.1}$$

We can expand each term as

$$U_\nu(x+a\hat{\mu}) = \exp(-igaA_\nu(x+a\hat{\mu})). \tag{B.2}$$

By applying the Baker-Campbell-Hausdorff identity [125]

$$\exp(A)\exp(B) = \exp(A+B+\frac{1}{2}[A,B]+...), \tag{B.3}$$

to Eq. B.1, and using the expansion of each term, we can write the plaquette as

$$\begin{aligned} P_{\mu\nu}(x) = \exp\big(& -igaA_\mu(x) - igaA_\nu(x+a\hat{\mu}) - \frac{1}{2}g^2a^2[A_\mu(x), A_\nu(x+a\hat{\mu})] \\ & + igaA_\mu(x+a\hat{\nu}) + igaA_\nu(x) - \frac{1}{2}g^2a^2[A_\mu(x+\hat{\nu}), A_\nu(x)] \\ & + \frac{1}{2}g^2a^2[A_\mu(x), A_\mu(x+a\hat{\nu})] + \frac{1}{2}g^2a^2[A_\mu(x), A_\nu(x)] \\ & + \frac{1}{2}g^2a^2[A_\nu(x+a\hat{\mu}), A_\mu(x+a\hat{\nu})] + \frac{1}{2}g^2a^2[A_\nu(x+a\hat{\mu}), A_\nu(x)] + \mathcal{O}(a^3)\big). \end{aligned} \tag{B.4}$$

We can now perform a Taylor expansion on the gauge fields with shifted arguments, *ie.* $A_\nu(x + a\hat{\mu})$,

$$A_\nu(x + a\hat{\mu}) = A_\nu(x) + a\partial_\mu A_\nu(x) + \mathcal{O}(a^2). \tag{B.5}$$

We will first consider the non-commutator terms of Eq. B.4

$$\begin{aligned} &-igaA_\mu(x) - igaA_\nu(x + a\hat{\mu}) + igaA_\mu(x + a\hat{\nu}) + igaA_\nu(x) \\ &\quad = iga(-A_\mu(x) - A_\nu(x) - a\partial_\mu A_\nu(x) + A_\mu(x) + a\partial_\nu A_\mu(x) + A_\nu(x) + \mathcal{O}(a^2) \\ &\quad = iga^2(\partial_\nu A_\mu(x) - \partial_\mu A_\nu(x)) + \mathcal{O}(a^3). \end{aligned} \tag{B.6}$$

The commutators with shifted gauge fields in Eq. B.4 can be written as

$$\begin{aligned} [A_\mu(x), A_\nu(x + a\hat{\mu})] &= [A_\mu(x), A_\nu(x)] + a[A_\mu(x), \partial_\mu A_\nu(x)] + \mathcal{O}\left(a^2\right) \\ [A_\mu(x + a\hat{\nu}), A_\nu(x)] &= [A_\mu(x), A_\nu(x)] + a[\partial\nu A_\mu(x), A_\nu(x)] + \mathcal{O}\left(a^2\right) \\ [A_\mu(x), A_\mu(x + a\hat{\nu})] &= [A_\mu(x), A_\mu(x)] + a[A_\mu(x), \partial_\nu A_\mu(x)] + \mathcal{O}\left(a^2\right) \\ [A_\nu(x + a\hat{\mu}), A_\mu(x + a\hat{\nu})] &= [A_\nu(x), A_\mu(x)] + a[\partial_\mu A_\nu(x), A_\mu(x)] + a[A_\nu(x), \partial_\nu A_\mu(x)] + \mathcal{O}\left(a^2\right) \\ [A_\nu(x + a\hat{\mu}), A_\nu(x)] &= [A_\nu(x), A_\nu(x)] + a[\partial_\mu A_\nu(x), A_\nu(x)] + \mathcal{O}\left(a^2\right). \end{aligned} \tag{B.7}$$

We can now use the fact that A_μ, A_ν are Hermitian, and the definition of the field strength tensor

$$G_{\mu\nu}(x) = \partial_\mu A_\nu(x) - \partial_\nu A_\mu(x) + ig[A_\mu(x), A_\nu(x)], \tag{B.8}$$

we can substitute these terms back into the plaquette

$$\begin{aligned} P_{\mu\nu}(x) &= \exp\Big(- iga^2\big(\partial_\mu A_\nu(x) - \partial_\nu A_\mu(x)\big) + g^2a^2[A_\nu(x), A_\mu(x)] + \mathcal{O}\left(a^3\right)\Big) \\ &= \exp\Big(- iga^2\big(\partial_\mu A_\nu(x) - \partial_\nu A_\mu(x) - ig[A_\nu(x), A_\mu(x)]\big) + \mathcal{O}\left(a^3\right)\Big) \\ &= \exp\Big(iga^2 G_{\mu\nu}(x) + \mathcal{O}\left(a^3\right)\Big). \end{aligned} \tag{B.9}$$

B.2. Least squares fitting

In this thesis fits have been performed via a linear least squares minimisation procedure, using the routines provided by SciPy [126]. The χ^2 per degree of freedom (dof) is minimised using

$$\frac{\chi^2}{dof} = \frac{1}{n-m}\sum_{i=1}^{n}\sum_{j=1}^{n}\big(y(t_i) - T(t_i)\big)C^{-1}(t_i,t_j)\big(y(t_j) - T(t_j)\big), \tag{B.10}$$

where m is the number of parameters being fitted, n is the number of data points in the fit window, $y(t_i)$ is the fitted data points, $T(t_i)$ is the fitted value at t_i, and $C(t_i,t_j)$ is the covariance matrix of the fitted data points, estimated from the bootstrap sub-ensembles.

Appendix C.

List of Calculated Values

C.1. Quark Masses

In order to better constrain the coefficients of the flavour breaking-expansion laid out in Section 5.2.5 we employ a a range of partially-quenched valence quarks, corresponding to the neutral pseudoscalar meson mass in range $230\,\text{MeV} \lesssim m_{\bar{q}q} \lesssim 790\,\text{MeV}$. The full list of values used is displayed on the next two pages.

C.2. Vector Current Renormalisation

The full list of Z_V^f values calculated for each valence quark mass/charge combination on each gauge ensemble are listed in the next two pages.

C.3. Finite-Volume Corrections

The full list of finite-volume corrections for a_μ^{HVP} calculated for each valence quark mass/charge combination on each gauge ensemble are listed in the next two pages.

Ensemble	Valence κ	Charge	$m_{\bar{q}q}$ [GeV]	Z_v	$\Delta a_\mu^{\text{HVP}}$
A	0.123 850	2/3	0.754(3)	0.8465(11)	6.88×10^{-10}
	0.124 362	2/3	0.431(1)	0.8296(25)	5.29×10^{-9}
	0.124 383 8	2/3	0.413(1)*	0.8260(22)	7.23×10^{-10}
	0.124 520	2/3	0.270(2)	0.8179(50)	1.24×10^{-8}
	0.121 100	−1/3	0.784(3)	0.8848(14)	6.08×10^{-10}
	0.121 713	−1/3	0.407(1)	0.8625(38)	6.68×10^{-9}
	0.121 702 6	−1/3	0.414(1)*	0.8620(14)	7.94×10^{-10}
	0.121 865	−1/3	0.235(6)	0.8504(61)	1.56×10^{-8}
	0.120 240	0	0.760(4)	0.8959(13)	6.92×10^{-10}
	0.120 814 2	0	0.412(1)*	0.8733(18)	8.13×10^{-10}
	0.120 855	0	0.378(1)	0.8708(10)	7.95×10^{-9}
B	0.123 850	2/3	0.755(2)	0.8466(13)	7.06×10^{-10}
	0.124 440	2/3	0.360(2)	0.8267(94)	8.50×10^{-9}
	0.124 520	2/3	0.272(2)	0.8108(41)	1.39×10^{-8}
	0.121 100	−1/3	0.788(2)	0.8851(16)	5.97×10^{-10}
	0.121 676	−1/3	0.459(1)	0.8631(16)	5.56×10^{-9}
	0.121 865	−1/3	0.243(2)	0.8568(56)	1.58×10^{-8}
	0.120 240	0	0.770(2)	0.8965(15)	6.88×10^{-10}
	0.120 855	0	0.369(2)	0.8717(39)	8.14×10^{-9}
C	0.123 850	2/3	0.758(2)	0.380(1)	8.37×10^{-10}
	0.124 508	2/3	0.293(2)	0.8192(21)	1.82×10^{-8}
	0.124 520	2/3	0.280(2)	0.8187(17)	2.36×10^{-9}
	0.121 100	−1/3	0.788(2)	0.8852(6)	6.99×10^{-10}
	0.121 821	−1/3	0.307(2)	0.8587(85)	1.68×10^{-8}
	0.121 466	−1/3	0.586(2)	0.8692(9)	2.76×10^{-9}
	0.121 865	−1/3	0.255(2)	0.8546(13)	2.55×10^{-9}
	0.120 240	0	0.771(2)	0.8963(7)	8.09×10^{-10}
	0.120 855	0	0.384(1)	0.8708(10)	1.31×10^{-9}

Table C.1. Valence quark masses and charges used in this study. Ensemble details listed in Table 5.1, SU(3)-symmetric point marked with *. Charge is in units of e, $m_{\bar{q}q}$ is the neutral pseudoscalar meson mass. Z_V is the vector current renormalisation. $\Delta a_\mu^{\text{HVP}}$ is the finite-volume correction to a_μ^{HVP}.

Ensemble	Valence κ	Charge	$m_{\bar{q}q}$ [GeV]	Z_v	$\Delta a_\mu^{\text{HVP}}$
D	0.123 859	2/3	0.764(4)	0.8465(11)	4.5×10^{-11}
	0.124 362	2/3	0.432(4)	0.8296(25)	8.64×10^{-10}
	0.124 382 4	2/3	0.414(4)*	0.8260(22)	9.82×10^{-10}
	0.124 520	2/3	0.255(5)	0.8179(50)	2.92×10^{-9}
	0.121 100	−1/3	0.795(4)	0.8848(14)	3.84×10^{-11}
	0.121 713	−1/3	0.410(3)	0.8625(38)	1.24×10^{-9}
	0.121 703 2	−1/3	0.419(3)*	0.8620(14)	1.14×10^{-9}
	0.121 865	−1/3	0.231(3)	0.8504(61)	4.08×10^{-9}
	0.120 240	0	0.773(4)	0.8959(13)	4.66×10^{-11}
	0.120 813 5	0	0.416(3)*	0.8733(18)	1.18×10^{-9}
	0.120 855	0	0.384(2)	0.8708(13)	1.6×10^{-9}
E	0.123 850	2/3	0.758(4)	0.8466(13)	4.82×10^{-11}
	0.124 440	2/3	0.364(3)	0.8267(94)	1.77×10^{-9}
	0.124 520	2/3	0.266(5)	0.8109(41)	3.56×10^{-9}
	0.121 100	−1/3	0.791(4)	0.8851(16)	3.8×10^{-11}
	0.121 676	−1/3	0.440(2)	0.8631(16)	3.43×10^{-9}
	0.121 865	−1/3	0.230(9)	0.8568(56)	4.16×10^{-9}
	0.120 240	0	0.777(4)	0.8965(15)	4.71×10^{-11}
	0.120 855	0	0.380(2)	0.8717(39)	1.67×10^{-9}
F	0.123 850	2/3	0.639(3)	0.8458(8)	6.84×10^{-11}
	0.124 508	2/3	0.286(2)	0.8192(21)	6.55×10^{-9}
	0.124 508	2/3	0.273(2)	0.8187(17)	7.48×10^{-9}
	0.121 100	−1/3	0.751(3)	0.8852(6)	5.12×10^{-11}
	0.121 821	−1/3	0.300(2)	0.8692(9)	5.67×10^{-9}
	0.121 466	−1/3	0.580(4)	0.8692(9)	3.86×10^{-10}
	0.120 240	0	0.689(4)	0.8963(7)	6.47×10^{-11}
	0.120 855	0	0.366(5)	0.8708(10)	3.03×10^{-9}

Table C.1. Valence quark masses and charges used in this study. Ensemble details listed in Table 5.1, SU(3)-symmetric point marked with *. Charge is in units of e, $m_{\bar{q}q}$ is the neutral pseudoscalar meson mass. Z_V is the vector current renormalisation. $\Delta a_\mu^{\text{HVP}}$ is the finite-volume correction to a_μ^{HVP}.

Bibliography

[1] J. S. Schwinger, *On Quantum electrodynamics and the magnetic moment of the electron*, *Phys. Rev.* **73** (1948) 416–417. 1, 15

[2] P. Kusch and H. Foley, *The Magnetic Moment of the Electron*, *Phys. Rev.* **74** (1948) 250. 1, 15

[3] T. Aoyama, T. Kinoshita and M. Nio, *Revised and Improved Value of the QED Tenth-Order Electron Anomalous Magnetic Moment*, *Phys. Rev. D* **97** (2018) 036001, [arXiv:1712.06060]. 1, 16, 21

[4] D. Hanneke, S. Fogwell and G. Gabrielse, *New Measurement of the Electron Magnetic Moment and the Fine Structure Constant*, *Phys. Rev. Lett.* **100** (2008) 120801, [arXiv:0801.1134]. 1, 16

[5] T. Aoyama et al., *The anomalous magnetic moment of the muon in the Standard Model*, arXiv:2006.04822. 1, 16, 20, 21, 24, 26, 112

[6] Muon g-2 collaboration, E. Valetov, *Toward the Frontiers of Particle Physics With the Muon g-2 Experiment*, in *3rd World Summit on Exploring the Dark Side of the Universe*, 9, 2020. arXiv:2009.07709. 2

[7] Muon g-2 collaboration, J. Grange et al., *Muon (g-2) Technical Design Report*, arXiv:1501.06858. 2, 19

[8] M. Abe et al., *A New Approach for Measuring the Muon Anomalous Magnetic Moment and Electric Dipole Moment*, *PTEP* **2019** (2019) 053C02, [arXiv:1901.03047]. 2, 19

[9] S. Borsanyi et al., *Leading-order hadronic vacuum polarization contribution to the muon magnetic momentfrom lattice QCD*, arXiv:2002.12347. 2, 27, 97, 100, 112

[10] ATLAS collaboration, G. Aad et al., *Observation of a new particle in the search for*

the Standard Model Higgs boson with the ATLAS detector at the LHC, Phys. Lett. B **716** (2012) 1–29, [arXiv:1207.7214]. 5

[11] CMS collaboration, S. Chatrchyan et al., *Observation of a New Boson at a Mass of 125 GeV with the CMS Experiment at the LHC*, Phys. Lett. B **716** (2012) 30–61, [arXiv:1207.7235]. 5

[12] E. Drexler, *Elementary particle interactions in the standard model*, 2014. [Online; accessed 26-January-2021], https://upload.wikimedia.org/wikipedia/commons/a/a7/Elementary_particle_interactions_in_the_Standard_Model.png. 6

[13] C. M. Institute, *Yang-mills and mass gap*, 2017. [Online; accessed 14-June-2021], http://www.claymath.org/millennium-problems/yang%5C%E2%5C%80%5C%93mills-and-mass-gap. 11

[14] D. J. Gross and F. Wilczek, *Ultraviolet behavior of non-abelian gauge theories*, Phys. Rev. Lett. **30** (Jun, 1973) 1343–1346. 11

[15] H. D. Politzer, *Reliable perturbative results for strong interactions?*, Phys. Rev. Lett. **30** (Jun, 1973) 1346–1349. 11

[16] Particle Data Group collaboration, M. Tanabashi et al., *Review of Particle Physics*, Phys. Rev. D **98** (2018) 030001. 14

[17] P. A. Dirac, *The quantum theory of the electron*, Proc. Roy. Soc. Lond. A **117** (1928) 610–624. 15

[18] Muon g-2 collaboration, G. Bennett et al., *Final Report of the Muon E821 Anomalous Magnetic Moment Measurement at BNL*, Phys. Rev. D **73** (2006) 072003, [hep-ex/0602035]. 16, 17

[19] P. J. Mohr, B. N. Taylor and D. B. Newell, *CODATA Recommended Values of the Fundamental Physical Constants: 2010*, Rev. Mod. Phys. **84** (2012) 1527–1605, [arXiv:1203.5425]. 16

[20] M. Davier, A. Hoecker, B. Malaescu and Z. Zhang, *Reevaluation of the hadronic vacuum polarisation contributions to the Standard Model predictions of the muon* $g-2$ *and* $\alpha(m_Z^2)$ *using newest hadronic cross-section data*, Eur. Phys. J. C **77** (2017) 827, [arXiv:1706.09436]. 16, 20

[21] A. Keshavarzi, D. Nomura and T. Teubner, *Muon* $g-2$ *and* $\alpha(M_Z^2)$*: a new*

data-based analysis, Phys. Rev. D **97** (2018) 114025, [arXiv:1802.02995]. 16, 20

[22] G. Colangelo, M. Hoferichter and P. Stoffer, *Two-pion contribution to hadronic vacuum polarization*, JHEP **02** (2019) 006, [arXiv:1810.00007]. 16, 20

[23] M. Hoferichter, B.-L. Hoid and B. Kubis, *Three-pion contribution to hadronic vacuum polarization*, JHEP **08** (2019) 137, [arXiv:1907.01556]. 16, 20

[24] M. Davier, A. Hoecker, B. Malaescu and Z. Zhang, *A new evaluation of the hadronic vacuum polarisation contributions to the muon anomalous magnetic moment and to* $\alpha(\mathbf{m_Z^2})$, Eur. Phys. J. C **80** (2020) 241, [arXiv:1908.00921]. 16, 20

[25] A. Keshavarzi, D. Nomura and T. Teubner, $g-2$ *of charged leptons,* $\alpha(M_Z^2)$ *, and the hyperfine splitting of muonium*, Phys. Rev. D **101** (2020) 014029, [arXiv:1911.00367]. 16, 20

[26] A. Kurz, T. Liu, P. Marquard and M. Steinhauser, *Hadronic contribution to the muon anomalous magnetic moment to next-to-next-to-leading order*, Phys. Lett. B **734** (2014) 144–147, [arXiv:1403.6400]. 16, 20

[27] K. Melnikov and A. Vainshtein, *Hadronic light-by-light scattering contribution to the muon anomalous magnetic moment revisited*, Phys. Rev. D **70** (2004) 113006, [hep-ph/0312226]. 16, 20, 24

[28] P. Masjuan and P. Sanchez-Puertas, *Pseudoscalar-pole contribution to the* $(g_\mu - 2)$*: a rational approach*, Phys. Rev. D **95** (2017) 054026, [arXiv:1701.05829]. 16, 20, 24

[29] G. Colangelo, M. Hoferichter, M. Procura and P. Stoffer, *Dispersion relation for hadronic light-by-light scattering: two-pion contributions*, JHEP **04** (2017) 161, [arXiv:1702.07347]. 16, 20, 24

[30] M. Hoferichter, B.-L. Hoid, B. Kubis, S. Leupold and S. P. Schneider, *Dispersion relation for hadronic light-by-light scattering: pion pole*, JHEP **10** (2018) 141, [arXiv:1808.04823]. 16, 20, 24

[31] A. Gérardin, H. B. Meyer and A. Nyffeler, *Lattice calculation of the pion transition form factor with* $N_f = 2 + 1$ *Wilson quarks*, Phys. Rev. D **100** (2019) 034520, [arXiv:1903.09471]. 16, 20, 24

[32] J. Bijnens, N. Hermansson-Truedsson and A. Rodríguez-Sánchez, *Short-distance constraints for the HLbL contribution to the muon anomalous magnetic moment*, *Phys. Lett. B* **798** (2019) 134994, [arXiv:1908.03331]. 16, 20, 24

[33] G. Colangelo, F. Hagelstein, M. Hoferichter, L. Laub and P. Stoffer, *Longitudinal short-distance constraints for the hadronic light-by-light contribution to* $(g-2)_\mu$ *with large-*N_c *Regge models*, *JHEP* **03** (2020) 101, [arXiv:1910.13432]. 16, 20, 24

[34] G. Colangelo, M. Hoferichter, A. Nyffeler, M. Passera and P. Stoffer, *Remarks on higher-order hadronic corrections to the muon g−2*, *Phys. Lett. B* **735** (2014) 90–91, [arXiv:1403.7512]. 16, 20, 24

[35] T. Blum, N. Christ, M. Hayakawa, T. Izubuchi, L. Jin, C. Jung et al., *Hadronic Light-by-Light Scattering Contribution to the Muon Anomalous Magnetic Moment from Lattice QCD*, *Phys. Rev. Lett.* **124** (2020) 132002, [arXiv:1911.08123]. 16, 20, 24

[36] T. Aoyama, M. Hayakawa, T. Kinoshita and M. Nio, *Complete Tenth-Order QED Contribution to the Muon g-2*, *Phys. Rev. Lett.* **109** (2012) 111808, [arXiv:1205.5370]. 16, 20

[37] T. Aoyama, T. Kinoshita and M. Nio, *Theory of the Anomalous Magnetic Moment of the Electron*, *Atoms* **7** (2019) 28. 16

[38] A. Czarnecki, W. J. Marciano and A. Vainshtein, *Refinements in electroweak contributions to the muon anomalous magnetic moment*, *Phys. Rev. D* **67** (2003) 073006, [hep-ph/0212229]. 16, 20, 22

[39] C. Gnendiger, D. Stöckinger and H. Stöckinger-Kim, *The electroweak contributions to* $(g-2)_\mu$ *after the Higgs boson mass measurement*, *Phys. Rev. D* **88** (2013) 053005, [arXiv:1306.5546]. 16, 20

[40] B. Jäger, *Hadronic Matrix Elements in Lattice QCD*. PhD thesis, Mainz U., 2014. https://openscience.ub.uni-mainz.de/handle/20.500.12030/4247. 18

[41] V. Pauk and M. Vanderhaeghen, *Single meson contributions to the muon's anomalous magnetic moment*, *Eur. Phys. J. C* **74** (2014) 3008, [arXiv:1401.0832]. 20, 24

[42] I. Danilkin and M. Vanderhaeghen, *Light-by-light scattering sum rules in light of*

new data, *Phys. Rev. D* **95** (2017) 014019, [arXiv:1611.04646]. 20, 24

[43] M. Knecht, S. Narison, A. Rabemananjara and D. Rabetiarivony, *Scalar meson contributions to a μ from hadronic light-by-light scattering*, *Phys. Lett. B* **787** (2018) 111–123, [arXiv:1808.03848]. 20, 24

[44] G. Eichmann, C. S. Fischer and R. Williams, *Kaon-box contribution to the anomalous magnetic moment of the muon*, *Phys. Rev. D* **101** (2020) 054015, [arXiv:1910.06795]. 20, 24

[45] P. Roig and P. Sanchez-Puertas, *Axial-vector exchange contribution to the hadronic light-by-light piece of the muon anomalous magnetic moment*, *Phys. Rev. D* **101** (2020) 074019, [arXiv:1910.02881]. 20, 24

[46] F. Jegerlehner, *The anomalous magnetic moment of the muon*, vol. 226. 2008, 10.1007/978-3-540-72634-0. 20, 24

[47] S. J. Brodsky and E. de Rafael, *Suggested boson-lepton pair couplings and the anomalous magnetic moment of the muon*, *Phys. Rev.* **168** (Apr, 1968) 1620–1622. 24

[48] B. E. Lautrup and E. de Rafael, *Calculation of the sixth-order contribution from the fourth-order vacuum polarization to the difference of the anomalous magnetic moments of muon and electron*, *Phys. Rev.* **174** (Oct, 1968) 1835–1842. 24

[49] KLOE-2 collaboration, A. Anastasi et al., *Combination of KLOE $\sigma\left(e^+e^- \to \pi^+\pi^-\gamma(\gamma)\right)$ measurements and determination of $a_\mu^{\pi^+\pi^-}$ in the energy range $0.10 < s < 0.95$ GeV^2*, *JHEP* **03** (2018) 173, [arXiv:1711.03085]. 24, 25, 26

[50] BaBar collaboration, B. Aubert et al., *Precise measurement of the e+ e- −> pi+ pi- (gamma) cross section with the Initial State Radiation method at BABAR*, *Phys. Rev. Lett.* **103** (2009) 231801, [arXiv:0908.3589]. 24, 26

[51] H. Czyż et al., *Constraining the Hadronic Contributions to the Muon Anomalous Magnetic Moment*, arXiv:1306.2045. 26

[52] V. M. Aul'chenko et al., *Measurement of the e+ e- −> pi+ pi- cross section with the CMD-2 detector in the 370 - 520-MeV c.m. energy range*, *JETP Lett.* **84** (2006) 413–417, [hep-ex/0610016]. 26

[53] M. N. Achasov et al., *Update of the e+ e- −> pi+ pi- cross-section measured by*

*SND detector in the energy region 400-MeV $<$ s**(1/2) $<$ file1000-MeV*, *J. Exp. Theor. Phys.* **103** (2006) 380–384, [hep-ex/0605013]. 26

[54] BESIII collaboration, M. Ablikim et al., *Measurement of the $e^+e^- \to \pi^+\pi^-$ cross section between 600 and 900 MeV using initial state radiation*, *Phys. Lett. B* **753** (2016) 629–638, [arXiv:1507.08188]. 26

[55] T. Xiao, S. Dobbs, A. Tomaradze, K. K. Seth and G. Bonvicini, *Precision Measurement of the Hadronic Contribution to the Muon Anomalous Magnetic Moment*, *Phys. Rev. D* **97** (2018) 032012, [arXiv:1712.04530]. 26

[56] Fermilab Lattice, LATTICE-HPQCD, MILC collaboration, B. Chakraborty et al., *Strong-Isospin-Breaking Correction to the Muon Anomalous Magnetic Moment from Lattice QCD at the Physical Point*, *Phys. Rev. Lett.* **120** (2018) 152001, [arXiv:1710.11212]. 27

[57] Budapest-Marseille-Wuppertal collaboration, S. Borsanyi et al., *Hadronic vacuum polarization contribution to the anomalous magnetic moments of leptons from first principles*, *Phys. Rev. Lett.* **121** (2018) 022002, [arXiv:1711.04980]. 27, 100

[58] RBC, UKQCD collaboration, T. Blum, P. Boyle, V. Gülpers, T. Izubuchi, L. Jin, C. Jung et al., *Calculation of the hadronic vacuum polarization contribution to the muon anomalous magnetic moment*, *Phys. Rev. Lett.* **121** (2018) 022003, [arXiv:1801.07224]. 27, 97, 100, 112

[59] D. Giusti, V. Lubicz, G. Martinelli, F. Sanfilippo and S. Simula, *Electromagnetic and strong isospin-breaking corrections to the muon $g-2$ from Lattice QCD+QED*, *Phys. Rev. D* **99** (2019) 114502, [arXiv:1901.10462]. 27

[60] PACS collaboration, E. Shintani and Y. Kuramashi, *Hadronic vacuum polarization contribution to the muon $g-2$ with 2+1 flavor lattice QCD on a larger than (10 fm)^4 lattice at the physical point*, *Phys. Rev. D* **100** (2019) 034517, [arXiv:1902.00885]. 27, 97, 100

[61] Fermilab Lattice, LATTICE-HPQCD, MILC collaboration, C. Davies et al., *Hadronic-vacuum-polarization contribution to the muon's anomalous magnetic moment from four-flavor lattice QCD*, *Phys. Rev. D* **101** (2020) 034512, [arXiv:1902.04223]. 27, 97, 100

[62] A. Gérardin, M. Cè, G. von Hippel, B. Hörz, H. B. Meyer, D. Mohler et al., *The*

leading hadronic contribution to $(g-2)_\mu$ from lattice QCD with $N_f = 2+1$ flavours of O(a) improved Wilson quarks, Phys. Rev. D **100** (2019) 014510, [arXiv:1904.03120]. 27, 97, 110, 112

[63] C. Aubin, T. Blum, C. Tu, M. Golterman, C. Jung and S. Peris, *Light quark vacuum polarization at the physical point and contribution to the muon $g-2$*, Phys. Rev. D **101** (2020) 014503, [arXiv:1905.09307]. 27, 97, 100

[64] D. Giusti and S. Simula, *Lepton anomalous magnetic moments in Lattice QCD+QED*, PoS **LATTICE2019** (2019) 104, [arXiv:1910.03874]. 27

[65] K. G. Wilson, *Confinement of quarks*, Physical Review D **10** (Oct., 1974) 2445–2459. 29, 31, 36, 38

[66] R. P. Feynman, *Space-time approach to nonrelativistic quantum mechanics*, Rev. Mod. Phys. **20** (1948) 367–387. 29

[67] F. Mandl, *Statistical Physics*. The Manchester Physics Series, 2 ed., 1991. 30

[68] J. Smit, *Introduction to quantum fields on a lattice: A robust mate*, vol. 15. Cambridge University Press, 1, 2011. 30

[69] C. Gattringer and C. B. Lang, *Quantum chromodynamics on the lattice*, vol. 788. Springer, Berlin, 2010, 10.1007/978-3-642-01850-3. 30, 49

[70] K. Symanzik, *Continuum limit and improved action in lattice theories*, Nuclear Physics B **226** (Sept., 1983) 187–204. 36

[71] P. Weisz, *Continuum limit improved lattice action for pure yang-mills theory (i)*, Nuclear Physics B **212** (Feb., 1983) 1–17. 36

[72] T. Blum, C. E. Detar, S. A. Gottlieb, K. Rummukainen, U. M. Heller, J. E. Hetrick et al., *Improving flavor symmetry in the Kogut-Susskind hadron spectrum*, Phys. Rev. D **55** (1997) 1133–1137, [hep-lat/9609036]. 38

[73] H. Neuberger, *Exactly massless quarks on the lattice*, Phys. Lett. B **417** (1998) 141–144, [hep-lat/9707022]. 38

[74] L. Susskind, *Lattice fermions*, Physical Review D **16** (Nov., 1977) 3031–3039. 38

[75] J. Kogut and L. Susskind, *Hamiltonian formulation of wilson's lattice gauge theories*, Physical Review D **11** (Jan., 1975) 395–408. 38

[76] P. H. Ginsparg and K. G. Wilson, *A remnant of chiral symmetry on the lattice*, *Physical Review D* **25** (May, 1982) 2649–2657. 38

[77] L. Giusti and M. Luscher, *Chiral symmetry breaking and the Banks-Casher relation in lattice QCD with Wilson quarks*, *JHEP* **03** (2009) 013, [arXiv:0812.3638]. 39

[78] B. Sheikholeslami and R. Wohlert, *Improved continuum limit lattice action for QCD with wilson fermions*, *Nuclear Physics B* **259** (Sept., 1985) 572–596. 40

[79] N. Cundy et al., *Non-perturbative improvement of stout-smeared three flavour clover fermions*, *Phys. Rev. D* **79** (2009) 094507, [arXiv:0901.3302]. 40, 44

[80] H. Rothe, *Lattice gauge theories: An Introduction*, vol. 43. 1992. 40, 43

[81] S. Duane, A. D. Kennedy, B. J. Pendleton and D. Roweth, *Hybrid Monte Carlo*, *Phys. Lett. B* **195** (1987) 216–222. 44

[82] M. Hayakawa and S. Uno, *QED in finite volume and finite size scaling effect on electromagnetic properties of hadrons*, *Prog. Theor. Phys.* **120** (2008) 413–441, [arXiv:0804.2044]. 45

[83] A. Duncan, E. Eichten and H. Thacker, *Electromagnetic splittings and light quark masses in lattice QCD*, *Phys. Rev. Lett.* **76** (1996) 3894–3897, [hep-lat/9602005]. 45

[84] R. Horsley et al., *QED effects in the pseudoscalar meson sector*, *JHEP* **04** (2016) 093, [arXiv:1509.00799]. 45, 52, 53, 54, 56, 87, 100

[85] QCDSF collaboration, R. Horsley, Y. Nakamura, D. Pleiter, P. Rakow, G. Schierholz, H. Stüben et al., *Electromagnetic splitting of quark and pseudoscalar meson masses from dynamical QCD + QED*, *PoS* **Lattice2013** (2014) 499, [arXiv:1311.4554]. 45, 52

[86] R. Horsley et al., *Isospin splittings of meson and baryon masses from three-flavor lattice QCD + QED*, *J. Phys. G* **43** (2016) 10LT02, [arXiv:1508.06401]. 45, 52, 53, 54, 55

[87] RBC, UKQCD collaboration, T. Blum et al., *Domain wall QCD with physical quark masses*, *Phys. Rev. D* **93** (2016) 074505, [arXiv:1411.7017]. 51

[88] ETM collaboration, C. Alexandrou et al., *Pion vector form factor from lattice QCD at the physical point*, *Phys. Rev. D* **97** (2018) 014508, [arXiv:1710.10401]. 51

[89] W. Bietenholz et al., *Flavour blindness and patterns of flavour symmetry breaking in lattice simulations of up, down and strange quarks*, *Phys. Rev. D* **84** (2011) 054509, [arXiv:1102.5300]. 52, 54

[90] R. Sommer, *Scale setting in lattice QCD*, *PoS* **LATTICE2013** (2014) 015, [arXiv:1401.3270]. 52

[91] QCDSF-UKQCD collaboration, R. Horsley, J. Najjar, Y. Nakamura, H. Perlt, D. Pleiter, P. Rakow et al., *SU(3) flavour symmetry breaking and charmed states*, *PoS* **LATTICE2013** (2014) 249, [arXiv:1311.5010]. 52

[92] CSSM, QCDSF, UKQCD collaboration, R. Horsley et al., *Isospin splittings in the decuplet baryon spectrum from dynamical QCD+QED*, *J. Phys. G* **46** (2019) 115004, [arXiv:1904.02304]. 53

[93] M. Lüscher, *Volume dependence of the energy spectrum in massive quantum field theories*, *Communications in Mathematical Physics* **104** (June, 1986) 177–206. 53

[94] W. Bietenholz et al., *Tuning the strange quark mass in lattice simulations*, *Phys. Lett. B* **690** (2010) 436–441, [arXiv:1003.1114]. 54

[95] K. Can, A. Kusno, E. Mastropas and J. Zanotti, *Hadron Structure on the Lattice*, *Lect. Notes Phys.* **889** (2015) 69–105. 60

[96] W. Wilcox, T. Draper and K.-F. Liu, *Chiral limit of nucleon lattice electromagnetic form-factors*, *Phys. Rev. D* **46** (1992) 1109–1122, [hep-lat/9205015]. 60

[97] S. Collins et al., *Dirac and Pauli form factors from lattice QCD*, *Phys. Rev. D* **84** (2011) 074507, [arXiv:1106.3580]. 60, 61

[98] P. Boyle, V. Gülpers, J. Harrison, A. Jüttner, C. Lehner, A. Portelli et al., *Isospin breaking corrections to meson masses and the hadronic vacuum polarization: a comparative study*, *JHEP* **09** (2017) 153, [arXiv:1706.05293]. 61

[99] I. A. Qattan et al., *Precision Rosenbluth measurement of the proton elastic form-factors*, *Phys. Rev. Lett.* **94** (2005) 142301, [nucl-ex/0410010]. 61

[100] E94110 collaboration, M. E. Christy et al., *Measurements of electron proton elastic cross-sections for 0.4 $<$ Q**2 $<$ 5.5 (GeV/c)**2*, *Phys. Rev. C* **70** (2004) 015206, [nucl-ex/0401030]. 61

[101] M. Diehl and P. Kroll, *Nucleon form factors, generalized parton distributions and quark angular momentum*, *Eur. Phys. J. C* **73** (2013) 2397, [arXiv:1302.4604]. 61

[102] J. Bickerton, R. Horsley, Y. Nakamura, H. Perlt, D. Pleiter, P. Rakow et al., *Patterns of flavor symmetry breaking in hadron matrix elements involving u, d, and s quarks*, *Phys. Rev. D* **100** (2019) 114516, [arXiv:1909.02521]. 63

[103] T. Blum, *Lattice calculation of the lowest order hadronic contribution to the muon anomalous magnetic moment*, *Phys. Rev. Lett.* **91** (2003) 052001, [hep-lat/0212018]. 69, 70

[104] D. Bernecker and H. B. Meyer, *Vector Correlators in Lattice QCD: Methods and applications*, *Eur. Phys. J. A* **47** (2011) 148, [arXiv:1107.4388]. 69, 72, 78, 92

[105] C. Aubin, T. Blum, P. Chau, M. Golterman, S. Peris and C. Tu, *Finite-volume effects in the muon anomalous magnetic moment on the lattice*, *Phys. Rev. D* **93** (2016) 054508, [arXiv:1512.07555]. 69, 72, 76, 92

[106] E. de Rafael, *Hadronic contributions to the muon g-2 and low-energy QCD*, *Phys. Lett. B* **322** (1994) 239–246, [hep-ph/9311316]. 70

[107] B. Lautrup, A. Peterman and E. de Rafael, *Recent developments in the comparison between theory and experiments in quantum electrodynamics*, *Physics Reports* **3** (May, 1972) 193–259. 70

[108] C. T. Sachrajda and G. Villadoro, *Twisted boundary conditions in lattice simulations*, *Phys. Lett. B* **609** (2005) 73–85, [hep-lat/0411033]. 70

[109] P. F. Bedaque, *Aharonov-Bohm effect and nucleon nucleon phase shifts on the lattice*, *Phys. Lett. B* **593** (2004) 82–88, [nucl-th/0402051]. 70

[110] G. M. de Divitiis, R. Petronzio and N. Tantalo, *On the discretization of physical momenta in lattice QCD*, *Phys. Lett. B* **595** (2004) 408–413, [hep-lat/0405002]. 70

[111] P. Boyle, L. Del Debbio, E. Kerrane and J. Zanotti, *Lattice Determination of the Hadronic Contribution to the Muon $g-2$ using Dynamical Domain Wall Fermions*, *Phys. Rev. D* **85** (2012) 074504, [arXiv:1107.1497]. 72

[112] C. Aubin, T. Blum, M. Golterman and S. Peris, *Model-independent parametrization of the hadronic vacuum polarization and g-2 for the muon on the lattice*, *Phys. Rev. D* **86** (2012) 054509, [arXiv:1205.3695]. 74

[113] M. Della Morte, A. Francis, V. Gülpers, G. Herdoíza, G. von Hippel, H. Horch et al., *The hadronic vacuum polarization contribution to the muon $g-2$ from lattice QCD*, *JHEP* **10** (2017) 020, [arXiv:1705.01775]. 81, 93

[114] S. Borsanyi, Z. Fodor, T. Kawanai, S. Krieg, L. Lellouch, R. Malak et al., *Slope and curvature of the hadronic vacuum polarization at vanishing virtuality from lattice QCD*, *Phys. Rev. D* **96** (2017) 074507, [arXiv:1612.02364]. 83

[115] A. Francis, B. Jaeger, H. B. Meyer and H. Wittig, *A new representation of the Adler function for lattice QCD*, *Phys. Rev. D* **88** (2013) 054502, [arXiv:1306.2532]. 93

[116] D. Giusti, F. Sanfilippo and S. Simula, *Light-quark contribution to the leading hadronic vacuum polarization term of the muon $g-2$ from twisted-mass fermions*, *Phys. Rev. D* **98** (2018) 114504, [arXiv:1808.00887]. 97, 100

[117] C. H. Chan, G. Brown and P. A. Rikvold, *Macroscopically constrained wang-landau method for systems with multiple order parameters and its application to drawing complex phase diagrams*, *Physical Review E* **95** (May, 2017) . 97

[118] C. Lehner and A. S. Meyer, *Consistency of hadronic vacuum polarization between lattice QCD and the R-ratio*, *Phys. Rev. D* **101** (2020) 074515, [arXiv:2003.04177]. 97

[119] J. Foley, K. Jimmy Juge, A. O'Cais, M. Peardon, S. M. Ryan and J.-I. Skullerud, *Practical all-to-all propagators for lattice QCD*, *Comput. Phys. Commun.* **172** (2005) 145–162, [hep-lat/0505023]. 106, 107

[120] J. J. Wu, W. Kamleh, D. t. Leinweber, R. D. Young and J. M. Zanotti, *Accessing high-momentum nucleons with dilute stochastic sources*, *J. Phys. G* **45** (2018) 125102, [arXiv:1807.09429]. 106

[121] TXL collaboration, N. Eicker et al., *Evaluating sea quark contributions to flavor singlet operators in lattice QCD*, *Phys. Lett. B* **389** (1996) 720–726, [hep-lat/9608040]. 107

[122] S. R. Beane et al., *Charged multi-hadron systems in lattice QCD+QED*, arXiv:2003.12130. 110

[123] I. Montvay and G. Munster, *Quantum fields on a lattice*. Cambridge Monographs on Mathematical Physics. Cambridge University Press, 3, 1997, 10.1017/CBO9780511470783. 117

[124] M. Gell-Mann, *THE EIGHTFOLD WAY: A THEORY OF STRONG INTERACTION SYMMETRY*, tech. rep., Mar., 1961. 10.2172/4008239. 118

[125] R. Achilles and A. Bonfiglioli, *The early proofs of the theorem of campbell, baker, hausdorff, and dynkin*, *Archive for History of Exact Sciences* **66** (Apr., 2012) 295–358. 119

[126] E. Jones, T. Oliphant, P. Peterson et al., *SciPy: Open source scientific tools for Python*, 2001–. http://www.scipy.org/. 121